Numerical Study of Pattern Forming Processes in Models of Rotating Rayleigh-Bénard Convection

Thesis by
Michael Louie

In Partial Fulfillment of the Requirements
for the Degree of
Doctor of Philosophy

California Institute of Technology
Pasadena, California

2001
(Defended June 23, 2000)

Acknowledgements

Primary acknowledgement must be given to my advisors, Professors Michael Cross and Dan Meiron. Their patience, guidance and understanding throughout the course of this work has proved to be invaluable. This thesis would not have been possible without their steady stream of ideas and suggestions. I have also benefitted from valuable discussions with Maya Tokman and Dr. Hector Ceniceros.

On a more personal note, I wish to thank the Faculty, staff and students of the Applied Mathematics department at Caltech who have helped to provide an atmosphere highly conducive to the pursuit of scientific research. Many students in particular must be thanked for providing distractions when this pursuit threatened to become overwhelming. Amongst them, Drs. Muruhan Rathinam, Mark Meloon, Imran Hashim and Russina Sgoureva-Philippakos.

Last, but certainly not least, thanks must be extended to my parents for all their support over the years. Special thanks to my brother Dr. Ken Louie, who has always been a source of inspiration to me. But most of all, I would like to thank my wife, Dr. Helen Si, whose continual support has been nothing short of vital in seeing this project to its completion.

Abstract

In this thesis we numerically study two unique pattern forming processes observed in Rayleigh-Bénard convection. Using variants of the Swift-Hohenberg equation, we study the Küppers-Lortz instability and a spiral chaos state in a large cylindrical cell. For the Küppers-Lortz instability, we show that the theoretical scaling of the correlation length and domain switching frequency hold in the case of our model equations. We find, however, that it is necessary to account for finite size effects by scaling the correlation length appropriately. We find then that the correlation length scales linearly with the size of the cell when the cell is small and/or when the control parameter is small. Scaling of the domain switching frequency for finite size effects is not necessary as domain switching appears to be enhanced by sidewall processes. Our results provide strong evidence that finite size effects are responsible for the observed discrepancies between theoretical and experimental scalings.

We also study the effect of rotation on the spiral state which occurs in a Swift-Hohenberg equation through a coupling with mean flow effects. We find that rotation and mean flow are competing processes. Mean flow shifts the pattern wave number so that the usual Küppers-Lortz instability is only observed at higher rotation rates. A parameter search is performed and a consistent trend of patterns is observed as the rotation rate is increased.

Contents

List of Figures

List of Tables

Chapter 1

Introduction

1.1 Rayleigh-Bénard Convection and the Küppers-Lortz Instability

Pattern formation is a fascinating process that occurs in many diverse physical systems [17]. The underlying connection in these processes is the formation of ordered structures out of essential disorder. This is most easily characterized by the formation of a small number of definite length scales in the system. Although the mechanisms responsible for this pattern formation can be vastly different in different systems, the similarity of the ordering process is truly remarkable. This leads one to search for a more fundamental understanding of these processes.

The difficulty in studying these processes is the inherent complexity in most physical systems. It is often difficult to isolate or control exactly those mechanisms which are responsible for determining the pattern forming processes. One system which is amenable to detailed study is the Rayleigh-Bénard convection (RBC) system. This involves a fluid which is confined between two horizontal parallel plates. The two plates are considered to be perfect conductors relative to the fluid between them so that temperature variations across each plate are negligible, while the temperature difference between the plates can be precisely controlled. If the bottom plate is heated, then initially, the fluid remains at rest and a linear temperature profile is established in the fluid. This is known as the conduction or uniform state. If the temperature difference ΔT is increased beyond some critical value ΔT_c, the dissipative effects of thermal conduction and viscosity are overcome and convection sets in. The important control parameter here is the Rayleigh number R, which is the dimensionless ratio of the destabilizing buoyancy force $\rho_0 \alpha g \Delta T$

to the stabilizing dissipative force $\nu\kappa\rho_0/d^3$

$$R = \frac{\alpha g \Delta T d^3}{\kappa\nu}, \tag{1.1}$$

where ρ_0 is the average mass density, α the thermal expansion coefficient, g the acceleration of gravity, ν the kinematic viscosity, κ the thermal diffusivity and d the plate separation. The transition from the conduction to the convection state then occurs as the parameter $\epsilon = (R - R_c)/R_c = \Delta T/\Delta T_c - 1$ passes through zero and becomes positive. The critical Rayleigh number $R_c = \alpha g \Delta T_c d^3/\kappa\nu \approx 1708$, is found to be independent of the fluid under consideration (see [12]). The pattern which is observed is one in which fluid rises in some regions and falls in others with a characteristic horizontal length scale d, the only length scale available in the ideal laterally infinite system. These structures are known as convection rolls. A schematic picture of a Rayleigh-Bénard convection roll pattern is shown in Fig. (1.1).

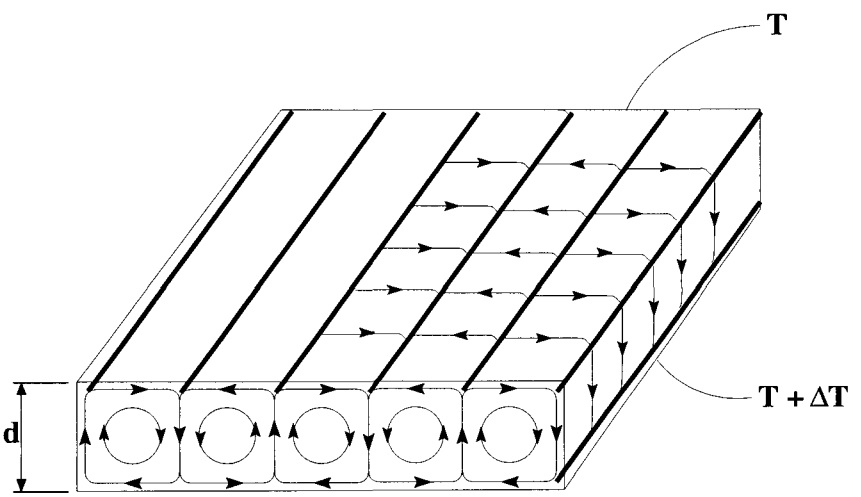

Figure 1.1: Schematic picture of Rayleigh-Bénard convection showing fluid streamlines in an ideal roll state.

The most important way specific fluid properties enter thermal convection is through another important dimensionless parameter. The Prandtl number $\sigma = \nu/\kappa$, represents the ratio of the two damping mechanisms acting on the fluid, the kinematic viscosity ν and the thermal diffusivity κ. It has been shown to be important in controlling the effects in secondary instabilities in the convection system.

Very close to onset (i.e., for small positive ϵ), the parallel roll state is essentially time independent. However, the system can be made more complex and interesting even near onset by rotating the entire system about a vertical axis. Coriolis forces then become important and render the system non-variational. Thus time dependent states can occur arbitrarily close to onset. Depending on the rotation rate Ω, an interesting new instability is seen. Instead of observing reasonably straight parallel rolls, a collection of smaller domains of parallel rolls oriented at different angles to each other is seen. The domains are dynamic with one domain being replaced over time by a neighboring domain, only to be replaced itself by another domain. This replacement occurs by domain wall propagation rather than a spontaneous change of roll orientation within the domains. This rather novel phenomenon is known as the Küppers-Lortz (KL) instability.

The KL instability was first investigated theoretically by Küppers and Lortz in 1969 [35]. In that work, they showed that the existence of a nonlinear instability of the parallel roll state in the rotating Rayleigh-Bénard convection system for the special case of infinite Prandtl number, $\sigma \to \infty$ and free slip boundary conditions. They found the parallel roll state to be maximally unstable to a set of rolls oriented at 58° (in the sense of rotation) to the original set of rolls when the Taylor number $T = (2\Omega)^2$, exceeds a critical value of 2285. Later Küppers [36] showed the same phenomenon exists for finite Prandtl numbers and rigid boundary conditions.

The first experimental observations of the KL-unstable state were by Heikes and Busse [11, 26] in 1980. Using water as the fluid and shadowgraph flow-visualization techniques, they observed patterns consisting of domains of rolls of more or less uniform roll orientation at a value of $\epsilon > 0.5$. As predicted by theory, switching of domain orientations was observed over time. But for large ϵ the switching angle was generally found to be greater than the predicted KL angle of 58° and the instability occurred for a rotation rate less than the theoretically expected value Ω_c [25]. Later experiments by

others [52], also in water, recorded patterns down to $\epsilon \approx 0.1$ and also found KL domains well below the predicted Ω_c. The measured switching angle however, agreed well with the theoretical value.

After the initial early work mentioned above, this system received little attention for almost a decade. But recent interest in studying systems which exhibit spatio-temporal chaos, for which the KL system is an ideal candidate, has renewed interest in it for both experimentalists [7, 31, 42, 51, 52] and theorists [18, 21, 41, 43, 48] alike.

1.2 Boussinesq Equations and Swift-Hohenberg Models

Another advantage of studying the Rayleigh-Bénard convection system is the existence of well known governing equations of motion. These are the so-called Oberbeck-Boussinesq equations which are derived from the Navier-Stokes equation and the conservation law for heat. But in the Oberbeck-Boussinesq equations, a considerable simplification is made by assuming that all fluid parameters except the density ρ are constant. In nondimensionalized form the equations are

$$\sigma^{-1}\left(\frac{\partial \mathbf{u}}{\partial t} + \mathbf{u}\cdot\nabla\mathbf{u}\right) = -\sigma^{-1}\nabla\left(\frac{p}{\rho_0}\right) + \theta\hat{z} + \nabla^2\mathbf{u}, \tag{1.2}$$

$$\frac{\partial \theta}{\partial t} + \mathbf{u}\cdot\nabla\theta = \nabla^2\theta + R\hat{z}\cdot\mathbf{u}, \tag{1.3}$$

$$\nabla\cdot\mathbf{u} = 0, \tag{1.4}$$

where $\mathbf{u}$ is the fluid velocity, θ is the temperature deviation from the linear conduction profile, p is the pressure deviation from the conduction profile and $\hat{z}$ is the unit vector in the vertical direction. The parameters here are the Prandtl number $\sigma = \nu/\kappa$, the mean fluid density ρ_0, the Rayleigh number $R = \alpha g \Delta T d^3/\kappa\nu$ where α is the thermal expansion coefficient, g is the acceleration due to gravity and d is the fluid depth. The appropriate boundary conditions at the top and bottom plates are

$$\mathbf{u} = \theta = 0, \quad z = \pm\frac{1}{2}. \tag{1.5}$$

In the ideal system, the plates are of infinite lateral extent and no lateral boundary conditions are needed. In practice, of course, it is necessary to have sidewalls and these

will inevitably complicate the behavior of the solutions as well as the analysis of these equations.

The linear instability of the uniform conduction state leading to the formation of convection rolls has been extensively studied in this system. The onset of solutions varying as $e^{i\mathbf{k}\cdot\mathbf{x}}$ can be found in essentially closed form [12]. The important parameter controlling this transition is the Rayleigh number, which has a critical value of $R_c = 1707.76$, regardless of the fluid. The critical wave vector is $k_0 = 3.117$. Notice that this is very close to π, so that the roll size is very close to the depth.

A detailed study of the stability boundaries has been done by Busse and his co-workers [10, 13]. In this work, several different instabilities have been identified and classified, according to their visual appearance. Of further interest and importance are the corresponding amplitude equations for this system, which govern the growth of the instabilities. These were first calculated by Cross in 1980 [14]. He found that for a single set of rolls nearly parallel to the y-axis, the equation for the complex amplitude $A(\mathbf{x}, t)$ is [17]

$$\tau_0 \partial_t A = \epsilon A + \xi_0^2 [\partial_x - (i/2q_0)\partial_y^2]^2 A - g_0 |A|^2 A. \tag{1.6}$$

The parameters appearing in this equation are found to be

$$\tau_0^{-1} = \frac{19.65\sigma}{\sigma + 0.5117}, \tag{1.7}$$

$$\xi_0^2 = 0.148, \tag{1.8}$$

$$g_0 = 0.6995 - 0.0047\sigma^{-1} + 0.0083\sigma^{-2}. \tag{1.9}$$

Although the amplitude equation is a schematic perturbation expansion of the full equations, it clearly does not incorporate all the spatial structure of the solutions in the fluid system. Therefore a detailed study of the amplitude equation is not usually performed. However, since the amplitude equation possesses the necessary mechanisms for pattern formation in the convection system, it is used as a basis for simpler model equations whose amplitude equations have the same form as Eq. (1.6). An important

equation of this type is the Swift-Hohenberg equation [46],

$$\frac{\partial \psi}{\partial t} = \epsilon\psi - (\nabla^2 + 1)^2\psi - \psi^3. \tag{1.10}$$

Using a multiple scales perturbation approach to separate the fast and slow space and time scales, it can be shown (see, for example, Appendix A of [17]) that the amplitude equation for Eq. (1.10) is,

$$\tau_0 \partial_t A = \epsilon A + \xi_0^2[\partial_x - (i/2)\partial_y^2]^2 A - g_0|A|^2 A, \tag{1.11}$$

with $\tau_0 = 1$, $\xi_0^2 = 4$ and $g_0 = 3$. Thus, solutions to the Swift-Hohenberg equation will exhibit similar pattern formation properties as the full Rayleigh-Bénard convection system because of this common amplitude equation.

It is important to note here that as a model for convection, the field ψ is only a function of two space variables x and y. Thus the study of this equation is considerably simpler than for the full fluid system, which involve coupled equations for the three fluid velocity components and the temperature field in three space dimensions. Although this equation bears little resemblance to the fluid equations for Rayleigh-Bénard convection, they do share the same basic instabilities through the common amplitude equation. Therefore, the Swift-Hohenberg equation can be used to study many of the interesting phenomena seen in RBC, without the need to solve the more complicated full system. Here the dependent variable ψ can be most closely related to the mid-depth temperature θ in the fluid system.

It is not surprising that the Swift-Hohenberg equation lacks many of the features found in the full fluid system. Firstly, the equation is potential, so that Eq. (1.10) can be written as

$$\frac{\partial \psi}{\partial t} = -\frac{\delta \mathcal{F}}{\delta \psi}, \tag{1.12}$$

where $\mathcal{F}$ is the potential given by

$$\mathcal{F} = \int dx\, dy \left\{ -\frac{1}{2}\epsilon\psi^2 + \frac{1}{2}[(\nabla^2 + 1)^2\psi]^2 + \frac{1}{4}\psi^4 \right\}. \tag{1.13}$$

For such a system, the dynamics consists of relaxation towards the minimum in $\mathcal{F}$, so persistent dynamics, periodic or chaotic, is not possible. Also, the stability diagram shows qualitative differences with the Busse balloon (the stability boundaries for the fluid equations) (see [22]) so that the solutions of Eq. (1.10) often fail to capture important qualitative features found in the full fluid system. Therefore, modifications are made to this equation at the nonlinear level to try to better emulate the missing features [23]. This derives a whole class of Swift-Hohenberg models to study, including a modification to model the Küppers-Lortz instability [18].

If we consider rotating the entire Rayleigh-Bénard system about a vertical axis at a (dimensionless) rate of Ω, then Eq. (1.2) becomes,

$$\sigma^{-1}\left(\frac{\partial \mathbf{u}}{\partial t}+\mathbf{u}\cdot\nabla\mathbf{u}\right)=-\sigma^{-1}\nabla\left(\frac{p}{\rho_0}\right)+\theta\hat{z}+\nabla^2\mathbf{u}+\Omega\hat{z}\times\mathbf{u}. \tag{1.14}$$

The addition of rotation gives rise to an important chiral-symmetry breaking term, which as seen in experiments, provides for more interesting and complex dynamics. To model this effect in a Swift-Hohenberg model, it is necessary to construct a term which induces a similar symmetry breaking effect. The simplest term constructed out of ψ and its derivatives retaining the inversion symmetry $\psi \to -\psi$, the parity symmetry $\mathbf{x} \to -\mathbf{x}$ and the rotational invariance in the (x,y)-plane is $g_2\hat{z}\cdot\nabla\times\left[(\nabla\psi)^2\nabla\psi\right]$. Here the parameter g_2 is approximately proportional to the rotation rate Ω for small rotations.

It is also important to include another nonlinear term in the Swift-Hohenberg model for the KL instability. This term, $g_3\nabla\cdot\left[(\nabla\psi)^2\nabla\psi\right]$, in conjunction with the term modeling the rotation, can be shown to be necessary in generating the appropriate instabilities of rolls of one orientation towards another, as we have in the KL instability [18]. The parameters g_2 and g_3 are then used to tune the instability to give the appropriate growth rate of rolls oriented at an angle of $\theta_{\mathrm{KL}} \approx 60^\circ$ as predicted by Küppers and Lortz [35] and as seen in experiment [52].

1.3 Discrepancies Between Theory and Experiment

The theoretical analysis of the Oberbeck-Boussinesq equations is carried out assuming laterally infinite systems, but experiments are done in necessarily finite geometries. Of

course, one may hope to construct an experimental cell large enough that sidewall effects may be considered negligible, but in practice this is nearly impossible due to physical limitations (such as producing plates that can be considered truly flat, or perfect conductors). But in fact, many interesting effects are due to the presence of the sidewalls and it is therefore worthwhile seeking solutions which include lateral boundaries. In the case of finite geometries, exact analytical solutions of the governing equations is generally impossible to obtain and it is necessary to seek numerical alternatives.

A major outstanding discrepancy between theory and experiment is the scaling of correlation length and domain switching frequencies in the KL state in rotating RBC. The correlation length gives a measure of the size of the domains of rolls while the domain switching frequency gives a measure of the time it takes for a set of rolls to undergo a switching of their orientation. On the basis of Ginzburg-Landau models, the correlation length ξ is expected to vary as $\xi \propto \epsilon^{-1/2}$ and the domain switching ω_a varies linearly with the control parameter ϵ, $\omega_a \propto \epsilon$ for small ϵ. Of course, the theory assumes no lateral boundaries, so the experiments are conducted in cells of large aspect ratio to try to minimize the effects of a finite geometry. Even so, the scalings obtained from experiment are found to be inconsistent with those predicted from theory. In the recent experiments of Hu *et al.* [31], the scalings were found to be $\xi \propto \epsilon^{-0.2}$ and $\omega_a \propto \epsilon^{0.6}$ in stark contrast to the theoretical predictions. When higher order corrections in ϵ are included in the scalings, and the theoretically predicted values used at the lowest order, unacceptably large coefficients for the corrections are needed to adequately fit the data.

Our goal is to shed some light on this discrepancy by conducting numerical experiments to determine the valid scalings in a finite geometry. There still exists severe computational barriers to the numerical solution of the full Boussinesq equations in the experimental geometry (a large cylindrical cell), but as we have seen, solving a corresponding Swift-Hohenberg model should provide us with some insight. The Swift-Hohenberg model considered by Cross *et al.* [18] has been shown to accurately reproduce the behavior seen in the experimental KL state, but their calculations have been performed in a periodic rectangular geometry. Therefore, we solve the Swift-Hohenberg model in a cylindrical geometry, and then apply the same pattern analysis techniques as in experiment to obtain the corresponding correlation lengths and domain switching

frequencies. Since we are not numerically simulating the actual experiments, it is not our intention to necessarily obtain their scalings, but instead understand whether finite geometries may be responsible for the discrepancies.

We find that, in the case of the model equation, the theoretical scaling for the correlation length holds, after an appropriate scaling of the values to take account of finite size effects. In particular, we find that the correlation length scales linearly with the size of the cell when the cell becomes small and/or when the control parameter $\epsilon \to 0$. The switching frequency appears to follow the theoretical scaling without the need to rescale the values for the finite cell size. This is not surprising since our model does not account for complicated sidewall effects, and we therefore expect the sidewalls to enhance the domain switching behavior since the rolls are often nucleated from the sidewalls. Similar scalings of the correlation length and domain switching frequency are attempted in the experiments, [33], but in the experiments, the rotation rate rather than the cell size is varied. These results are found to support the theoretical scalings with only limited success as large corrections to the theoretically predicted scalings are necessary to accurately fit the data. This may be due to the less obvious relationship between finite size effects and the rotation rate. Furthermore, sidewall effects certainly play a role in the case of the experiments. Therefore, it would worthwhile in the future to consider more complicated boundary effects in our model to see if these affect our scalings of the domain switching frequency.

1.4 Outline of the Thesis

In order to provide some explanation for the different time and length scales seen in experiment and theory, we perform a numerical study of a Swift-Hohenberg model in a finite cylindrical geometry. Although numerical studies of Swift-Hohenberg models have been performed before (for example, see [4, 18, 21, 22]), they have not been conducted in truly cylindrical geometries, or have considered the models relevant to the Küppers-Lortz instability.

Another difficulty that is encountered in the numerical solution of these problems is the need to find efficient, stable algorithms. Since the time scales involved are typically very long, use of explicit or even semi-implicit schemes is impractical. This, coupled

with the fact that it is necessary to solve these equations in a circular geometry, presents a major obstacle to progress. In this thesis, we have considered several approaches to numerically solving the Swift-Hohenberg models in the cylindrical geometry with varying degrees of success.

Numerical solutions to Swift-Hohenberg models have been obtained by many other researchers. However, these have not necessarily concentrated on modeling the KL instability or have not looked at solving the equations in a truly circular domain. Most importantly, none have considered developing codes which can be used to evolve the solution over very long time scales. For this, a fully implicit scheme is needed, which has been developed in our work.

We also implement pattern diagnostic techniques to obtain comparisons with experiment. This requires the collection and processing of large amounts of data which we believe has not been attempted before. Again, this may be attributed to the need for a numerical scheme which allows for long time evolutions. Our study reveals a dependence on the finite size of the domain which may account for the discrepancies seen in scaling of time and length scales of experiment and theory.

Finally, we extended our solution technique to a generalized Swift-Hohenberg equation which takes account of mean flow effects. Mean flow arises when the vertical vorticity is driven by roll curvature and amplitude modulations. Coupling to mean flow has been shown to play a key role, for example, in the onset of weak turbulence [39, 24, 45, 53]. We follow the approach of Xi *et al.* [50] from a model suggested by Greenside and Cross [23], but extend their results by adding terms related to rotation. In the absence of rotation, and for sufficiently large ϵ and sufficiently large cells and strong mean flow, spiral chaos is observed, in agreement with the experimental system. We have found that the addition of rotation has a negative effect on spiral formation, often unwinding the spirals. As we further increase the rotation, we find that it is possible to remove all spiral structures from the pattern. The spirals are first replaced by a quasi-static or slowly evolving roll structures which are reasonably straight for smaller ϵ, but may become more curved at higher $\epsilon > 0.55$. At higher rotation rates, this roll pattern is replaced by the familiar KL state. The onset of the KL state however, occurs at considerably higher rotation rates than would be expected in the absence of mean flow. This further confirms the existence

of the competition between mean flow and rotational effects in the system.

The rest of this thesis is organized as follows. In Chapter 2, several numerical schemes for Swift-Hohenberg models are presented, leading to a fully implicit scheme suitable for use in integrating over very long time scales. We also show the need for a variable radial mesh to help stabilize some numerical artifacts which arise when using a polar mesh. In Chapter 3 we present the techniques for pattern and data analysis following the work of experimentalists. In Chapter 4, a generalized Swift-Hohenberg equation is solved and the effects of rotation on the spiral chaos state is considered.

Chapter 2
Numerical Simulation of the Model Equations

2.1 Swift-Hohenberg Models

Our models of Rayleigh-Bénard convection are conveniently studied using the time dependent fourth-order partial differential equation,

$$\frac{\partial \psi}{\partial t} = \epsilon\psi - (\nabla^2 + 1)^2\psi + N(\psi, t), \tag{2.1}$$

where $\psi(\mathbf{x}, t)$ is a real-valued function of two horizontal space variables. In the physical set up, the field ψ would roughly represent the mid-plane temperature field of the convecting fluid. $N(\psi, t)$ is a nonlinear function of ψ and possibly time t, and it is through this term that the interesting dynamics can be generated. We notice that the mechanism represented by this equation is a basic linear instability at wave number 1 when the control parameter $\epsilon > 0$. Expanding about $\mathbf{k} = \hat{x}$, for example, we see that the linear growth rate Γ for wave number $\mathbf{k} = (1 + \Delta k_x) \cdot \hat{x} + \Delta k_y \cdot \hat{y}$ is

$$\Gamma(\mathbf{k}) = \epsilon - 4\left[\Delta k_x + \frac{1}{2}(\Delta k_y)^2\right]^2, \tag{2.2}$$

which is of the same form as that for the linear instability in Rayleigh-Bénard convection. With $N(\psi) = -\psi^3$, we obtain the original Swift-Hohenberg equation. By considering more complicated forms of the nonlinear term $N(\psi)$, we are able to use Eq. (2.1) to simulate the dynamics seen in the Küppers-Lortz instability.

2.1.1 Modeling the Küppers-Lortz Instability

A particularly novel instability is seen when the Rayleigh-Bénard system is rotated about a vertical axis. In the nonrotating case, straight parallel rolls are typically observed just above onset, but in the rotating case, several patches of differently oriented stripe patterns are possible once a critical rotation rate is exceeded. These patches are dynamic in the sense that they are constantly in a process of creation and destruction which occurs primarily through boundary interactions with other patches. In particular, one set of rolls becomes unstable towards a second set of rolls rotated at a particular angle $\theta_{\mathrm{KL}} = 58°$. This second set of rolls, when established, in turn becomes unstable to a third set of rolls, rotated through a further θ_{KL}, and so on. This is the well documented Küppers-Lortz (KL) instability.

Early efforts to model this instability by Busse and Heikes [11] involved using a three-mode model with $\theta_{KL} = 60° \approx 58°$, but with no spatial variation. Later Tu and Cross [48] added spatial dependence to the model, as well as more realistic interaction terms, but still limited study to the truncated set of three orientations. In order to more accurately model the continuous range of orientations possible in the fluid system, Cross *et al.* [18] derived a Swift-Hohenberg type model which would allow for a full range of possible roll orientations. The model they developed has the form of Eq. (2.1) where the nonlinear term is taken to be

$$N(\psi) = -g_1\psi^3 + g_2\hat{z}\cdot\nabla\times\left[(\nabla\psi)^2\nabla\psi\right] + g_3\nabla\cdot\left[(\nabla\psi)^2\nabla\psi\right]. \tag{2.3}$$

If we take the parameters g_2 and g_3 to be zero, we recover the original Swift-Hohenberg equation. The second term is the important term which breaks the reflection or chiral symmetry, and represents the effect of rotation on the convection system. It is the simplest term constructed out of ψ and its derivatives retaining the inversion symmetry $\psi \to -\psi$, the parity symmetry $\mathbf{x} \to -\mathbf{x}$ and the rotational invariance in the x,y plane. In a derivation of this model equation from the fluid equations we would expect g_2 to *increase* with the rotation rate Ω, and to be proportional to Ω for small rotations.

The reason for including the third term is shown by calculating the amplitude equa-

tion for this model. Writing

$$\psi = \sum_j A_j \exp[i\mathbf{q}_j \cdot \mathbf{x}], \tag{2.4}$$

gives amplitude equations for A_j of the form,

$$\frac{\partial A_j}{\partial t} = \epsilon A_j + 4\left(\frac{\partial}{\partial x_j} - \frac{i}{2}\frac{\partial^2}{\partial y_j^2}\right)^2 - g_0|A_j|^2 A_j - \sum_{j\neq k} g(\theta_{jk})|A_k|^2 A_j, \tag{2.5}$$

where θ_{jk} is the angle from $\mathbf{q}_j$ to $\mathbf{q}_k$, and

$$g_0 = \frac{1}{2}g(\theta_{jj}) = 3(g_1 + g_3), \tag{2.6}$$

$$g(\theta_{jk}) = 6g_1 + 2g_2\sin(2\theta_{jk}) + 4g_3 + 2g_3\cos(\theta_{jk}), \tag{2.7}$$

and the coordinates are $x_j = \mathbf{x}\cdot\mathbf{q}_j$ and $y_j = \mathbf{x}\cdot(\mathbf{z}\times\mathbf{q}_j)$. The Küppers-Lortz instability, when stripes i become unstable towards stripes j, first occurs for the angle $\theta_{ij} = \theta_{\mathrm{KL}}$ that gives $g(\theta_{ij})$ its largest negative value. Minimizing $g(\theta)$ gives

$$\tan(2\theta_{\mathrm{KL}}) = g_2/g_3, \tag{2.8}$$

and the instability then occurs for

$$3g_1 + g_3 - 2\sqrt{g_2^2 + g_3^2} < 0. \tag{2.9}$$

Thus the coefficient g_3 can be used to tune θ_{KL}. For example, if we wish to mimic the Küppers-Lortz instability where the rolls are maximally unstable to another set of rolls at $\pi/3$ to the original rolls, we set

$$g_2/g_3 = \tan(2\frac{\pi}{3}) = -\sqrt{3}, \tag{2.10}$$

and then Eq. (2.9) implies that the instability occurs for $g_1 < g_3$. Note that by rescaling the magnitude of ψ we may choose g_1 to be of unit magnitude, and we shall assume that this is the case unless otherwise noted. Then the Küppers-Lortz instability at an angle $\theta_{\mathrm{KL}} = \pi/3$ occurs for $g_1 = 1$, $g_2 = -\sqrt{3}g_3$ and $g_3 > 1$. Note that a band of orientations

$\Delta\theta \sim (g_3/g_1 - 1)^{1/2}$ will actually be unstable (see [18]).

2.1.2 Numerical Challenges

The full fluid system still represents a considerable challenge to current computational capabilities although researchers have begun to implement such problems in finite rectangular geometries [37]. The effect of finite system sizes and fixed boundaries on the dynamics of pattern forming processes, like the Küppers-Lortz instability, is still not fully understood, even in the model systems. Therefore, as a first step, we consider studying these effects in the corresponding Swift-Hohenberg models. These, too, present many challenges to the researcher looking to accurately and efficiently integrate numerically equations of the form of Eq. (2.1).

The main difficulties to overcome are inherent in the problem we wish to study. These are a circular physical geometry and a need to obtain solutions over long time scales. Since theoretical results really only apply in the weakly nonlinear regime, it is particularly important to be able to study these models close to onset (where the control parameter ϵ is close to zero). In this regime, the dynamics are slow so it is necessary to obtain the solutions over long time scales if meaningful statistical information is to be obtained.

Although a circular geometry is generally easy to deal with using a standard rectangular grid (in a spatial finite difference discretization), the circular outer boundary is usually poorly approximated by such a discretization. This can lead to anomalous results near the boundary, which ultimately propagate into the bulk, where we are most interested in obtaining accurate solutions [33]. An obvious way to overcome this difficulty is to repose the problem in polar coordinates, $r = \sqrt{x^2 + y^2}$ and $\theta = \tan^{-1}(y/x)$, where x and y are the usual Cartesian coordinates, but one must then deal with the artificial singularity that is generated at the polar origin. This is a difficulty that is reasonably easy to overcome in this case (see [6]) and we choose to use a polar description instead of having to apply an appropriate fix at the outer boundary. As we will see later, a polar mesh also has the disadvantage that it is no longer uniform in space, and this causes our numerical solution to become sensitive to the computational mesh. This too can be overcome as we describe later in Section 2.6.

Given these restrictions, the difficulties involved in integrating Eq. (2.1) become more apparent. In particular, we see that the high order derivatives of the biharmonic operator precludes the use of simple explicit methods. The fourth order spatial derivatives would require time steps of the order $O(\Delta x^4)$, where Δx is the spatial step, to ensure stable solutions. Note that in polar coordinates, it is necessary to take several thousands of points in the θ direction to achieve sufficient accuracy at the outer boundary of a cell of radius ≈ 100, so that $\Delta\theta = O(10^{-3})$. Thus a time step $\Delta t = O(10^{-12})$ would be required to obtain stable solutions which this is clearly unacceptable. On the other hand, the nonlinear term makes the use of implicit methods difficult since a nonlinear system of equations would then have to be solved at each time step. Additionally, the more complicated circularly geometry makes the spatial problem more difficult to solve.

2.2 A Semi-Implicit Scheme

We have already mentioned that it is impractical to use an explicit time stepping scheme for the numerical solution of our Swift-Hohenberg models Eq. (2.1) because of the severe time step constraints necessary to stably evolve the linear biharmonic term. In this section we consider a simple hybrid time stepping method which looks to overcome this severe restriction, while also avoiding the need to solve any nonlinear problems. We find that this approach is appropriate for some choices of the nonlinearity $N(\psi)$, but has only limited success in the solution of more complicated Swift-Hohenberg models.

2.2.1 Time and Space Discretization

We avoid the severe time step constraints of an explicit method by evolving Eq. (2.1) with an implicit time stepping scheme. However, because of the nonlinear term $N(\psi)$, a fully implicit treatment will lead us to solving a nonlinear equation. To avoid this, we consider a simple hybrid time stepping scheme where the linear part of the equation is treated implicitly while the nonlinear terms are treated explicitly. A similar semi-implicit approach is used in the work of Cross *et al.* [18].

In the current implementation, we use the second order accurate Crank-Nicolson

scheme on the linear part which gives the following discretized equation in time;

$$\frac{\psi^{n+1}-\psi^n}{\Delta t} = \frac{L\psi^{n+1}+L\psi^n}{2} + \frac{1}{2}\left(3N(\psi^n) - N(\psi^{n-1})\right). \tag{2.11}$$

Here we have used L to denote the linear biharmonic operator on the right-hand side of Eq. (2.1),

$$L \equiv \epsilon - (\nabla^2 + 1)^2. \tag{2.12}$$

At each time step, $n = 0, 1, \ldots$, we have the following partial differential equation in the spatial variables to solve;

$$\left(L - \frac{2}{\Delta t}\right)\psi^{n+1} = -\left(L + \frac{2}{\Delta t}\right)\psi^n + 3N(\psi^n) - N(\psi^{n-1}). \tag{2.13}$$

Since L is a linear operator, we note that Eq. (2.13) is a linear equation for ψ^{n+1}.

We now consider an appropriate spatial discretization for these equations. This choice is clearly influenced by the physical geometry and boundary conditions of the problem under investigation. In the case of a finite geometry, the appropriate "rigid" boundary conditions are, as described in [15],

$$\psi|_B = \hat{\mathbf{n}} \cdot \nabla\psi|_B = 0, \tag{2.14}$$

where $\hat{\mathbf{n}}$ is the unit normal to the boundary of the domain, B. Since it is our goal to solve Eq. (2.1) in a truly circular geometry, it seems natural to solve Eq. (2.13) in polar coordinates, (r, θ), rather than Cartesian coordinates (x, y). We have noted before that this would also lead to a more accurate treatment of the boundary conditions at the outer radius, $r = R$. We now have a choice of discretizing the polar coordinates using finite differences or spectral methods. Although spectral methods may seem more natural because of the periodicity in the angular coordinate θ, the need to impose both a functional and derivative boundary condition at $r = R$ (in order to obtain a well-posed problem) makes this choice more difficult. Since it is a simple matter to implement periodic, functional or derivative boundary conditions using finite differences, we choose to discretize the polar domain using standard finite differences.

Our choice of spatial discretization is also influenced by the presence of the biharmonic operator L in Eq. (2.13). This term would make it difficult to consider more complicated spatial discretizations such as a mix of finite difference and spectral decompositions for the radial and angular coordinates respectively, or a spectral element decomposition. Fortunately, the work of Bjørstad on the fast direct solution of generalized biharmonic problems in rectangular domains [5] and in circular domains [6] allows us to solve Eq. (2.13) simply and efficiently in this polar, finite difference spatial discretization.

Although we have not compared the performance of Bjørstad's polar solver against an iterative solver, we have performed comparisons of the direct rectangular solver against a preconditioned conjugate gradient technique. The convergence of the iterative conjugate gradient method can, of course, be greatly improved by a careful choice of preconditioner, but we found that most natural choices of preconditioning (like diagonal preconditioning) did not improve the convergence enough to make this competitive with the direct solver. We therefore believe that Bjørstad's direct polar biharmonic solver provides us with the optimal method for solving Eq. (2.13).

2.2.2 Difficulties and Limitations

The semi-implicit scheme presented above provides a good method for solving Eq. (2.1) only for certain choices of the nonlinear term, $N(\psi)$. We found that the method was particularly stable if N did not include any terms with spatial derivatives of ψ, as in the case of the Swift-Hohenberg equation ($N(\psi) = -\psi^3$). Note that this equation is relaxational (or potential) and eventually settles down to a quasi-steady state. The slow changes which occur after long evolution times actually allow us to stably increase the time step. We also observed that the stability was not affected by the value of the parameter ϵ, for $0 < \epsilon \leq 0.3$. For accuracy reasons, though, a smaller time step should be used for larger ϵ, since the dynamics are more rapid in this regime.

The situation was quite different when more complicated nonlinear terms were involved. The numerical scheme became much more sensitive to the choice of time step size, as well as the value of ϵ. We have found that for small $\epsilon < 0.05$, the solutions evolve on a time scale of the order $t = O(10^3)$, so it would be ideal if we could use time

step which is $O(1)$. For larger $\epsilon > 0.1$, the solutions evolve more rapidly on a time scale $O(10^1)$, so a time step of 0.1 or even 0.01 would be acceptable. However, we have found that a time step $\Delta t < 0.1$ is generally needed to obtain stable solutions with $\epsilon \approx 0.01$. If larger values of ϵ are used, the method appeared to develop a local finite time singularity if the time step was maintained around 0.1. It was not always clear whether or not this singularity could be avoided by simply reducing the time step, although we did see a general improvement if this was done. Since we are interested in simulations where the parameter ϵ can be as large as 0.3, the poor stability characteristics of this scheme clearly makes this an unsuitable approach.

We have not done a complete investigation of this instability, but it is clear from our experience with this solver and the Swift-Hohenberg equation, that the difficulty lies with the nonlinear terms. Since our treatment of these terms is explicit in this scheme, it seems reasonable that we should experience some time step constraint when derivative terms are present in $N(\psi)$. This is certainly consistent with our results for the Swift-Hohenberg equation where $N(\psi) = -\psi^3$ contains no derivative terms and we appear to achieve the unconditional stability of the Crank-Nicolson scheme. Substituting the nonlinear terms for the KL instability Eq. (2.3), we see that the nonlinearities contain up to second order spatial derivatives. Thus we would expect a time step constraint of the form $\Delta t = O(\Delta x^2)$. This actually appears to be more restrictive than we find in practice, although it does explain why we were able in some cases to stabilize the solutions by reducing the time step. In any case, it is clear that we will not be able to achieve unconditional stability with this scheme when derivative terms are present in the nonlinear term $N(\psi)$.

We conclude this section by mentioning the advantages of this solver. First and foremost is the efficiency. By using the direct biharmonic solver, we are able to obtain solutions in $O(MN \log N)$ arithmetic operations (per time step), while the storage requirements are $MN + O(M) + O(N)$, where M is the number of points in the radial direction, and N is the number of points in the angular direction. The second is the simplicity. The numerical scheme can be coded in around 200 lines (excluding the biharmonic solver) and is therefore very manageable and easily maintained. Perhaps it is not surprising then, that this approach has limited usefulness, although it is clear that other

more sophisticated schemes should, where possible, take advantage of the fact that we are able to solve the linear biharmonic problem directly.

2.3 Krylov Methods and Exponential Propagation

An alternative approach to solving Eq. (2.1) is possible by using the concept of Krylov subspaces and exponential propagation. Our primary reason for investigating these methods is that they allow us to take much larger time steps than would normally be possible with the semi-implicit method we have used above. This is particularly true when the system is close to equilibrium, as is the case when the control parameter, ϵ, is close to zero. The basic idea is that the discretized spatial operator can be reasonably approximated by a moderate sized Krylov subspace. This subspace, rather than the operator itself, can be easily (and cheaply) diagonalized and the solution obtained by a simple exponentiation process. In the next section we outline the approach for linear problems, and then show how the method is extended to nonlinear problems. We then make some comments about our experience with this approach, and the difficulties we have found in applying the method to our Swfit-Hohenberg models.

2.3.1 Exponential Propagation for Linear Differential Equations

Consider the following linear initial value problem:

$$\frac{\partial U}{\partial t} = AU, \tag{2.15}$$

$$U(t_0) = U_0, \tag{2.16}$$

for an arbitrary linear operator A. The exact solution at a later time t is

$$U(t_0 + t) = e^{tA}U_0. \tag{2.17}$$

If $U(t)$ is represented in discrete form by a vector of length N, then the operator (tA) may be exponentiated if the $N \times N$ matrix form of A can be decomposed as

$$A = E\Lambda E^{-1}, \tag{2.18}$$

where E is the matrix of eigenvectors and Λ is a diagonal matrix of eigenvalues $\lambda_1, \lambda_2, \ldots, \lambda_N$. In this case

$$e^{tA} = E e^{t\Lambda} E^{-1}, \tag{2.19}$$

where $e^{t\Lambda}$ is the diagonal matrix with entries $e^{t\lambda_1}, e^{t\lambda_2}, \ldots, e^{t\lambda_N}$.

However, explicit exponentiation of the operator A by this method is quite expensive if N is large. For example, in our two-dimensional calculations we will often be using hundreds of points in the radial direction and thousands of points in the azimuthal direction. Thus N is of the order of 10^5 and the operator A would be a matrix of size $N \times N$. Even if such a large amount of storage were available, the computational cost of diagonalizing A would mean that this approach was no longer competitive with other standard methods. Instead, the idea is to approximate the action of e^{tA} on an initial vector U_0 by exponentiating a small matrix H which approximates the action of A in a Krylov subspace.

Define the K-dimensional Krylov subspace to be the space spanned by the vectors $\{U_0, AU_0, \ldots, A^{K-1}U_0\}$. An orthonormal basis for this subspace is generated by the following *Arnoldi process* [1]. Setting $w_1 \equiv U_0$, we compute, for $k = 1, 2, \ldots, K$,

$$v_k \equiv w_k / \|w_k\|, \tag{2.20}$$

$$w_{k+1} \equiv A v_k - \sum_{l=1}^{k} v_l \, (v_l, A v_k) \, . \tag{2.21}$$

This is equivalent to the Gram-Schmidt orthogonalization of the sequence of vectors $\{U_0, AU_0, \ldots, A^{K-1}U_0\}$ and the K resulting *Krylov vectors* $v_1, v_2, \ldots, v_K$ are orthonormal vectors in $\Re^N$. Although finite precision arithmetic can sometimes lead to a loss of orthogonality, we have found empirically in our calculations that a straightforward implementation of Eqs. (2.20) – (2.21) leads to a reasonably orthogonal basis set.

Now that we have constructed the orthonormal basis, we assemble the Krylov vectors into an $N \times K$ matrix V whose columns are $v_1, v_2, \ldots, v_K$. Storage requirements for these methods are dominated by the size of V, which is the largest matrix that is explicitly constructed.

The action of the operator A may be approximated in the Krylov subspace by

$$A \approx VV^T AVV^T = VHV^T,$$

where the $K \times K$ matrix

$$H \equiv V^T AV, \tag{2.22}$$

has elements

$$H_{lk} \equiv (v_l, Av_k)\,. \tag{2.23}$$

We note that by definition, v_l is orthogonal to Av_k for $l > k+1$ so H is upper Hessenberg. Also, we see that

$$\begin{aligned} H_{k+1,k} &= (v_{k+1}, Av_k) \\ &= (v_{k+1}, w_{k+1}) + \sum_{l=1}^{k} (v_l, Av_k)\,(v_{k+1}, v_l)\,, \end{aligned}$$

using Eq. (2.21). But the vectors v_l, $l = 1, 2, \ldots, k$ are orthonormal to v_{k+1} by construction, so all terms in the sum on the right-hand side are zero. Thus we have

$$\begin{aligned} H_{k+1,k} &= (v_{k+1}, w_{k+1}) \\ &= \|w_{k+1}\|, \end{aligned}$$

using Eq.(2.20), and we see that all of the elements of H are generated automatically as a byproduct of the orthogonalization in the Arnoldi process.

In order to approximate the exponential of tA, we now diagonalize the small matrix H explicitly

$$H = E\Lambda E^{-1},$$

where Λ is a diagonal $K \times K$ matrix of eigenvalues $\lambda_1, \lambda_2, \ldots, \lambda_K$ and E is the $K \times K$ matrix whose columns are the corresponding eigenvectors. The solution at time $t_0 + t$ is

then approximated by

$$U(t_0+t) = e^{tA}U_0 \approx Ve^{tH}V^TU_0 \tag{2.24}$$

$$= VEe^{t\Lambda}E^{-1}V^TU_0, \tag{2.25}$$

where $e^{t\Lambda}$ is the diagonal matrix with entries $e^{t\lambda_1}, e^{t\lambda_2}, \ldots, e^{t\lambda_K}$.

We now state some important results which are proved by Edwards *et al.* in [20]. Firstly, the approximation Eq. (2.24) can be shown to be of order $O(t^K)$. In fact, it is shown in [20] that

$$\begin{aligned} Ve^{tH}V^TU_0 &- \left(I + tA + \frac{(tA)^2}{2} + \ldots + \frac{(tA)^{K-1}}{(K-1)!}\right) \\ &= \left(\frac{t^K}{K!}I + \frac{t^{K+1}}{(K+1)!}VV^TA + \ldots\right)VV^TA^KU_0, \end{aligned}$$

and thus Eq. (2.24) approximates e^{tA} to order t^K. Although this is a correct upper bound, it is important to note the presence of the operator A, in this bound. Since $\|A\|$ may be large when we are solving PDEs, we can in fact experience very poor accuracy with this method. We will discuss this point further in Section 2.3.3. Secondly, the method can be shown to be unconditionally stable, in the sense that if

$$\lim_{t\to\infty} \left\|e^{tA}U_0\right\| = 0,$$

then

$$\lim_{t\to\infty} \left\|Ve^{tH}V^TU_0\right\| = 0.$$

Note that the stability can only be shown in the case of a symmetric operator, although the result has been extended to normal operators [20].

2.3.2 Extension to Nonlinear Problems

Consider the general nonlinear initial-value problem:

$$\frac{\partial U}{\partial t} = F(U), \tag{2.26}$$

$$U(t_0) = U_0. \tag{2.27}$$

We define

$$u(t) \equiv U(t_0 + t) - U_0, \tag{2.28}$$

and Taylor expand F about U_0 to get the following problem for u,

$$\frac{\partial u}{\partial t} = b + Au + G(u), \tag{2.29}$$

$$u(t_0) = 0, \tag{2.30}$$

where $b \equiv F(U_0)$, the Jacobian $A \equiv DF(U_0)$, and the remainder $G(u)$ is defined by

$$G(u) \equiv F(U_0 + u) - b - Au. \tag{2.31}$$

If $G(u)$ were zero, then the exact solution to Eqs. (2.29) – (2.30) would be

$$u(t) = \frac{e^{tA} - I}{A} b. \tag{2.32}$$

There is, of course, no closed form solution to Eqs. (2.29) – (2.30) when $G(u) \neq 0$. But we may write an equivalent integral equation:

$$u(t) = \frac{e^{tA} - I}{A} b + \int_0^t e^{(t-\tau)A} G(u(\tau))\, d\tau. \tag{2.33}$$

We solve Eq. (2.33) by the functional iteration

$$u^{(m+1)}(t) = \frac{e^{tA} - I}{A} b + \int_0^t e^{(t-\tau)A} G(u^{(m)}(\tau))\, d\tau \tag{2.34}$$

using Eq. (2.32) as the initial guess $u^{(0)}(t)$. Equation (2.32) is approximated by analogy with Eq. (2.25) as

$$u^{(0)}(t) \approx VE \frac{e^{t\Lambda} - I}{\Lambda} E^{-1} V^T b. \tag{2.35}$$

Recall that Λ is diagonal, so that its inversion and exponentiation is straightforward.

The convolution integral in Eq. (2.34) is evaluated by a combination of linear exponential propagation and quadrature, as follows. We calculate $G(u^{(m)}(\tau))$ at several

values of τ in order to fit $G(u^{(m)}(\tau))$ to a polynomial,

$$G(u^{(m)}(\tau)) \approx \sum_{j=2}^{J+1} g_j \tau^j, \tag{2.36}$$

where each g_j is a vector of length N. The polynomial has no constant or linear terms in τ by virtue of the definition Eq. (2.31) of the remainder $G(u)$.

The integral in Eq. (2.34) can now be written as

$$\int_0^t e^{(t-\tau)A} G(u^{(m)}(\tau))\, d\tau \approx \int_0^t e^{(t-\tau)A} \sum_j g_j \tau^j \tag{2.37}$$

$$= \sum_j \left[\int_0^t e^{(t-\tau)A} \tau^j \right] g_j. \tag{2.38}$$

We act with the integral operator in the square brackets in Eq. (2.38) on each of the vector coefficients g_j by forming a separate Krylov subspace V_j and approximate operator H_j for each j. This involves carrying out the Arnoldi process using g_j as the initial vector. The computational complexity of doing this for large $j > 10$ would quickly make this procedure undesirable. Also, there is little purpose in evaluating these integrals more accurately than the linear term Eq. (2.35). Empirically we find that much smaller Krylov spaces ($K_j \approx 2$) are optimal, and give an error that is comparable to evaluating Eq. (2.35) with $K = 20$. After diagonalizing each small matrix $H_j = E_j \Lambda_j E_j^{-1}$, the final approximation for the convolution integral Eq. (2.37) is assembled as

$$\int_0^t e^{(t-\tau)A} G(u^{(m)}(\tau))\, d\tau \approx \sum_j V_j E_j \left(\int_0^t e^{(t-\tau)\Lambda_j} \tau^j \, d\tau \right) E_j^{-1} V_j^T g_j, \tag{2.39}$$

where the Λ_j are $K_j \times K_j$ diagonal matrices. The integrals in Eq. (2.39) enclosed in parentheses are evaluated in closed form by the following recursion relation:

$$I_j \equiv \int_0^t e^{\lambda(t-\tau)} \tau^j \, d\tau \tag{2.40}$$

$$= \frac{1}{\lambda} \left[j I_{j-1} - t^j \right], \tag{2.41}$$

and

$$I_0 = \frac{1}{\lambda}\left[e^{\lambda t} - 1\right]. \tag{2.42}$$

2.3.3 Difficulties and Limitations

In order to confirm that we had implemented this approach correctly, we first considered solving the one-dimensional heat equation. The exact solution to this problem is known, and it is therefore possible to compare our computed solutions against the exact solution. In these tests, we found that we could not achieve the accuracy suggested by Edwards *et al.* A closer look at the accuracy bound they provide shows that there is a dependence of this bound on the norm of operator A, $\|A\|$. In the case of partial differential equations, this is a discretized version of the exact spatial differential operator, and therefore has an error associated with it. But what is more detrimental is the fact that $\|A\|$ may have a very large bound, essentially nullifying the benefit of having the accuracy depend on $(\Delta t)^k$. That is, reasonable accuracy is likely to be achieved only for very small time steps. Given that this is the case, there seems to be little advantage to using this approach. Therefore, as a way to solve unsteady problems, much care must be taken in simply implementing this approach with careful attention to the operator A. We should note, however, that for steady problems, or where solutions quickly approach an equilibrium state, this still remains a reasonable solution method, particularly if one is more interested in seeing the behavior of solutions over long time scales.

We have not pursued a way of overcoming this difficulty in the method. It has been shown [47] that the problem lies in the simple treatment of the time stepping by exponential propagation outlined above. Other researchers [27, 28] have developed more successful alternatives for the time evolution. Unfortunately, in the implementation of [27, 28], the accuracy drops to being only as high as third or fourth order depending on the time stepping scheme used, but still retains the advantage that generally large time steps can be taken.

Another difficulty we have encountered in attempting to implement this approach is associated with determining a reasonable approximation to the spectrum of the discretized form of A. In the exponential propagation procedure, the rightmost eigenvalues

Annulus radii	Smallest Magnitude Eigenvalues		Largest Magnitude Eigenvalues	
	Arnoldi	Exact	Arnoldi	Exact
$2\pi - 4\pi$	1.1278	0.3134	1273.84	1274.02
	22.924	0.3205	1264.97	1272.72
	42.947	0.3431	1252.29	1268.85
	67.063	0.3857	1226.68	1262.46
	96.373	0.4554	1199.91	1253.64
$\frac{\pi}{4} - \frac{9\pi}{4}$	68.129	0.3151	106464	106453
	483.76	0.3610	105977	105965
	1144.9	0.5778	104526	104515
	2239.2	1.0879	102146	102134
	3694.1	1.9516	98891	98879
$\frac{\pi}{32} - \frac{65\pi}{32}$	742.65	0.2953	3653290	3653247
	6398.0	0.3807	3635652	3635813
	25283	0.8026	3583959	3583924
	52261	1.6198	3498863	3498821
	87610	2.2493	3382551	3382517

Table 2.1: Smallest and largest magnitude eigenvalues of the discretized biharmonic operator ∇^4 in an annular region using polar coordinates. The Arnoldi values are obtained using a Krylov space of 30 vectors. The discretized operator has a total of 1024 eigenvalues.

(i.e., the ones with the largest real parts) are the most important since the solution is determined essentially from the exponentiation of these values (see Eq. (2.25) and Eq. (2.35)). For solutions that are bounded in time, the eigenvalues will have either negative real parts or only small positive real parts. Therefore, we are most interested in the small magnitude eigenvalues. We have found however, that for the discretized form of the biharmonic operator ∇^4 in polar coordinates, the Arnoldi procedure Eqs. (2.20) and (2.21), does a poor job of approximating this part of the spectrum. On the other hand, the large magnitude eigenvalues appear to be better approximated. This is shown in Table 2.1, where we give the five smallest and five largest eigenvalues obtained from diagonalizing the matrix H obtained from a basis of 30 Krylov vectors generated by the Arnoldi procedure. For comparison we give the exact eigenvalues of ∇_h^4, the discretized form of ∇^4. In this particular case, an annular domain with a resolution of 16 points in the r-direction and 64 points in the θ-direction is used, so that ∇_h^4 has a total of 1024

eigenvalues.

We notice that the large magnitude eigenvalues become larger as we shrink the annulus to a disk. It is apparent that this behavior is due to the singularity at the origin in the polar coordinate system. As the separation between the small and large magnitude eigenvalues increases, the Arnoldi procedure is clearly less and less effective at extracting the small magnitude eigenvalues of ∇_h^4. Since these are the eigenvalues that are required in the exponential propagation procedure outlined above, this would not be effective way to solve a biharmonic problem in a circular geometry. It is of course possible to replace the Arnoldi iteration with more sophisticated eigenvalue extracting procedures (for example [38]), but we have found in the case of the biharmonic operator in polar coordinates, that these too are somewhat ineffectual at extracting the required eigenvalues in reasonable times.

An obvious solution to a stiff operator is to use preconditioning. With a careful choice of preconditioner, it would be possible to ensure a well behaved spectrum for the new operator. However, it is somewhat unclear in the context of this method, exactly how the preconditioning would be implemented. We consider an approach which utilizes this idea, but in a different context, in the next section.

2.4 A Fully Implicit Scheme

The two approaches above have yielded some success in the solution of the model equation, although each has had its difficulties. The semi-implicit scheme appeared to suffer from poor stability properties, particularly for complicated nonlinearities involving spatial derivatives of ψ. While exponential propagation appeared to deal better with the nonlinearities, it suffered instead from the stiffness of the biharmonic term in polar coordinates. Our next approach was to try to combine elements of each of the previous methods in the hope of retaining each of their attractive features, whilst overcoming their difficulties. This leads to an implicit time stepping approach coupled to a Krylov subspace treatment of the spatial components.

2.4.1 Time and Space Discretization

The fully implicit scheme is closely related to the semi-implicit approach of Section (2.2). The difference occurs in the time discretization of Eq. (2.1). Instead of treating the nonlinear term explicitly, Crank-Nicolson is applied to entire right-hand side of Eq. (2.1). This then requires us to solve the following nonlinear equation at each time step $n = 0, 1, 2, \ldots,$

$$\left(-L + \frac{2}{\Delta t}\right)\psi^{n+1} - N(\psi^{n+1}) = R^n, \tag{2.43}$$

where

$$R^n = \left(L + \frac{2}{\Delta t}\right)\psi^n + N(\psi^n), \tag{2.44}$$

$$L \equiv \epsilon - (\nabla^2 + 1)^2. \tag{2.45}$$

The nonlinear equation can be solved by Newton's method, as we describe in the next section. The solution of the resultant *linear* problem once again depends on our choice of spatial discretization. For reasons given in Section (2.2), the appropriate spatial discretization will once again be the use of finite differences on the polar form of the equations.

2.4.2 Newton's Method and GMRES

In order to solve Eq. (2.43), we apply Newton's method. Let us drop the superscripts corresponding to the time step, and let

$$F(\psi) = \left(-L + \frac{2}{\Delta t}\right)\psi - N(\psi) - R = 0, \tag{2.46}$$

and $DF(\psi)$ be the *Jacobian* of $F(\psi)$. Then Newton's method involves finding a sequence, $\psi_1, \psi_2, \ldots,$ of approximations to the solution of Eq. (2.46) by successively solving the linear equation

$$DF(\psi_m)\Delta\psi = F(\psi_m), \tag{2.47}$$

for $\Delta\psi = \psi_m - \psi_{m+1}$, from which the new (and hopefully better) approximate solution, $\psi_{m+1} = \psi_m - \Delta\psi$, is obtained. Note here that the Jacobian operator, $DF(\psi)$ on the left-hand side of Eq. (2.47) is simply

$$DF(\psi) = \left(-L + \frac{2}{\Delta t}\right) - DN(\psi), \tag{2.48}$$

and $DN(\psi)$ is the Jacobian of the nonlinear term $N(\psi)$. For example, if $N(\psi) = -\psi^3$, as in the original Swift-Hohenberg equation, then $DN(\psi) = -3\psi^2$. The iteration is continued until some desired convergence criterion is reached (usually measured by the size of some norm of $F(\psi)$). As with any iterative process, an initial approximate solution, ψ_0, is required. In this case, it is most convenient to choose the solution at the previous time step.

Before discussing any convergence issues of this iteration, we first must address the method of solving the resultant linear system, Eq. (2.47), obtained at each step of Newton's method. Once again, this will depend upon the spatial discretization used, but for the reasons mentioned above, we shall assume this to be a finite difference scheme. Then, as we have seen with exponential propagation, this problem will generally be too large to store, let alone perform any kind of reduction on (such as an LU decomposition). Thus, this system cannot be solved directly, and we must resort again to some iterative procedure. We have chosen to use GMRES (generalized minimal residual) to do this, and this combined with Newton's method is just one of a class of strategies known as inexact, iterative, or truncated Newton solving (see [20], and the references therein). Like the Krylov methods mentioned in the previous section, GMRES also uses Krylov subspaces of the operator $DF(\psi)$ in its solution strategy, rather than the full operator itself. For this reason, only the action of the Jacobian, $DF(\psi)$, and the evaluation of $F(\psi)$ need to be carried out, without explicit storage or manipulation of the large linear system.

2.4.3 Some Implementation Issues

As with any iterative linear solver, the performance (convergence) of GMRES is greatly affected by preconditioning. Most preconditioning strategies involve trying to make the

operator or matrix "close," in some sense, to the identity. With this in mind, we tried preconditioning our system with the inverse of the linear biharmonic operator. We found this to greatly accelerate the convergence, as it would generally take more than 30 iterations to obtain convergence when trying to solve a simple biharmonic problem without preconditioning. We note, however, that we can actually take advantage of this preconditioning step before solving the linear system Eq. (2.47). In our implementation, preconditioning is done on Eq. (2.46). Thus we actually solve

$$\tilde{F}(\psi) \equiv \left(-L + \frac{2}{\Delta t}\right)^{-1} F(\psi) = \psi - \left(-L + \frac{2}{\Delta t}\right)^{-1} (N(\psi) + R) = 0, \tag{2.49}$$

by Newton's method. The Jacobian operator $D\tilde{F}(\psi)$ has the form

$$D\tilde{F}(\psi) = I + \left(-L + \frac{2}{\Delta t}\right)^{-1} DN(\psi), \tag{2.50}$$

where once again, $DN(\psi)$ represents the Jacobian of the nonlinear term $N(\psi)$. This saves a great deal of computation, since we see that it is no longer neccessary to evaluate the linear biharmonic operator $(-L + 2/\Delta t)$ on the current approximate solution ψ_m, and then essentially invert this operation in the preconditioning step of the GMRES procedure.

We comment briefly on the convergence of these iterations. To make it clear, we shall call the iterations performed in Newton's method, Eq. (2.47), the *outer iterations*, while the iterations performed in the GMRES procedure, the *inner iterations*. It is known that if the linear systems Eq. (2.47) are solved exactly, then Newton's method has locally quadratic convergence toward the solution of Eq. (2.46). When these linear systems are solved only approximately, generally the convergence achieved is only linear. Several guidelines have been suggested as to how to set somewhat optimal convergence criteria for the inner iterations, but we have not experimented with these. Instead, we have chosen to follow those set out in [9]. We have found in our calculations that generally no more than three inner iterations and six outer iterations are necessary to achieve convergence to an accuracy of 10^{-6} in the two-norm of F, i.e., $\|F(\psi_M)\|_2 \leq 10^{-6}$, where ψ_M is our last Newton iterate. In most cases, convergence to this accuracy was achieved in a *total* of only five to six iterations (for a time step of $\Delta t = 0.2$).

2.5 A Test Case

Since there are no known analytical solutions to the model equation Eq. (2.1), it is difficult to verify the correct performance of our code. In particular, we want to ensure that we do not generate artificial solutions. Other than performing simple tests on the various components in our solution approach (Newton's method, GMRES, etc.), there are no systematic quantitative tests for our results. Fortunately, the qualitative behavior of solutions is known for several choices of the nonlinearities $N(\psi)$ in the Swift-Hohenberg models. We consider one such case in this section which should provide us with some verification of correct code performance.

2.5.1 Convection Between Poorly Conducting Plates

We consider the following variant of our model equation;

$$\frac{\partial \psi}{\partial t} = \epsilon\psi - (\nabla^2 + 1)^2\psi + \nabla \cdot \left[(\nabla\psi)^2 \nabla\psi\right]. \tag{2.51}$$

This has been suggested as a potential model for Rayleigh-Bénard convection between poorly conducting upper and lower plates by Gertsberg and Sivashinsky [23]. It is known that a square cell pattern is the stable configuration for this equation [23]. In particular, if we start with an initial state of straight parallel rolls, we should see this becoming unstable to the square cell pattern. In a finite domain, we would expect this to happen in a predictable way. Since the most stable configuration is for the rolls to approach the boundaries with their axes perpendicular to the boundary, we would expect the square cell pattern to begin forming where the rolls are *parallel* to the boundaries. In the absence of any other perturbations in the system, the square cell state should then propagate in from the boundaries, eventually transforming the entire domain to the square cell pattern. Therefore, a good test of our code is to see if this behavior can be reproduced in our computed solutions.

2.5.2 Sensitivity to the Computational Mesh

We begin by generating an initial state of straight rolls, for example $\psi_0(x, y) = \cos(x)$. We impose zero boundary conditions, $\psi|_{r=R} = 0$, by multiplying this function by a

"cap" $w(r)$, which simply forces the value to zero at $r = R$. Once again, $r = \sqrt{x^2 + y^2}$ is the radial polar coordinate and R is the radius of the cell. Some of the choices for $w(r)$ we have considered are $w(r) = \cos(\pi r/2R)$ and $w(r) = (1 - \tanh(r - 0.95R))/2$. It is possible that our solution will show some sensitivity to this choice, but we have not observed any differences in our computed solutions when different "caps" are used.

In Fig. (2.1) we show the computed solution at $t = 50$ and $t = 75$ after starting from the initial roll state $\psi_0(x, y) = \cos(x)w(r)$, with $w(r) = (1 - \tanh(r - 0.95R))/2$ and $R = 20\pi$. The time step was $\Delta t = 0.2$. At $t = 50$, we see the expected breakdown of the rolls to the square cell state near the outer boundary. Notice that the rolls at the three and nine o'clock positions have gone unstable first, while the rolls at the six and twelve o'clock positions remain relatively unaffected. This is expected since these rolls are essentially perpendicular to the boundary, while the rolls at the three and nine o'clock positions are parallel. There is also a noticeable "bending" of some of the rolls as they approach the boundary, so as to be perpendicular to it. This seems to prevent them from going unstable to the square cell state. Although not particularly discernible at this time, a slight instability in the rolls at the center of the domain can be observed.

By $t = 75$, the breakdown of the rolls in the center of the domain is evident. It is clear, however, that this has not occurred through the square cell state propagating in from the outer boundary, but instead, through some instability being generated near the center. This breakdown is contrary to what we expect and it is necessary to seek an explanation for this behavior. It is simple to determine that the breakdown is not due to our choice of $w(r)$, or a possible time step instability. In Fig. (2.2) we show in (a) and (b) the solutions obtained using a smaller time step ($\Delta t = 0.1$), and in (c) and (d) the solutions obtained starting from an initial condition with a different cap function $w(r) = \cos(\pi r/2R)$. The lower spatial resolution (160×1024) has been used in both these runs. We once again observe the same breakdown of the rolls near the center, and can safely conclude that neither our choice of $w(r)$ or time step size is responsible for this breakdown.

It is, in fact, easy to show that the breakdown in the center of the domain is a numerical artifact due the computational grid we have used. We show in the bottom two plots in Fig. (2.1), exactly the same run as before but on a grid with twice the radial

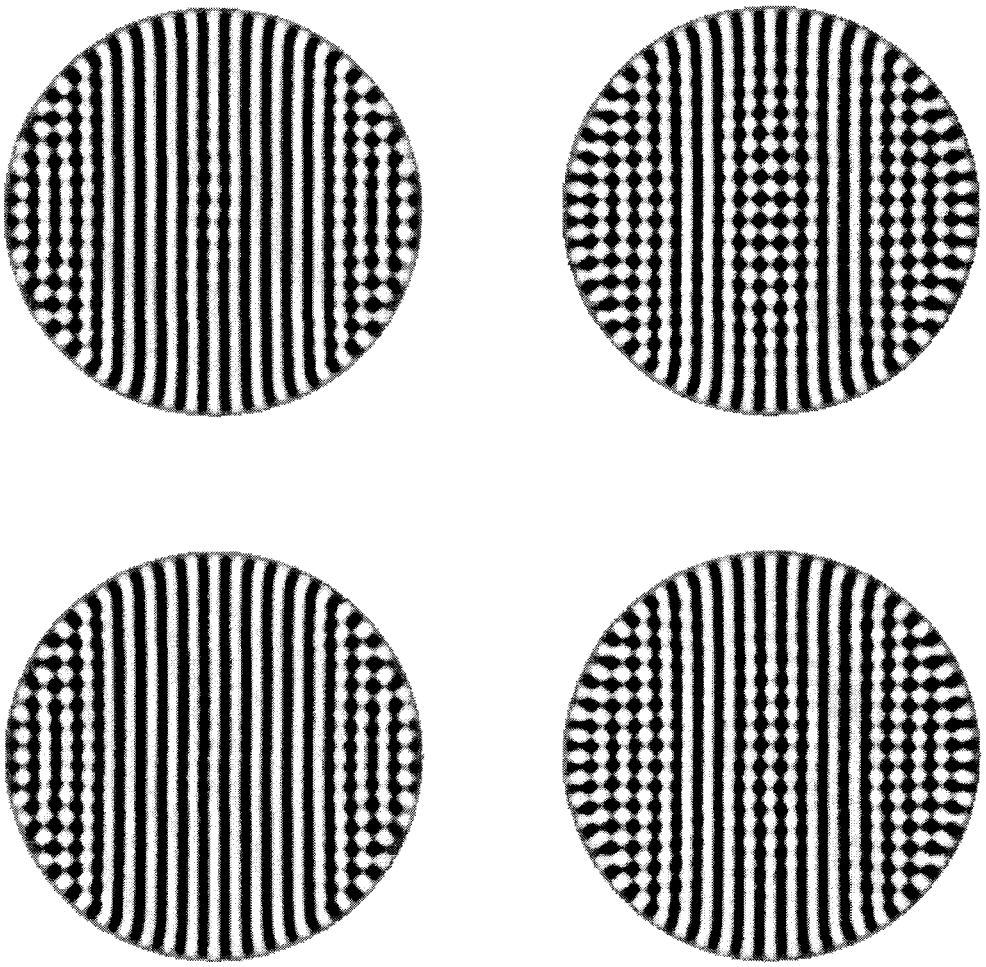

Figure 2.1: Contour plots of solutions of Eq. (2.51) with $\epsilon = 0.3$, started from straight rolls, $\psi_0 = \cos(x)(1 - \tanh(r - 0.95R))/2$. Plots on the left are at $t = 50$, plots on the right are at $t = 75$. The top plots are computed on a 160×1024 mesh, the bottom plots on a 320×1024 mesh. The time step was $\Delta t = 0.2$ for all plots.

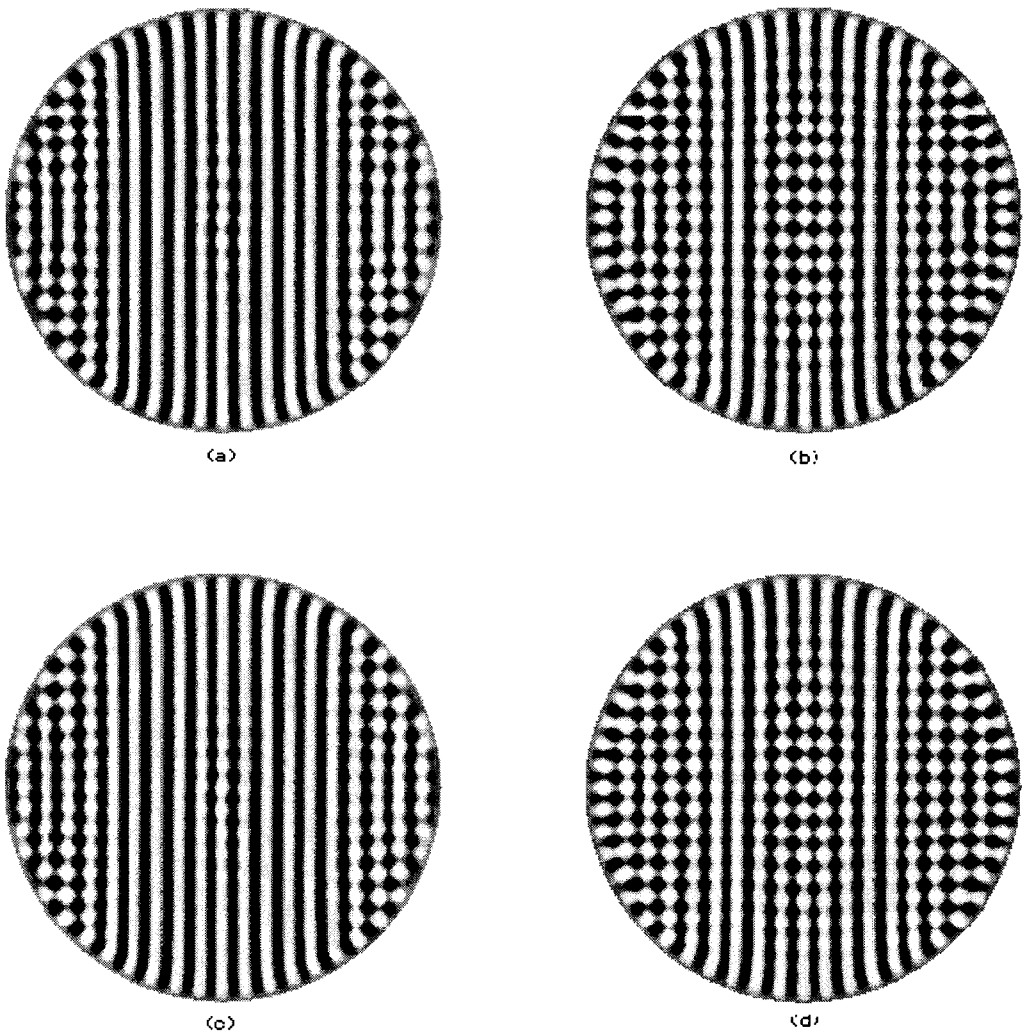

Figure 2.2: Contour plots of solutions of Eq. (2.51) with $\epsilon = 0.3$, started from straight rolls, $\psi_0 = \cos(x)w(r)$. In (a) and (b), the solution is shown at $t = 50$ and $t = 75$ respectively, and is started from the same initial condition as in Fig. (2.1). We have reduced the time step to $\Delta t = 0.1$ in this run. In (c) and (d) the solutions are started from an initial condition with $w(r) = \cos(\pi r/2R)$, and are again shown at $t = 50$ and $t = 75$. The time step for this run was $\Delta t = 0.2$. All plots are computed on a 160×1024 mesh.

resolution. It is clear in these plots that the breakdown to the square cell state is less pronounced near the center, but that the breakdown near the outer boundary is the same in both cases. By further increasing the radial resolution, it is possible to prevent any discernible instability in the rolls near the center. We have also confirmed this by increasing the resolution in both the radial and angular coordinates. Therefore, we do appear to converge to the "correct" solution in the limit of higher spatial resolutions.

Our understanding of this phenomenon is not complete, but it is clear that the use of the polar coordinate system is partly responsible. We believe the effect is due to the loss of accuracy in the computation of derivatives in the nonlinear terms near the origin. Because of the clustering of the angular grid points in this region, it appears that a higher resolution in the radial direction is necessary to maintain reasonable accuracy.

Although it is reasonably simple to overcome this effect, increasing the radial resolution throughout the entire domain is generally unnecessary. In most circumstances, a resolution of eight points per half wavelength is sufficient to resolve the roll structures. When we set this resolution at the outer boundary, we actually obtain a higher resolution in the interior because of the "fanning out" of the radial lines θ = constant, from the origin. Therefore, little would be served by further increasing the resolution throughout the whole domain. Additionally, this higher resolution results in an increase in the complexity and memory requirements of the code, which eventually become prohibitive.

2.6 Introduction of a Varying Radial Mesh

In this section we consider two simple approaches to increasing the spatial resolution. Since we only require a higher resolution in the radial coordinate near the center of the domain, this leads to introducing a variable radial mesh.

2.6.1 Simple Two-Step Mesh

Our first attempt was to simply introduce a finer uniform mesh near the origin. This mesh would cover some inner fraction (between 1/4 to 1/2) of the domain, with the usual (coarser) uniform mesh covering the remainder. Because we continue to use uniform meshes, the changes are trivial except at the boundary of the two grids. Here it is

necessary to use finite differences over unequally spaced points to correctly approximate the derivatives. To keep the differencing consistent over the entire domain, only three-point stencils were used for first and second derivatives. This unfortunately leads to a reduction in the order of accuracy of the approximations (from second to essentially first), but only at the boundary point between the two grids. This drop in the accuracy is similar to one we would encounter at a physical boundary, so again, we do not expect it to reduce the overall order of accuracy of our method.

Our tests with this two-step uniform mesh showed an improvement near the origin, but the breakdown of the rolls now seemed to occur at the boundary between the fine and coarse mesh. Also, the breakdown was more severe when there was a greater difference between the mesh spacings of the two grids, but was not particularly sensitive to where this boundary occurred in the domain. This phenomenon shows the sensitivity of the equation to the computational mesh, but again, it is not clear why the breakdown occurs. Although we did not try to use more accurate approximations for the derivatives at the boundary point, we believe this may have helped in stabilizing the breakdown at the mesh boundary. However, we do not believe it would have been enough to completely eliminate the instability.

2.6.2 Smoothly Varying Mesh

The next natural step was to introduce a smoothly varying radial mesh. This allow us to increase the resolution in certain areas of the domain, without introducing any sharp changes in the mesh spacing. Several strategies are available, but a particularly general approach is to introduce a mapping or function between the radial coordinate, r and a fictitious variable, ρ. These would be related through a function h, $r = h(\rho)$, which we shall call the *radial mesh generating function.* The radial mesh points are then obtained by laying down a uniform grid in ρ. By doing this, we are able to ensure our method retains second order accuracy (when using three-point stencils), even though the points in the radial coordinate are no longer equi-spaced. We demonstrate this in the next section, as well as show how to do numerical differentiation and integration on this grid. We then describe appropriate conditions for the radial mesh generating function and consider some simple examples for h.

2.6.3 Numerical Differentiation and Integration using the Smoothly Varying Mesh

Let us first show that we can retain second order accuracy in the radial derivatives when using three-stencils to approximate the derivatives in ρ. We assume here that our mesh generating function $h(\rho)$ is sufficiently smooth. We compute the new approximations to the various derivatives with respect to r, in terms of the function $h(\rho)$ and the new variable ρ. First, we have,

$$\frac{\partial u}{\partial r} = \frac{1}{h'(\rho)} \cdot \frac{\partial u}{\partial \rho}, \tag{2.52}$$

$$\frac{\partial^2 u}{\partial r^2} = \frac{1}{[h'(\rho)]^2} \left[\frac{\partial^2 u}{\partial \rho^2} - \frac{h''(\rho)}{h'(\rho)} \frac{\partial u}{\partial \rho} \right]. \tag{2.53}$$

We now use standard second order central differences to approximate the derivatives in ρ (recall that the mesh in ρ is assumed to be equi-spaced). Letting $r_i = h(\rho_i)$, $h'_i \equiv h'(\rho_i)$, $h''_i \equiv h''(\rho_i)$ and $u_i \equiv u(r_i)$, we therefore have

$$\frac{\partial u_i}{\partial r} \approx \frac{1}{h'_i} \cdot \frac{u_{i+1} - u_{i-1}}{2\Delta\rho}, \tag{2.54}$$

$$\frac{\partial^2 u_i}{\partial r^2} \approx \frac{1}{(h'_i)^2} \left[\frac{u_{i+1} - 2u_i + u_{i-1}}{(\Delta\rho)^2} - \frac{h''_i}{h'_i} \cdot \frac{u_{i+1} - u_{i-1}}{2\Delta\rho} \right]. \tag{2.55}$$

When we compute the errors incurred by these approximations, we find,

$$\frac{\partial u_i}{\partial r} - \frac{1}{h'_i} \cdot \frac{u_{i+1} - u_{i-1}}{2\Delta\rho} = \frac{(\Delta\rho)^2}{6} \left(h'_i \frac{\partial^2 u_i}{\partial r^2} + \frac{h''_i}{h'_i} \frac{\partial u_i}{\partial r} \right) + O\left(\Delta\rho^3\right) \tag{2.56}$$

and

$$\begin{aligned} &\frac{\partial^2 u_i}{\partial r^2} - \frac{1}{(h'_i)^2} \left[\frac{u_{i+1} - 2u_i + u_{i-1}}{(\Delta\rho)^2} - \frac{h''_i}{h'_i} \cdot \frac{u_{i+1} - u_{i-1}}{2\Delta\rho} \right] \\ &= \frac{(\Delta\rho)^2}{12} \left(\frac{h_i^{(iv)}}{(h'_i)^2} \frac{\partial u_i}{\partial r} + \left(4\frac{h'''_i}{h'_i} + 3\left(\frac{h''_i}{h'_i}\right)^2 \right) \frac{\partial^2 u_i}{\partial r^2} + 6h''_i \frac{\partial^3 u_i}{\partial r^3} + (h'_i)^2 \frac{\partial^4 u_i}{\partial r^4} \right) \\ &- \frac{(\Delta\rho)^2}{6} \left(\left(\frac{h''_i}{h'_i}\right)^2 \frac{\partial u_i}{\partial r} + \frac{h''_i}{h'_i} \frac{\partial^2 u_i}{\partial r^2} \right) + O\left(\Delta\rho^3\right), \end{aligned} \tag{2.57}$$

so the approximations are certainly second order accurate in the new independent variable ρ. We notice how this reduces to the usual case of an equi-spaced grid when

$r = h(\rho) = \rho$, so that all derivatives of h, higher than first order, are zero. It is also worth noting that using linear functions for h is optimal, in the sense of minimizing the error in these approximations. In fact, the errors will become particularly large if the ratios h_i''/h_i', h_i'''/h_i' and $h_i^{(iv)}/h_i'$, are large.

When we tried implemementing this approach, we found that even choosing very smooth functions for h tended to yield poor approximations to the derivatives. A closer examination did indeed reveal that it was the moderate size of the ratios between higher order derivatives and the first derivative that was generally preventing us from gaining reasonable accuracy. This lead to the idea of simply trying to use linear functions where possible (usually at the two ends), with the major difficulty now being how to connect them smoothly. A more obvious way to find good candidates for h was in fact to look at the behavior of the first derivative of h. What we require is for the slope $h'(\rho)$ to be some constant for small values of ρ and some other constant for higher values of ρ with a (somewhat) smooth connection between them. The clear choice here is a tanh-like function for $h'(\rho)$. After experimenting with functions of this nature, a general improvement in the accuracy was found, but the magnitude of the error was still considerably larger in the regions where h was significantly nonlinear.

It should be noted, however, that this approach gave much more accurate results when used to do numerical integration over this variable grid. In these circumstances, the errors were not only second order accurate over the entire domain, but were also smaller in magnitude in regions where the grid was finer. Perhaps this is not surprising, given the smoothing behavior of any integration process. What we have then is a viable approach to at least do the integration parts of our problem. What was attractive here, was the fact that we were able to continue to use three-point stencils, and therefore, not significantly increase the complexity of the problem. However, a better approach to differentiation on this grid was still needed.

In order to determine derivative values more accurately, we decided to treat the grid as though it were nonuniform. Even though this would generally not be the case near the center and the outer boundary of the domain (as noted above), our approach here also takes advantage of any uniformity in the spacing of the grid. We use centered five-point stencils for the first and second derivatives, assuming now a nonuniform grid spacing.

This leads to essentially fourth and third order accurate approximations, respectively. In regions where the grid spacing is uniform, these orders of accuracy are increased by one.

Let us indicate, explicitly, how the first derivative is approximated. Let $\Delta r_i = r_i - r_{i-1}$ be the distance between the r_i and r_{i-1} grid points, and $u_i = u(r_i)$. Then we try to approximate the first derivative by

$$\frac{\partial u_i}{\partial r} \approx a u_{i-2} + b u_{i-1} + c u_i + d u_{i+1} + e u_{i+2}, \tag{2.58}$$

where a, b, c, d and e are constants to be determined. We Taylor expand each of the u's in the right-hand side, about $r = r_i$. For example,

$$\begin{aligned} u_{i-2} &= u_i - (\Delta r_i + \Delta r_{i-1})\frac{\partial u_i}{\partial r} + \frac{(\Delta r_i + \Delta r_{i-1})^2}{2}\frac{\partial^2 u_i}{\partial r^2} \\ &\quad - \frac{(\Delta r_i + \Delta r_{i-1})^3}{6}\frac{\partial^3 u_i}{\partial r^3} + \frac{(\Delta r_i + \Delta r_{i-1})^4}{20}\frac{\partial^4 u_i}{\partial r^4} + O\left((\Delta r_i + \Delta r_{i-1})^5\right). \end{aligned}$$

We form the right-hand side of Eq. (2.58) and collect the coefficients of u_i and its first four derivatives. Equating both sides of Eq. (2.58) clearly requires that all these coefficients are zero, except the coefficient of the first derivative, which should be one. This gives a 5×5 linear system which can then be solved for a, b, c, d and e. Note that in this approach, we are able to correctly account for all terms up to the fifth order derivative. Thus, the resulting approximation given by the right-hand side of Eq. (2.58) will be essentially fourth order accurate (after we divide through by the coefficient of the first derivative). When the points are equi-spaced, the coefficient corresponding to the fifth order derivative will automatically be zero, due to symmetry. Thus, the order of accuracy of the approximation increases by one.

The second derivative is obtained in a similar way. Note, however, that its order of accuracy is one lower than the corresponding first derivative because we need to divide through by its coefficient, which is quadratic rather than linear, in the grid spacings Δr_i.

We also note that this five-point stencil cannot be used at the inner most grid points. At these points, we revert back to using standard three-point stencils. Since we expect the mesh to be uniform in these places, we are still able to achieve second order accuracy at these points.

To summarize then, we assume that the radial coordinate is given by some mapping $r = h(\rho)$, where h is free to be chosen. The radial mesh points are obtained by evaluating h at equi-spaced values of ρ. The relationships (2.54) – (2.55), obtained above for the derivatives with respect to r, in terms of h and ρ, are then used to do any integration on this grid, while the derivatives are approximated directly from the location of the nonuniform grid points r_i, without any knowledge of this mapping h.

2.6.4 Simple Choices for Mesh Generating Functions

In the preceding sections, we have already suggested several characteristics we expect the function h to have. In this section we will attempt to use these to help us determine some suitable choices for this function.

Our initial choice above, of a tanh-like function (for the derivative of h), is such an example. However, an even simpler choice is to use linear pieces at the ends, connected in some (reasonably) smooth way through the interior. This choice is more appealing because it offers a greater degree of flexibility. We found when trying to use the tanh-like function, only two parameters were essentially available to adjust the shape of the curve. The function is given by:

$$h(\rho) = \left(\frac{1-c}{2a}\right) \ln\left[\frac{\cosh[a(\rho-b)]}{\cosh(ab)}\right] + \left(\frac{1+c}{s}\right)\rho. \tag{2.59}$$

Here, the parameter c is taken to be less than 1, and essentially gives the slope of the nearly linear piece at the lower end. The other two parameters, a and b, are used to adjust the shape of the curve. Roughly speaking, a controls the physical extent over which the two end-pieces are joined and b controls the positioning of the variability of the mesh.

It was then particularly difficult to find parameters which would give a reasonably gradual change in the grid spacing for r, if we also wanted reasonably linear pieces at the ends. The reasons for wanting linear functions for h were alluded to above. We reiterate these reasons again to make it clear why this choice is desirable. Firstly, if h is linear, then the truncation error, given by (2.54) and (2.55), will generally be lower. Secondly, linear functions for h lead to uniform grid spacings in r, so our approximations to the

derivatives using five point stencils will generally have higher orders of accuracy. Given these, it seems clear how we should proceed.

The difficulty that remains is in connecting these two linear pieces. We first tried to use a polynomial to do this, ensuring that function, first and second derivative values were continuous. This leads to a quintic polynomial, which surprisingly, does not connect them in a truly monotonic way. By this we mean that we observe a change in curvature over its domain. Although there is no reason why this is unacceptable, it appears that this is unnecessary if all we require is a smooth connection between the two linear pieces. If we no longer require continuity in the second derivative of h, then a cubic polynomial can be used. This too, however, has a change in its curvature and we again discard it as a possibility.

Our next attempt was to use a circular arc to connect the linear ends. This again would not give a continuous second derivative for h, but it was hoped that the discontinuous jumps would be small. This would be the case if the arc had a large radius. Although we were not able to arbitrarily specify this radius, in practice it will be large if the connection occurs over a reasonably large region. For this we reason, we basically divided the range of r (which is just the radius of our disk) into thirds. The circular arc would then cover the region over this middle third, with linear pieces over the first and last thirds. We would generally choose the slope of the "outer" linear piece to be one, and the "inner" slope to be a fraction $1/k$, where $k = 2, 3, \ldots$. This corresponds to the inner third of the radial mesh having k-times the resolution of the outer third. Our solutions on meshes generated from this approach have been found to be more than satisfactory.

2.7 Adaptive Time Stepping

The fully implicit code provides a highly stable integration scheme, which appeared to be stable for time steps even as large as $\Delta t = 100$. When the scheme did breakdown, it was usually due to a lack of convergence in the GMRES iteration, which was halted if the number of iterations exceeded more than 30. This in essence signifies a loss of stability in the scheme. Given the stable nature of this scheme, and the need to integrate the equations over very long time frames, a simple adaptive time stepping procedure was

implemented. This involved computing the solution at some time t, using a step of size Δt and the solution at the same time using two steps of size $\Delta t/2$. If a local measure of error between these two solutions was below a specified tolerance (usually 1% of the two-norm of the solution), then the time step was doubled to $2\Delta t$ and the same accuracy test performed. Since the dynamics of the pattern formation tends to decrease as time increases or if ϵ is reduced, this test is performed to determine an appropriate time step size, comparable to the dynamics in the solution.

The simple adaptive time stepping procedure was implemented in two ways. The first was to simply conduct the test after a specified number of time steps. In general we found that, after the initial transients in the dynamics had dissipated, it was likely that the time step could be doubled as often as required, and there seems to be little sign of an upper bound on the time step. This provides some justification that the scheme achieves almost unconditional stability. In practice, we would not allow for too large a time step since the method is only second order accurate in time, and the simple accuracy test we perform clearly only checks the accuracy locally in time. In Fig. (2.3) we show a plot of the time step trace on logarithmic scales in a typical run.

The persistent dynamics expected in these systems is another reason that simply checking the accuracy at specific times in the evolution may not be a particularly good method of choosing an appropriate time step. The possibility of local changes in the patterns happening on time scales that are less than the current time step would lead to inaccurate solutions that the simple test above would be unable to detect. Therefore, as an alternative or additional criterion for determining when the accuracy test is performed, we compute a measure of the rate of change of the solution after each time step. This simply involves obtaining a local measure of $\partial\psi/\partial t$ by evaluating the right-hand side of Eq. (2.1) after each time step. Any large deviations in this value indicates the possibility of rapid changes in the solution, and therefore the need to check the accuracy at the current time step.

In Fig. (2.4) we show a time step trace for a typical run using this particular scheme. The two spikes seen at $t \approx 1200$ and $t \approx 1800$ clearly shows the capability of this scheme to detect rapid changes in the solution and change (in this case halve) the time step accordingly. We see that the time step is quickly doubled again and shows that the

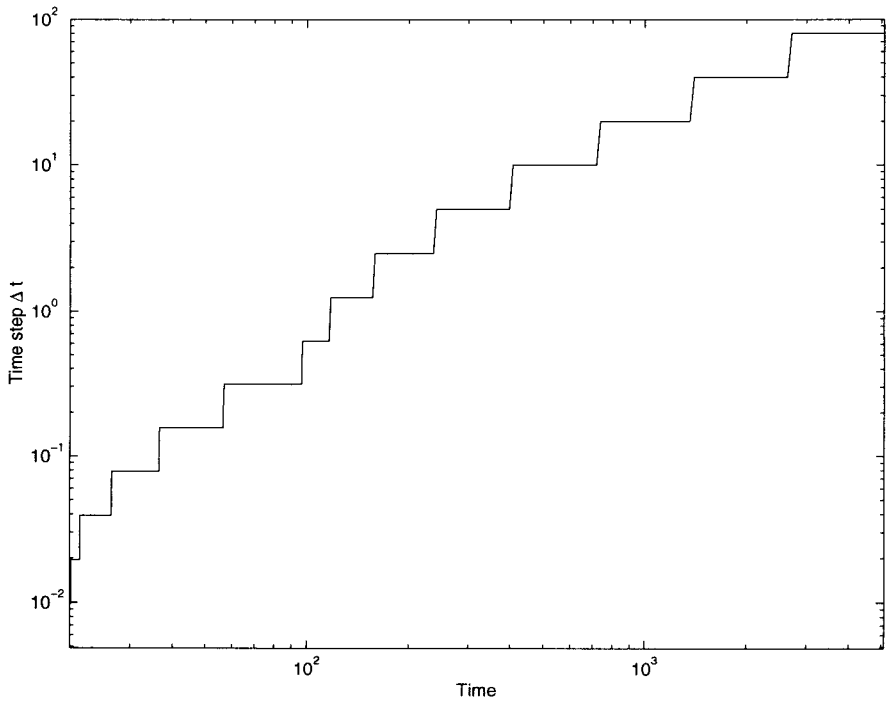

Figure 2.3: Example of the simple adaptive time stepping procedure shown on logarithmic scales. The time step is doubled or halved according to whether the solutions at Δt and $2\Delta t$ or Δt and $\Delta t/2$, respectively, differ by less than 1%. In this case, the accuracy test is performed every 50 time steps. For this particular run, $\epsilon = 0.01$.

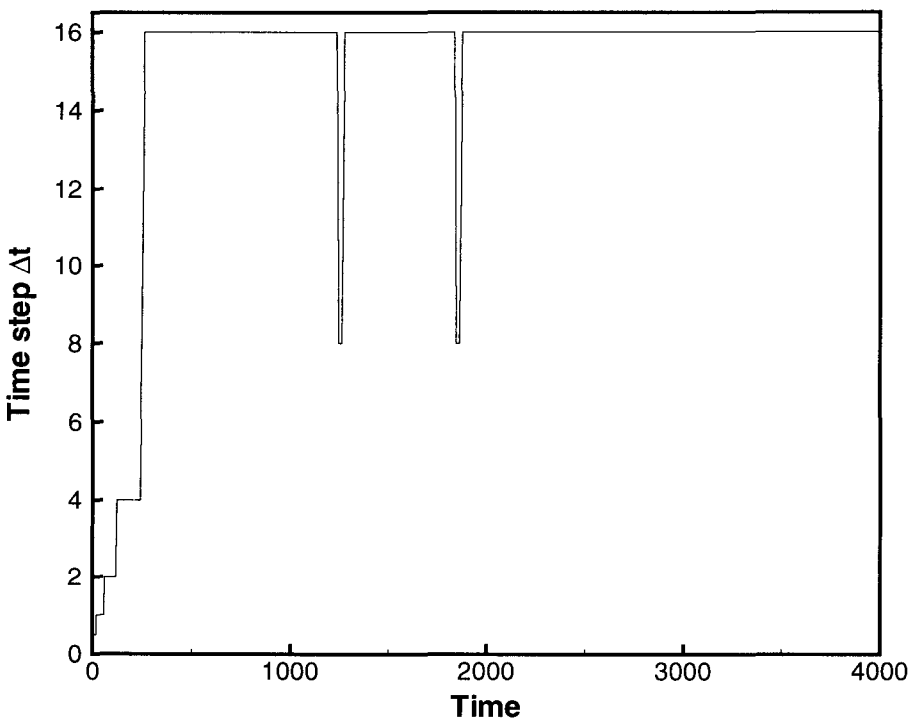

Figure 2.4: Example of adaptive time stepping procedure based on checking the rate of change in the solution. At each time step, $\partial\psi/\partial t$ is computed and monitored for large changes (relative to $\|\psi\|_2$). If a significant change is detected, the accuracy test is used to determine if the time step is doubled, halved or left unchanged. The two spikes seen indicates that the scheme always tries to use the largest time step size compatible with the dynamics. For this particular run, $\epsilon = 0.05$.

scheme is successful at choosing the largest step compatible with the dynamics in the system. In general, we did not find many such large changes in the long time evolutions and the usual accuracy check after a specified number of time steps was usually sufficient for providing the appropriate time step size.

Chapter 3

Data Analysis and Numerical Results

3.1 Qualitative Observations

In this section we briefly describe some qualitative features of the solutions. Our primary goal is to confirm that our numerical solutions qualitatively reproduce the behavior seen in the Küppers-Lortz instability. The experimental work of Hu *et al.* [31, 33] should be consulted for comparison. The appropriate value of the parameters g_2 and g_3 in our model equation Eq. (2.3) are chosen to ensure that we are in the appropriate KL regime, as indicated in the work of Cross *et al.* [18]. We also consider the trends as we vary the control parameter ϵ and the cell size, to ensure our solutions are behaving as expected.

A typical evolution in the KL state is shown in Fig. (3.1). This should be compared with Fig. (3.2) which is taken from the experimental work of Hu *et al.* [33]. The similarity with experiments is truly remarkable. Here we see that in the KL regime, several domains of essentially parallel rolls coexist in the cell. The domains are dynamic and grow and shrink in size due to the presence of the other domains. Sharp boundaries exist between the various domains and it is through the propagation of these boundaries that the orientation of the rolls change in any particular part of the cell over time. It should be noted that the boundaries appear sharp relative to the size of the cell, but generally have a thickness on the order of one or two roll widths. Since our computed solutions have at least 8 points per roll width, these boundaries are more than adequately resolved in our calculations.

We notice that the rolls are mostly nucleated from the boundary in this particular evolution. However, at higher values of ϵ, spontaneous generation of new rolls has been observed in the interior of the cell. This is also a feature of the experiments. Thus, we are able to reproduce many of the phenomena found in the experimental system.

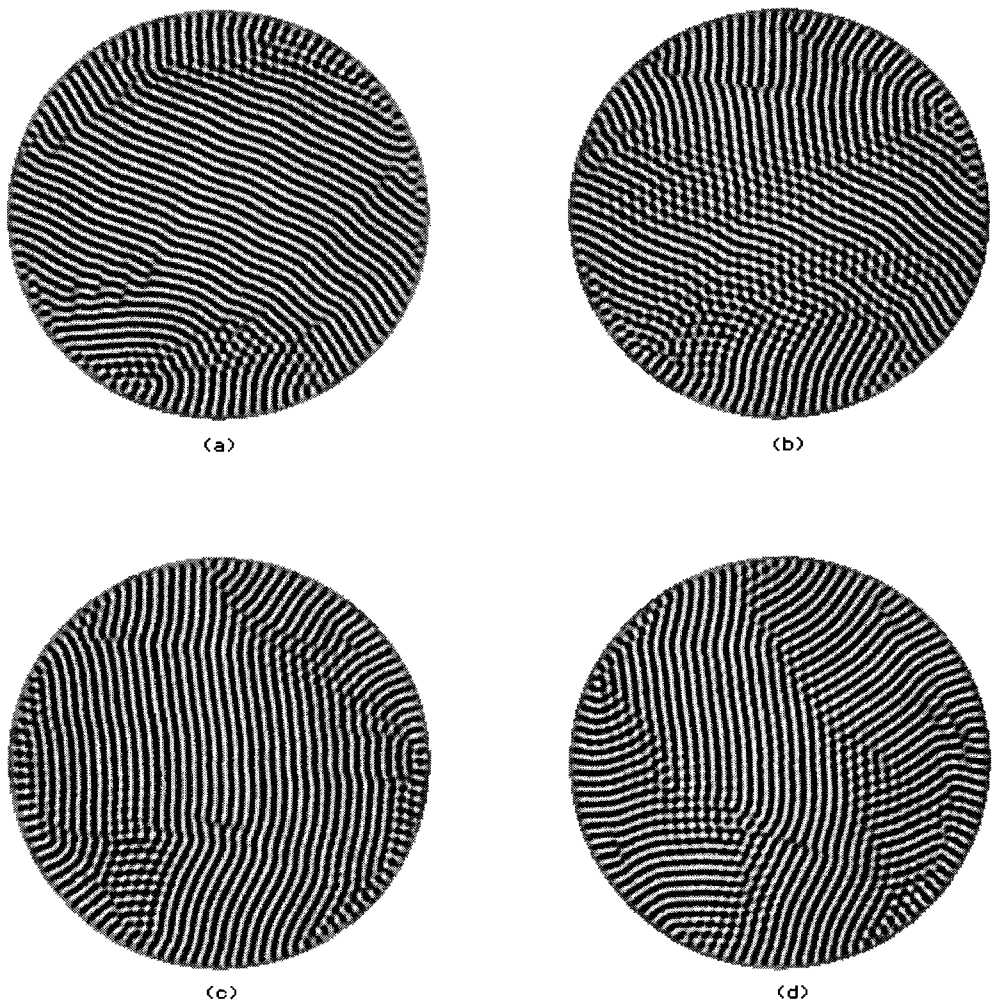

Figure 3.1: Typical time evolution in the KL regime. The evolution is shown at (a) $t = 10460$, (b) $t = 10780$, (c) $t = 11000$ and (d) $t = 11420$. The parameters are $\epsilon = 0.05$, $g_1 = 1$, $g_2 = -2.60$ and $g_3 = 1.5$ in a cell of radius 40π. In these grey-scale contour plots of the field $\psi(x, y, t)$, black corresponds to a maximum field value of 0.248 and white to a minimum value of -0.247.

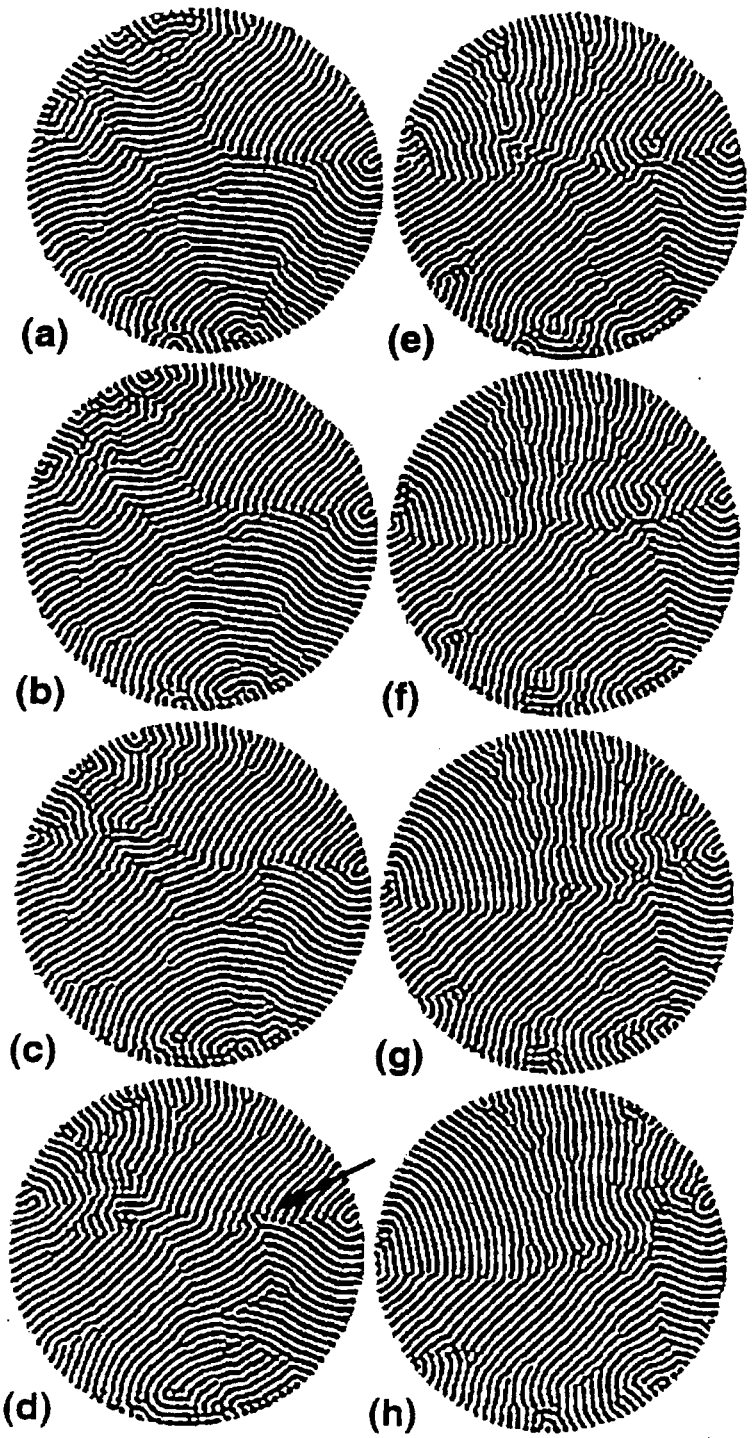

Figure 3.2: Time sequence of images from experiments for a cell of aspect ratio 40, showing Küppers-Lortz domains and dislocation-defect motion. The images are approximately 40 seconds apart. Reprinted from [33].

3.1.1 Variations with the Control Parameter ϵ

The control parameter ϵ provides a measure of the distance from onset. Thus, as ϵ increases, the system is driven further and further from equilibrium, and we expect to see a generally more disordered pattern. Indeed this is what is found in experiment, and here we show that the same trend is also seen in our simulations.

In Fig. (3.3), we show the configurations obtained at three different values of ϵ. As expected, when ϵ is very small, the cell is filled almost entirely with a single set of parallel rolls. As ϵ increases, we see that more and more sets of rolls begin to fill the cell. Consequently, the size of each of these domains shrinks. What is not shown here is the dynamics of the domains which grow and shrink due to the propagation of the walls of the domains. This behavior is indicative of the KL state, and is generally only observed for $\epsilon < 1$.

3.1.2 Effects of Different Cell Size

We have computed solutions in cells with radii $R = 30\pi$, 40π and 50π, corresponding to cells with aspect ratios of 30, 40 and 50 respectively. Much experimental work [31, 33] has been conducted in cells of aspect ratio 40, so this should allow us to to make meaningful comparisons with experiments, while also allowing us to investigate possible effects due to finite geometries. Unfortunately, our maximum cell size is restricted by computational resources, although we have been able to perform a small number of runs in a cell of radius $R = 80\pi$ (see later results).

Since we are interested in determining if finite size effects are important in this problem, this range of cell sizes gives us an opportunity to observe the changes with different cell sizes. We find that for the same value of ϵ, the patterns look qualitatively the same. In Fig. (3.4) we show that patterns at the same ϵ look very similar regardless of the cell size. In particular, at this larger value of $\epsilon = 0.2$, the domains of rolls appear to be of comparable size in each of the different cells. We note, however, that this situation changes as $\epsilon \to 0$. As ϵ decreases, the domains become larger (see Fig. (3.3)) and the size of the cell clearly begins to constrain the size of the domains that are possible. This is shown in Fig. (3.5), where it is clear that, although the patterns have similar configurations, the size of the largest domains are influenced by the size of the cell. This

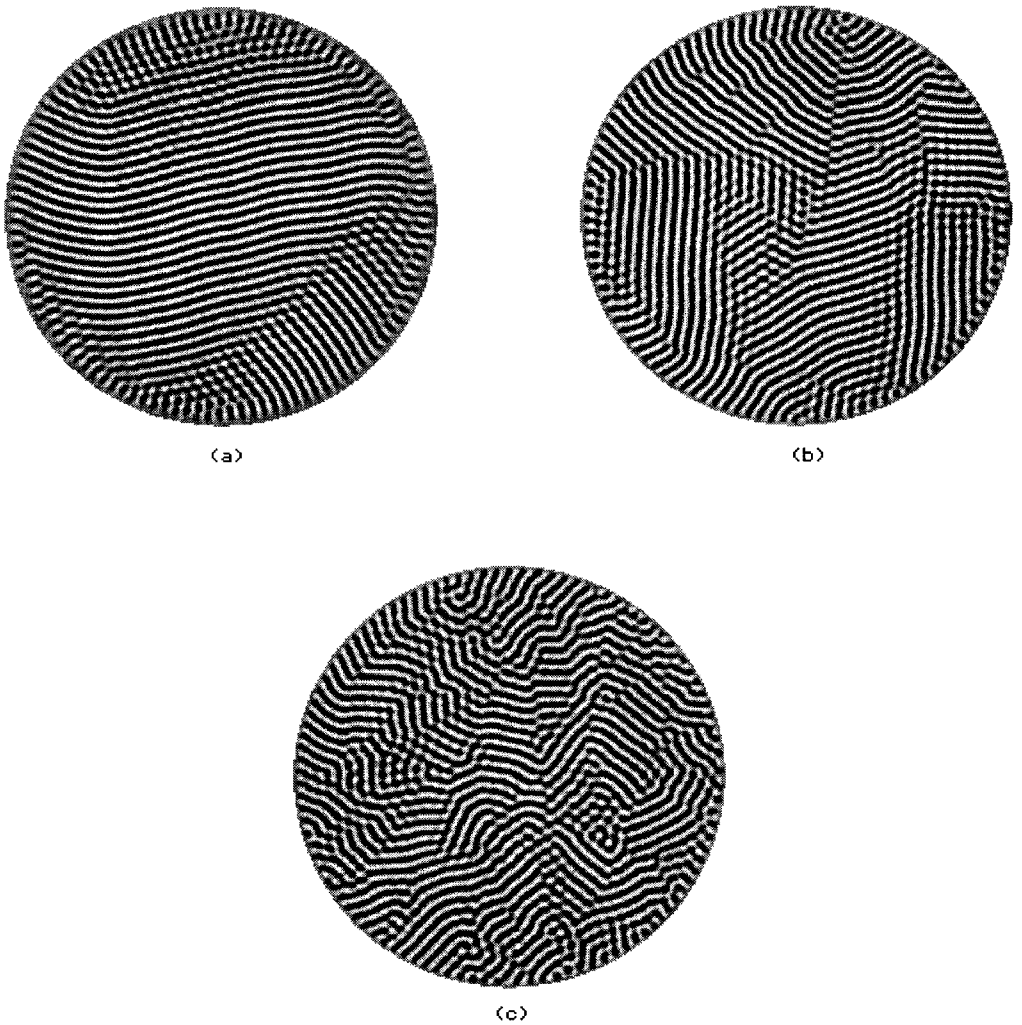

Figure 3.3: Snapshots of contours of the field $\psi(x, y, t)$ for different values of ϵ, showing the trend to smaller domains as ϵ increases. (a) $\epsilon = 0.01$ (at $t = 27000$), black corresponds to a maximum of 0.100 for ψ, white to a minimum of -0.100, (b) $\epsilon = 0.1$ (at $t = 7000$), black corresponds to a maximum of 0.337 for ψ, white to a minimum of -0.334, (c) $\epsilon = 0.3$ (at $t = 310$), black corresponds to a maximum of 0.617 for ψ, white to a minimum of -0.621. The other parameters are $g_1 = 1$, $g_2 = -2.60$ and $g_3 = 1.5$ in a cell of radius 40π.

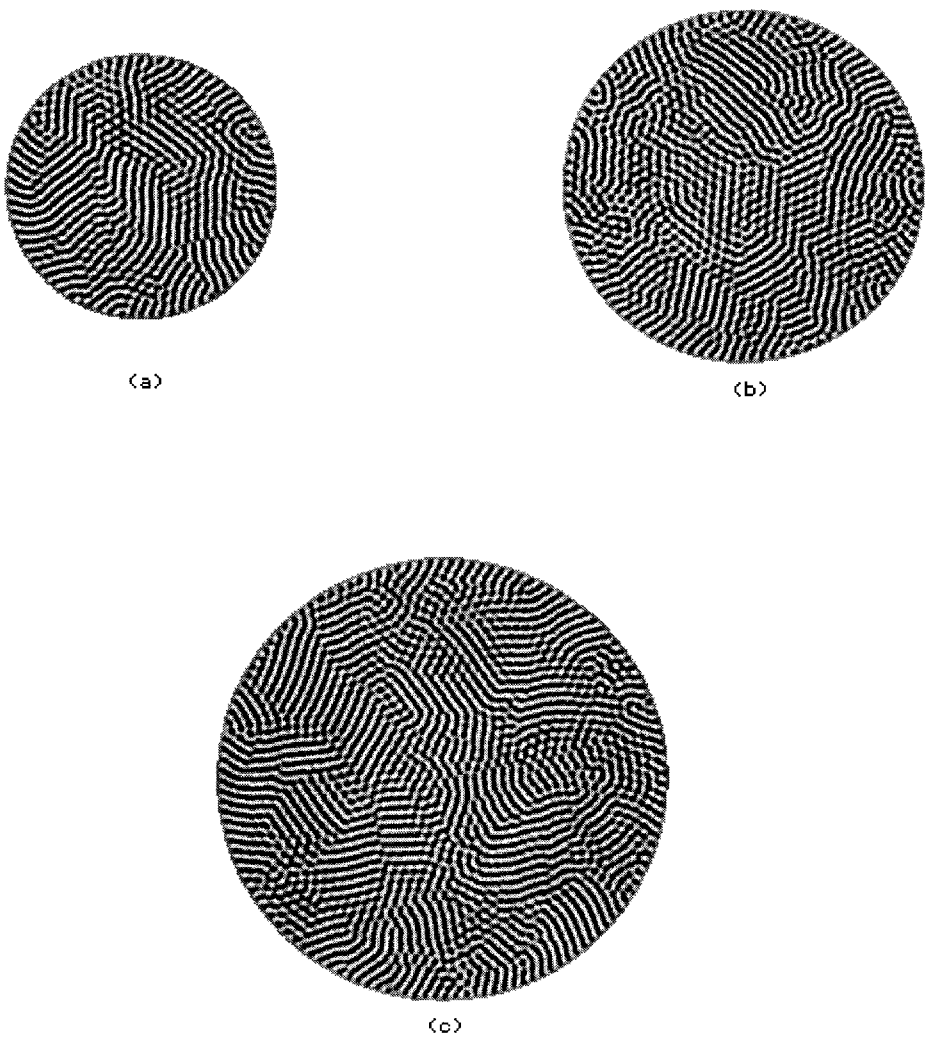

Figure 3.4: Comparison of solutions in cells of different size for the same value of $\epsilon = 0.2$. The cells have radii (a) 30π, (b) 40π and (c) 50π. The other parameters are the same as in Fig. (3.3). Black corresponds to a maximum field value of 0.496 and white to a minimum of -0.501.

is studied more quantitatively later in this chapter.

3.2 Quantitative Data Analysis and Pattern Diagnostics

In order to better classify the many complicated patterns that develop in Rayleigh-Bénard convection, experimentalists have developed ways to analyze the patterns in a quantitative way [31, 33]. In particular, Hu *et al.* [33] have done a detailed quantitative study of the Küppers-Lortz instability from which we hope to draw some comparisons.

To this end, we have developed similar diagnostic analyses for our simulations. The primary analysis is a spatial Fourier transform of the pattern $\psi(x, y, t)$,

$$\Psi(\mathbf{k}, t) = \Psi(k_x, k_y, t) = \int_{-\infty}^{\infty} \int_{-\infty}^{\infty} \psi(x, y, t) e^{i(k_x x + k_y y)} \, dx dy. \tag{3.1}$$

We assume that $\psi(x, y, t) = 0$ for all values of x and y outside the circular cell $x^2 + y^2 \leq R^2$, where R is the radius of the cell. Thus the integration in Eq. (3.1) need only be performed over any finite region in space incorporating the cell region. It is convenient to choose the square region $D = \{(x, y) | -R \leq x \leq R, -R \leq y \leq R\}$, and use the fast Fourier transform (FFT) to compute Eq. (3.1). Note that we first interpolate the values of ψ from our computational polar mesh to a uniform mesh in (x, y). This is accomplished using a piecewise bicubic interpolation scheme. A resolution comparable to that used in the computation (about 8 points per half wavelength) is used to cover the square region D. For a cell of radius $R = 40\pi$, we have used 512×512 points.

As with experiments, our patterns are actually prefiltered with a 71% Hanning window before the Fourier transform is taken. The Hanning window is applied by multiplying the pattern $\psi(r, \theta, t)$ by a radial function defined by

$$H(r) = \begin{cases} [1 + \cos(\pi r / r_0)]/2 & \text{for } r \leq r_0, \\ 0 & \text{for } r > r_0 \end{cases} \tag{3.2}$$

where $r_0 = 0.71R$ and R is the radius of the cell. The effect of the Hanning window is to de-emphasize any contributions from near the boundary. Thus, the Fourier transform which results only essentially shows the dominant orientations from the center of the cell. For this reason, it was necessary for us to ensure that our numerical approach did

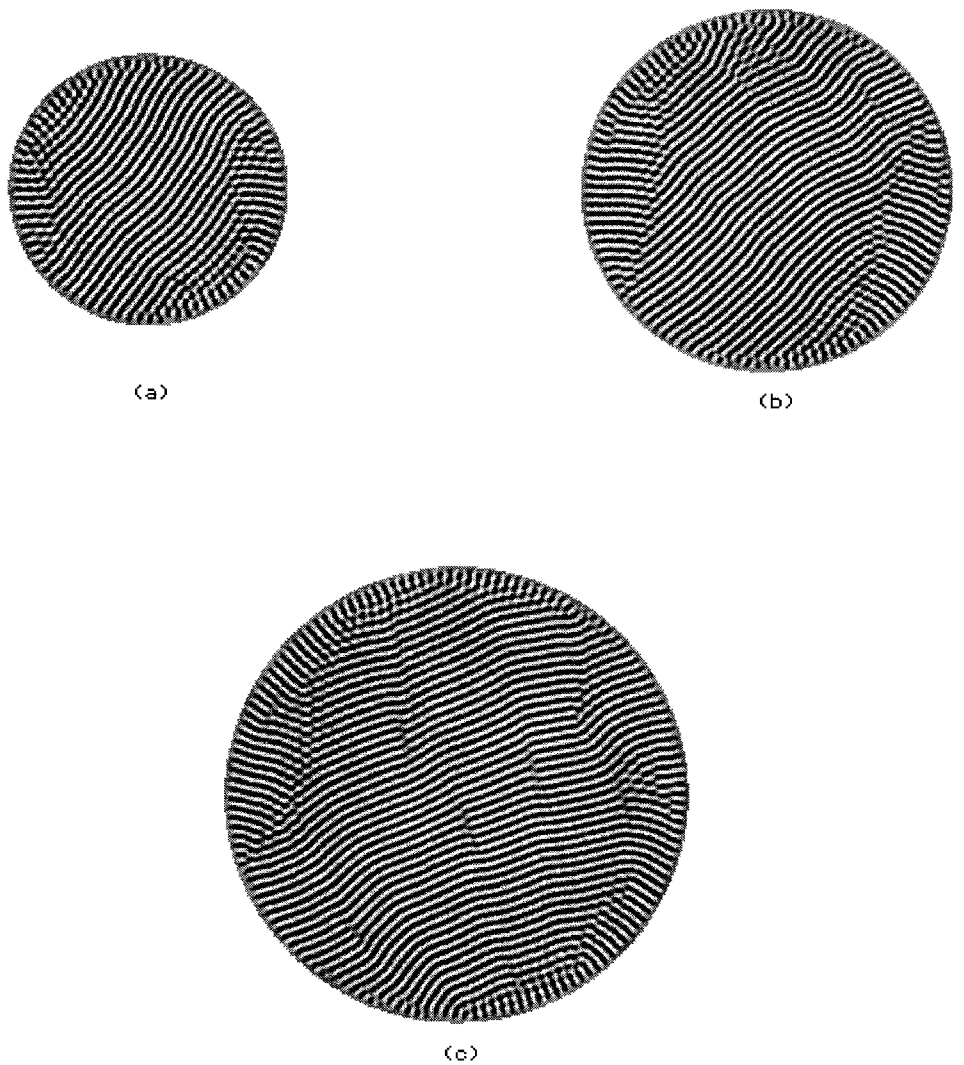

Figure 3.5: Comparison of solutions in cells of different size for the same value of $\epsilon = 0.03$. The cells have radii (a) 30π, (b) 40π and (c) 50π. The other parameters are the same as in Fig. (3.3). Pattern configurations are similar, but larger domains can be observed in the larger cells. Black corresponds to a maximum field value of 0.180 and white to a minimum of -0.175.

not generate any spurious results (i.e., non-physical generation of rolls) near the center of the cell.

Since the patterns consist primarily of domains of straight rolls, these would manifest themselves as regions in wave space $\mathbf{k}$, where the magnitude of the Fourier transform is large. Our model equation has been scaled so that these regions are concentrated about the circle $|\mathbf{k}| = 1$. Then rolls of a particular orientation give rise to a large concentration at a particular angle on this circle in wave space. This can be seen in Fig. (3.6), which shows a snapshot of a pattern and the corresponding Fourier transform. It should be noted that there are generally domains in the pattern oriented at 60 degrees to each other. This is a consequence of the model and the particular parameter values chosen. The three-mode switching is a feature of experimental patterns and it is a promising sign that our simulations are able to capture this phenomenon.

It should also be noted that one drawback of the Fourier transform analysis is that local spatial information is lost. Thus, we cannot distinguish rolls with the same wave vector in several disconnected domains from rolls in a single larger domain. Nevertheless, it provides a simple and effective method of determining the "average" roll orientation of the patterns.

3.2.1 Angle Time Plots and Their Auto-correlations

In order to better determine temporal trends in the patterns, we need a way of displaying the evolution of the average roll orientation. A particularly convenient way to do this is to integrate the Fourier intensity $|\Psi(\mathbf{k}, t)|$, over radial coordinates to give the angular intensity as a function of the direction (given by the unit vector $\hat{k}$ with $\mathbf{k} = k\hat{k}$)

$$\bar{S}_1(\hat{k}, t) = \int 2\pi k \, dk \, |\Psi(k, \hat{k}, t)|. \tag{3.3}$$

By plotting this as function of time, we should be able to clearly see the evolution of the average domain structure. We show an example of this **angle time plot** in Fig. (3.7). This is essentially the same plot seen in the experimental work of Hu *et al.* [33], who call them angular distributions $F(\theta, t)$. Similar plots are also considered in the numerical work of Cross *et al.* [18].

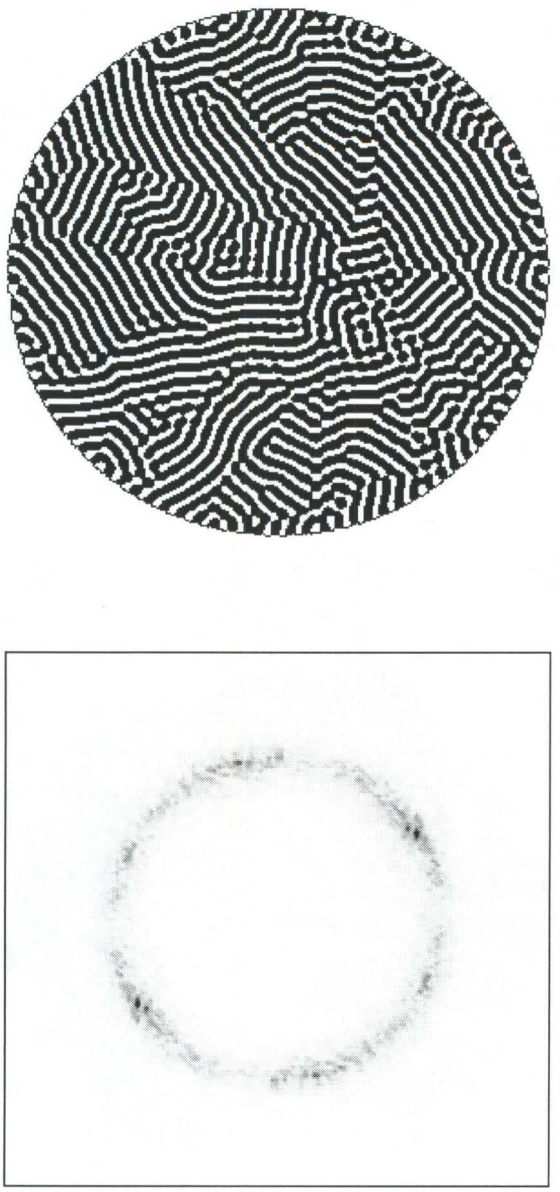

Figure 3.6: Snapshot of the field $\psi(x, y, t)$ (top panel) and its corresponding Fourier transform (bottom panel) after a time 2000 from random initial conditions. The parameters are $g_1 = 1$, $g_2 = -2.60$, $g_3 = 1.5$ and $\epsilon = 0.3$, in a cell of radius 40π. In the field representation (top panel) black denotes positive values and white negative values. In the bottom panel the full range of wave vectors shown is ± 1.6 in each direction k_x, k_y.

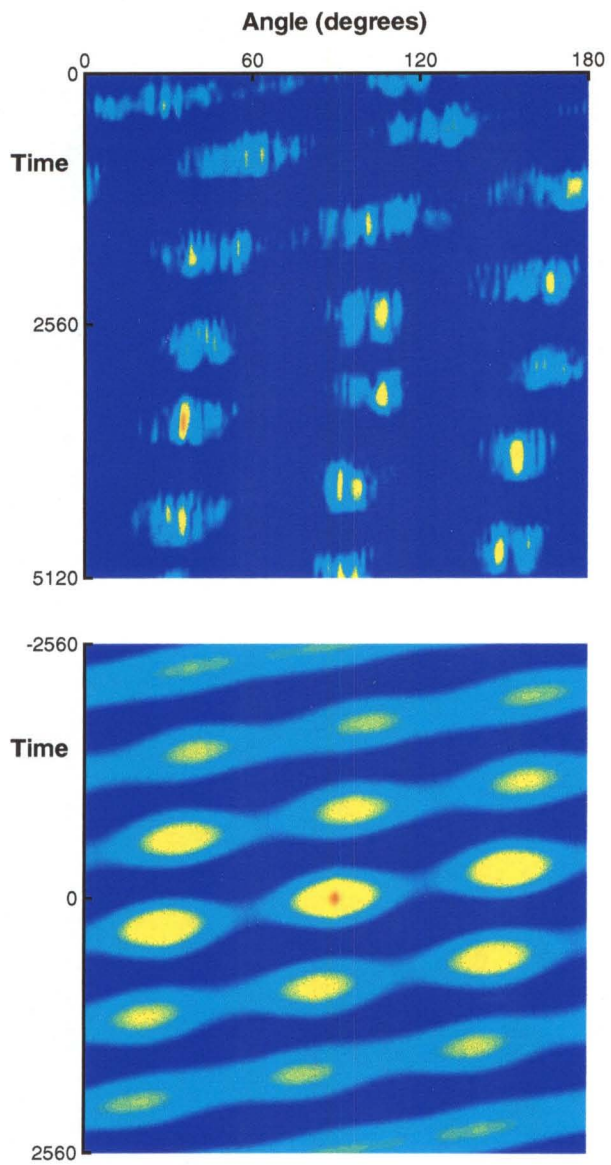

Figure 3.7: Angular Fourier intensity versus time and its auto-correlation. Top panel is a color scale plot of the radially integrated Fourier intensity (blue, zero; red, maximum intensity) as a function of the angle θ_k of the wave vector, plotted against time for an interval of 5,120 starting at time 800, in a cell of radius 30π. The other parameters are $\epsilon = 0.1$, $g_1 = 1$, $g_2 = -2.60$ and $g_3 = 1.5$. The lower panel is the auto-correlation of the top panel, with the origin (θ_k, $t = 0$) in the center of the plot.

To accentuate the details in the angular distributions $F(\theta, t)$, auto-correlations (labelled $C(\delta\theta, \delta t)$ by the experimentalists) of this plot are computed. This is simply the square of the Fourier transform of $F(\theta, t)$ treated as a two-dimensional image. Notice that we shift the auto-correlation so that the largest contributions now occur at the center of the plot. From these, it is particularly easy to see the switching behavior of the domains. The switching behavior manifests itself as a sequence of bright spots separated by (θ_s, τ_s) offsets. Here θ_s represents the switching angle which we see is close to 60°. We also notice that it is possible for there to be an overall drift in the dominant orientation. Thus, after any two consecutive switches, it is not necessary to return to the same dominant orientation. This is also seen in the experimental results. τ_s gives a characteristic switching time, but it is important to note exactly how this is being determined. As we have already mentioned, there is a loss of local spatial information after we take the Fourier transform. Therefore, our angle time plots $F(\theta, t)$ and auto-correlations $C(\delta\theta, \delta t)$ do not show the switching behavior of any one particular domain. Instead, it is a measure of the average stripe orientation, and therefore our switching angle and switching time are also only average measures of these quantities. Nevertheless, they provide a good quantitative way of determining the important characteristics of the particular system under study.

3.2.2 Structure Function $S(\mathbf{k})$ and the Correlation Length ξ

Of particular interest to us is a way to obtain some measure of the size of the domains in our cell. This leads to defining a correlation length, and we again follow the work of the experimentalists [40]. They begin by defining the structure function $S(\mathbf{k})$, which is simply the time average of the square of the modulus of the spatial Fourier transform. They also consider averaging this azimuthally to obtain a function which depends only on $k \equiv |\mathbf{k}|$. In cases where $S(\mathbf{k})$ is nearly azimuthally symmetric, $S(k)$ provides a convenient way to represent the wavespace information.

In terms of the first two moments,

$$\langle k \rangle \equiv \frac{\int |\mathbf{k}| S(\mathbf{k}) d^2\mathbf{k}}{\int S(\mathbf{k}) d^2\mathbf{k}} = \frac{\int_0^\infty k^2 S(k) dk}{\int_0^\infty k S(k) dk} \tag{3.4}$$

and

$$\langle k^2 \rangle \equiv \frac{\int |\mathbf{k}|^2 S(\mathbf{k}) d^2\mathbf{k}}{\int S(\mathbf{k}) d^2\mathbf{k}} = \frac{\int_0^\infty k^3 S(k) dk}{\int_0^\infty k S(k) dk} \tag{3.5}$$

of $S(\mathbf{k})$, an average wave vector $\langle k \rangle$ and the correlation length

$$\xi \equiv \left[\langle k^2 \rangle - \langle k \rangle^2 \right]^{-1/2} \tag{3.6}$$

can be defined. Note that although the integrals defining the first two moments are over a semi-infinite range, they are clearly not computed on this range. In our case, we integrate only as far as we can in wave space which is determined by the (finite) Fourier transform that we calculate. If we take N points in the sample and R is the radius of the cell, then the maximum wave number is given by $k < \pi N/R$.

An alternative definition of the correlation length is considered by Cross *et al.* [18]. This is defined in terms of a filtered Fourier transform which is the product of the Fourier transform $\Psi(\mathbf{k})$ of the field $\psi(\mathbf{r})$ with a Gaussian filter centered at some angle θ_f around the $k = 1$ circle in Fourier space:

$$\Psi_f(\mathbf{k}, \theta_f) = e^{-(\mathbf{k}-\mathbf{k}_f)^2/\sigma^2} \Psi(\mathbf{k}), \tag{3.7}$$

where $\mathbf{k}_f = (\cos\theta_f, \sin\theta_f)$ and σ sets the width of the filtering function. If we perform the inverse Fourier transform with respect to $\mathbf{k}$ on $\Psi_f(\mathbf{k}, \theta_f)$ we get a function $\psi_f(\mathbf{r}, \theta_f)$ that is large in magnitude in those domains where the stripe normal is close to the θ_f direction. From this filtered field $\psi_f(\mathbf{r})$, the correlation function for a particular filtering angle θ_f is defined as

$$C(\mathbf{R}; \theta_f) = \langle \psi_f(\mathbf{r}, t; \theta_f) \psi_f(\mathbf{r} + \mathbf{R}, t; \theta_f) \rangle_{\mathbf{r},t} - \langle \psi_f(\mathbf{r}, t; \theta_f) \rangle^2_{\mathbf{r},t}, \tag{3.8}$$

and the filtered correlation function is defined as this quantity averaged over θ_f

$$C_f(\mathbf{R}) = \frac{1}{n_f} \sum_{f=1}^{n_f} C(\mathbf{R}, \theta_f) \tag{3.9}$$

summing over n_f discrete filtering angles. Typically 8 to 12 θ_f are used in their cal-

culations. By plotting C_f for separations $\mathbf{R}$ along the x and y directions gives a curve which decays approximately exponentially as the separation increases. The correlation length is then taken as the width at half the maximum of C_f. We have not considered this for our purposes since we hope to draw more direct comparison from the experiments. Thus, where possible, we have tried to implement the quantitative analyses of the experimentalists.

3.2.3 Domain Switching Frequency ω_a

We saw from the angle time plots $F(\theta, t)$ and auto-correlations $C(\delta\theta, \delta t)$ how a characteristic switching time could be determined. However, often in experiments, they are in regimes where the Küppers-Lortz instability is not fully developed (usually when they are below the critical rotation rate) and the pattern rotation seen in these plots is most likely not due to a switching orientation of domains. In fact, domains may not be the primary structure in such cases, and it is therefore difficult to attribute a characteristic switching time to such pattern behavior. However, it is still possible to consider a domain switching frequency ω_a as the inverse of the slope of the bright lines in the angle time plots and auto-correlations. In the fully developed KL state, this will be proportional to the inverse of the characteristic switching time since the domain switching angle will be reasonably constant.

In our simulations, we have restricted ourselves to a parameter regime where the KL state is active and therefore it is possible for us to directly determine a switching time. However, to be consistent with experiment, and since the switching time and switching frequency are so closely related in this regime, we only consider computing ω_a. We note again that this is determined from the Fourier transform analysis, and therefore only represents an average, and not a switching time for any one particular domain. The domain switching frequency is therefore also only an average measure of the true switching frequencies that may be seen in the patterns.

3.3 Time and Length Scales

Our primary purpose for studying these models is to try to establish time and length scales for this problem. This is of interest because there are both theoretical and experiment results for these quantities, which do not agree. Since we are not modeling the full fluid systems, we do not fully expect to reproduce the same scalings seen in experiment, but it is interesting to see how finite size effects might alter the scalings predicted by theory based on results in infinite size cells. In particular, it is interesting to determine whether such finite size effects might be responsible for the discrepancy between the theoretical and experimental scalings.

3.3.1 Experimental and Theoretical Predictions

In the work of Hu *et al.* [31, 33], they have established time and length scales in rotating Rayleigh-Béard convection based on the measurements described in the previous sections. Their findings suggest that the data are not particularly well described by the theoretical predictions. They have suggested alternative scalings which fit the data better, but which facilitates the need for further explanation.

The theoretical scalings are based on general properties of Ginzburg-Landau models which hold only in the limit of small ϵ and in the absence of boundaries. The theory predicts that $\omega_a \propto \epsilon$ and that $\xi \propto \epsilon^{-1/2}$, so it is convenient to plot ω_a and $1/\xi^2$ as functions of ϵ to see if the data fall on straight lines. For small ϵ, Hu and his co-workers found that a linear relationship was a reasonable fit to the data, but the lines did not pass through the origin. This indicates that there are nonzero correlation lengths and switching times at $\epsilon = 0$, contrary to what is expected theoretically. In order to search for a scaling which fit the data better, they included higher order corrections to the scalings of the form

$$(1/\xi)^2 = X_0\epsilon\left(1 + X_1\epsilon + X_2\epsilon^2\right), \tag{3.10}$$

$$\omega_a = \omega_{a,0}\epsilon\left(1 + \omega_{a,1}\epsilon + \omega_{a,2}\epsilon^2\right). \tag{3.11}$$

However, in doing this, they found that the coefficients X_1, X_2, $\omega_{a,1}$ and $\omega_{a,2}$, corresponding to these higher corrections, had to be considerably larger than $O(1)$. An alternative

is to consider a different scaling at the lowest order. A particularly good fit to their data is obtained with the scalings $\omega_a \propto \epsilon^{0.6}$ and $\xi \propto \epsilon^{0.17}$.

3.3.2 Numerical Results

As we mentioned earlier, we do not expect to necessarily reproduce the scalings found in experiment, and it is likely that we will not be able to confirm the theoretical scalings because of finite size effects. Indeed, this is the case as we show in Fig. (3.8). Here we

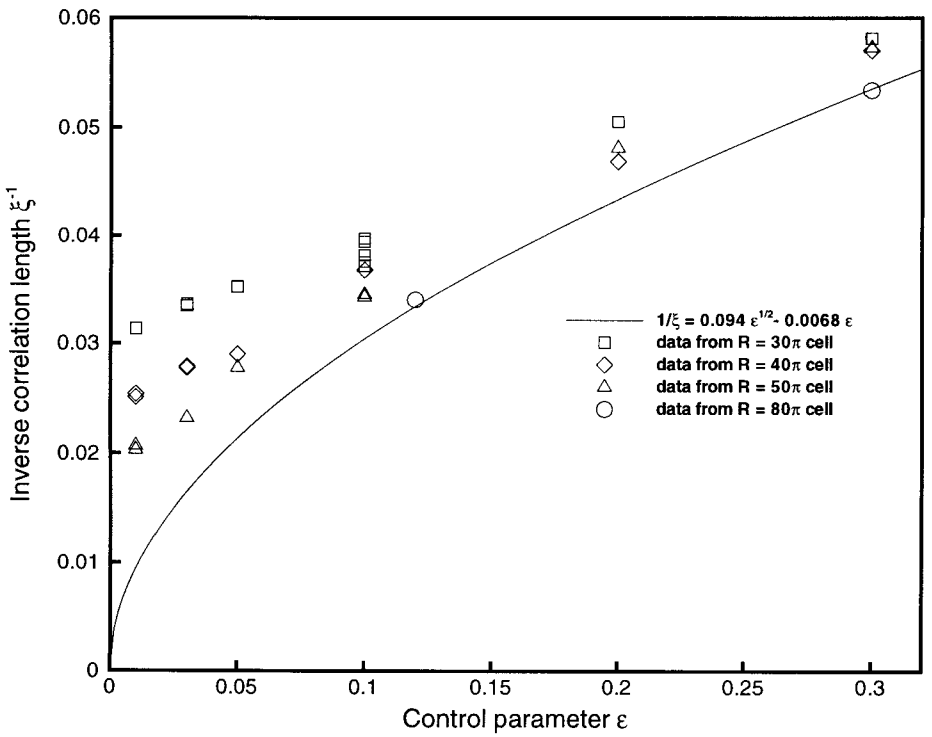

Figure 3.8: Dependence of the correlation length ξ on the control parameter ϵ for $g_3 = 1.5$ and the expected $\sqrt{\epsilon}$ fit for small ϵ.

see that the correlation length does not follow a $\epsilon^{-1/2}$ relationship as $\epsilon \to 0$. In fact, it appears that a linear fit is actually better to the data. There is a general trend, however, for the data to follow the theoretical $\epsilon^{-1/2}$ scaling for smaller ϵ in the larger cells, i.e., the deviation from the theoretical scaling occurs for smaller ϵ in the larger cells. Therefore, it

is clear that finite size plays a role in determining ξ. This is not too surprising perhaps, since ξ must be constrained to be no larger than the size of the cell, otherwise it is questionable as to what ξ is measuring. Although our computed correlation lengths are still considerably smaller than the size of the cell, this does not exclude the possibility that the finite boundaries are influencing their values. The correlation length data is also given in Table 3.1.

A somewhat contrary observation is made in [31] where they try to show that finite size effects have not influenced the measurement of their correlation lengths. They do this by comparing the correlation lengths of patterns obtained without rotation and for small values of the control parameter ϵ. In this case, the pattern consists of essentially one set of nearly straight rolls, and a measured correlation length of such a pattern should provide, in essence, the upper bound to the correlation. Since they show this to be considerably larger than the lengths measured with rotation, they conclude that finite size effects in the analysis algorithm are not important. We currently do not have an explanation for this observation.

Since we anticipate that finite size effects are influencing the correlation lengths we observe, we consider scaling them with the size of the cell. Thus we assume that our correlation lengths computed using Eq. (3.6), and which we now label as ξ_{FS}, are related to the theoretical value ξ by

$$\xi_{\mathrm{FS}} = \xi F(\xi/R) \tag{3.12}$$

where R is the radius of the cell and F is some function. Then, if the theoretical scaling $\xi \propto \epsilon^{-1/2}$ holds, a plot of $\epsilon^{-1/2}/\xi_{\mathrm{FS}}$ versus $\epsilon^{-1/2}/R$ should collapse all the data for different values of R and ϵ onto a single curve. We show in Fig. (3.9) a plot of our data on these scales. The successful collapse of the data onto a single curve indicates that the theoretical scaling of domain size with ϵ does indeed hold for our model equation. It also shows the importance of scaling the correlation length appropriately to take account of *finite size* effects. Note that if finite size effects were unimportant, a straight horizontal line is the expected fit for the data since this would imply that $\xi_{\mathrm{FS}} \propto \xi$, and so from Eq. (3.12), $F(\xi/R) =$ constant. We can see that for small values of the argument $\epsilon^{-1/2}/R$, our data does indeed follow this expected fit reasonably well. This is not surprising since

Control parameter ϵ	Cell radius R	Correlation length xi
0.01	30π	31.92
	40π	39.84
		39.38
	50π	48.32
		49.21
0.03	30π	29.77
		29.92
	40π	35.83
		36.00
	50π	43.09
0.05	30π	28.40
		28.42
	40π	34.46
	50π	35.97
0.1	30π	25.17
		25.34
		26.19
		26.65
		26.94
	40π	27.20
	50π	28.99
		29.20
0.12	80π	29.41
0.2	30π	19.79
	40π	21.33
	50π	20.77
0.3	30π	17.20
	40π	17.53
	50π	17.45
		17.46
	80π	18.73

Table 3.1: Measured correlation lengths for different ϵ and different cell sizes. The inverse values are plotted as a function of ϵ in Fig. (3.8). Multiple correlation lengths at the same value of ϵ and R indicate values that have been obtained from different sections of a run, or from runs started with different initial conditions.

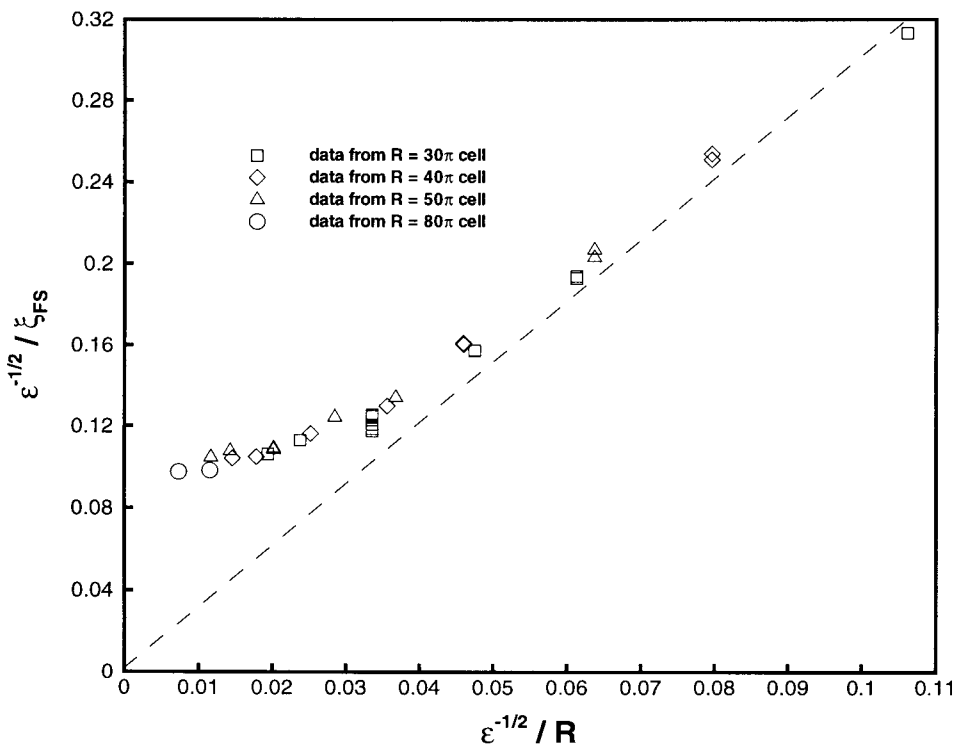

Figure 3.9: Collapse of the correlation length ξ versus ϵ data on a line by rescaling ξ and ϵ to take account of finite size effects. The dashed line represents the asymptotic limit of the finite size correlation length ξ_{FS}.

we would expect finite size effects to be less prevalent in those cases where the domain size was small compared with the cell size. This occurs when both R and ϵ are large, or when $\epsilon^{-1/2}/R$ is small. Thus, this provides further evidence that our data are consistent with the theoretical scaling.

For larger values of $\epsilon^{-1/2}/R > 0.03$, significant deviation from the theoretical fit occurs. This is clearly due to finite size effects since large values of $\epsilon^{-1/2}/R$ corresponds to small cells and small values of ϵ, where we tend to find domains of rolls that are large compared to the cell size. Thus, it is not surprising that the size of the cell may be influencing the size of the domains. It is important to note that the deviation from the theoretical scaling approximately follows a straight line. This indicates that $\epsilon^{-1/2}/\xi_{FS} \sim \epsilon^{-1/2}/R$ and hence that $\xi_{FS} \sim R$ as $\epsilon^{-1/2}/R \to \infty$. In other words, we find that the correlation length scales like the size of the cell as the cell size and/or ϵ decreases. The asymptotic limit is shown as the dashed line in Fig. (3.9).

In recent experimental work, a similar collapse of the data onto a single curve has been attempted [33]. In these experiments, the cell size is fixed while the control parameter $\epsilon = R/R_c - 1$ and rotation rate Ω are varied to give the different domain structures. A successful collapse of the data is then achieved by scaling the data sets with Ω. In the finite cell, sidewall effects are known to influence the dynamics, and some differences as Ω is varied have also been noted [33]. Thus the scaling with Ω is somewhat less satisfactory than scaling with the cell size since it becomes difficult to isolate exactly those effects due to finite size, and those due to rotation. In any case, the experimental results appear to be consistent with our findings. They find that in plotting $(1/\xi)^2/\epsilon$ as a function of ϵ, the data does not approach a constant value as ϵ vanishes, as one expects if the theoretical scaling $\xi \propto \epsilon^{-1/2}$ holds. The divergence of the values of $(1/\xi)^2/\epsilon$ as $\epsilon \to 0$ is clearly due to the fact that $(1/\xi)^2$ is non-vanishing as ϵ decreases. In other words, the correlation length ξ remains finite as $\epsilon \to 0$. Our results clearly provide evidence to support this conclusion, at least in the case of the Swift-Hohenberg models.

For the domain switching frequency, we find good agreement with the theoretical scaling, so long as ϵ is not too large. In Fig. (3.10), we have plotted ω_a against ϵ on linear scales, and we see that a linear fit to the data is good for $\epsilon < 0.2$. Beyond values of 0.2, we see that the data no longer follow a linear relationship, but this deviation

can be attributed to higher order corrections as ϵ increases. The fact that the time

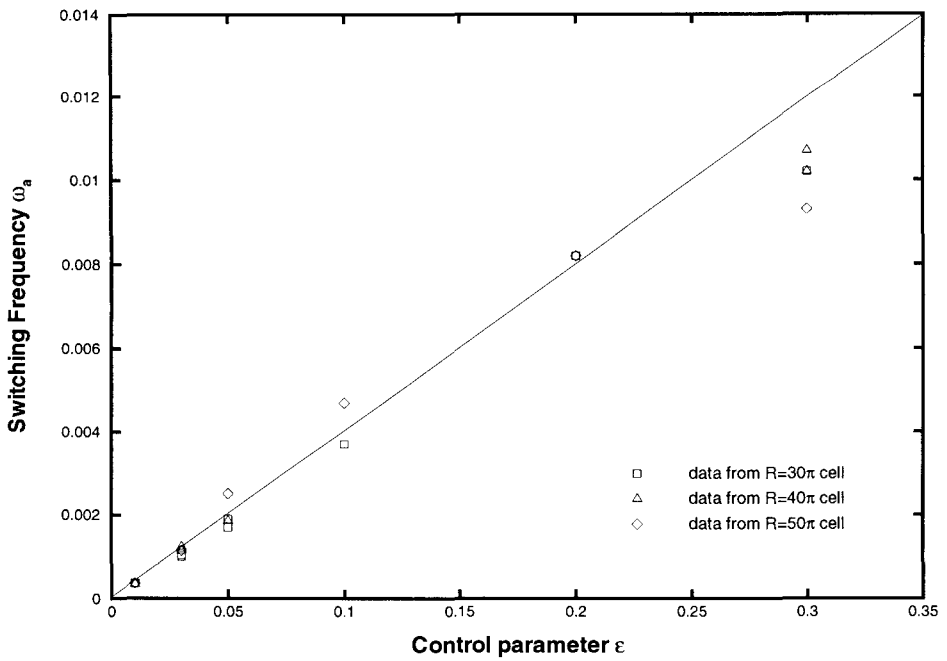

Figure 3.10: Domain switching frequency as function of ϵ on linear scales. The line is $\omega_a = 0.04\epsilon$.

scales follow the theoretical predictions in the finite case is not totally surprising, even in light of the disagreement found in the length scales above. Since our model equation does not allow for any complicated dynamics at the outer boundary, it is likely that the presence of such boundaries will not affect the temporal behavior of the solution. In fact, since many of the rolls are actually nucleated from the boundary, we might expect the presence of boundaries to enhance rather than inhibit any domain switching behavior of our solutions.

In the case of experiments, the switching frequency data are found to be inconsistent with the theoretical prediction, $\omega_a \propto \epsilon$ [31, 33]. As with the correlation length, the data could be successfully collapsed onto a single curve after scaling by the rotation

rate [33]. A plot of $\tilde{\omega}_a/\epsilon$ against ϵ, where $\tilde{\omega}_a$ is the scaled switching frequency, shows that $\tilde{\omega}_a/\epsilon$ does tend to a constant value as ϵ approaches zero, in agreement with the theoretical prediction. But the curve quickly deviates from the theoretical scaling and the less satisfactory scaling given in Eq. (3.11) is necessary to fit the data.

To summarize then, we have found that the theoretical scalings of the correlation length and switching frequency with ϵ do hold in the case of our model equations. It is necessary, however, to make allowances for finite size effects in the case of the correlation length. We have found that if the measured correlation lengths are scaled linearly with the cell radius, then agreement with the theoretical predictions is obtained. For a cell of radius R, we have found that the correlation length $\xi \sim R/3$, for R large and/or ϵ small. Our results appear to be consistent with the experimental results in [33], while also providing strong evidence to support the conjecture that the different scalings obtained in experiment are due in large part to finite size effects. One further effect that we have not considered here, but which may help to shed more light on the discrepancy in the theoretical and experimental scalings, is to investigate the effects of more complicated boundary conditions. In particular, the boundary conditions suggested by Kuo [34] might help in explaining the significant difference observed between the scaling of ω_a in our numerical simulations and in the experiments.

Chapter 4
Numerical Simulation of Spiral Defect Chaos

The existence of a spiral defect chaos state in Rayleigh-Bénard convection was first observed experimentally by Morris *et al.* [40]. Since then, other researchers have been able to confirm the existence of this state both experimentally [2, 29, 30] and numerically through integrations of Swift-Hohenberg type models [3, 16, 43, 44, 49, 50]. The appearance of the spiral state in the convection system was surprising since it was not predicted theoretically [10, 13]. This has clearly helped to spur a great deal of interest in this system.

In this chapter we numerically study the spiral chaos state observed in the solutions of a generalized Swift-Hohenberg equation. In Section 4.1, we state the model. Then, in the next section, we describe the numerical solution, based on our earlier experience with solving other Swift-Hohenberg models. In the third section, we describe the qualitative features of the solutions and give a detailed account of the effect of a global rotation on the spiral state, which is our primary objective in studying this system.

4.1 The Model – Generalized Swift-Hohenberg Equation

We follow the work of Xi *et al.* [50] who numerically studied a generalized Swift-Hohenberg model for spiral defect chaos. The model involves the addition of mean flow effects to the usual Swift-Hohenberg equation by coupling the field equation for $\psi(x, y, t)$ to a vertical vorticity potential $\zeta(x, y, t)$. The equations we therefore consider

are

$$\frac{\partial \psi}{\partial t} + g_m \mathbf{U} \cdot \nabla \psi = \epsilon \psi - (\nabla^2 + 1)^2 \psi + N(\psi, t), \tag{4.1}$$

$$\left[\frac{\partial}{\partial t} - Pr(\nabla^2 - c^2)\right] \nabla^2 \zeta = \left[\nabla(\nabla^2 \psi) \times \nabla \psi\right] \cdot \hat{z}, \tag{4.2}$$

where $\mathbf{U}$ is the mean flow velocity given by

$$\mathbf{U} = \nabla \times (\zeta \hat{\mathbf{z}}) = (\partial_y \zeta)\hat{x} - (\partial_x \zeta)\hat{y}. \tag{4.3}$$

Here, Pr represents the Prandtl number and c^2 is a parameter related to damping of the horizontal flow by viscous coupling to the top and bottom plates. As in the work of Xi *et al.*, we will use $c^2 = 2$ to model physical rigid-rigid boundary conditions, rather than free-slip conditions modeled by $c^2 = 0$. The appropriate lateral boundary conditions are

$$\psi|_B = \hat{\mathbf{n}} \cdot \nabla \psi|_B = \zeta|_B = \hat{\mathbf{n}} \cdot \nabla \zeta|_B = 0, \tag{4.4}$$

where $\hat{\mathbf{n}}$ is the unit normal to the boundary of the domain of integration, B. Note that the boundary conditions for the field ψ are unchanged with the addition of the vorticity. The boundary conditions on ζ ensure that both the normal and tangential components of the mean flow velocity vanish at the boundary.

We have considered two different nonlinear terms for $N(\psi)$. The first is the same as used by Xi *et al.*,

$$N(\psi) = -g_2 \psi^2 - \psi^3, \tag{4.5}$$

while the second is the combination of terms used to model the KL instability, Eq. (2.3). Thus, we hope to see the effect of adding rotation to the spiral chaos state.

4.2 Numerical Solution

The obvious similarity between the generalized Swift-Hohenberg equation and our model equation for the KL instability Eq. (2.1) and Eq. (2.3) suggests that we also try our fully implicit solution approach on this system of equations.

We begin by discretizing Eqs. (4.1) and (4.2) in time using the Crank-Nicolson scheme;

$$\begin{aligned}\frac{\psi^{n+1}-\psi^n}{\Delta t} &+ \frac{1}{2}g_m\left[\mathbf{U}^{n+1}\cdot\nabla\psi^{n+1}+\mathbf{U}^n\cdot\nabla\psi^n\right]\\ &= \frac{1}{2}\left[\left(\epsilon-(\nabla^2+1)^2\right)\psi^{n+1}+\left(\epsilon-(\nabla^2+1)^2\right)\psi^n\right]\\ &+ \frac{1}{2}\left[N(\psi^{n+1})+N(\psi^n)\right], \qquad (4.6)\end{aligned}$$

$$\begin{aligned}\frac{\nabla^2\zeta^{n+1}-\nabla^2\zeta^n}{\Delta t} &- \frac{1}{2}Pr\left[(\nabla^2-c^2)\nabla^2\zeta^{n+1}+(\nabla^2-c^2)\nabla^2\zeta^n\right]\\ &= \frac{1}{2}\left[\nabla(\nabla^2\psi^{n+1})\times\nabla\psi^{n+1}+\nabla(\nabla^2\psi^n)\times\nabla\psi^n\right]\cdot\hat{z}. \qquad (4.7)\end{aligned}$$

We rewrite these by collecting the terms at the new time step $n+1$;

$$\left[(\nabla^2+1)^2-\epsilon+\frac{2}{\Delta t}\right]\psi^{n+1}+g_m\mathbf{U}^{n+1}\cdot\nabla\psi^{n+1}-N(\psi^{n+1}) = R_1^n, \qquad (4.8)$$

$$\left[\nabla^4-\left(c^2+\frac{2}{Pr\Delta t}\right)\nabla^2\right]\zeta^{n+1}+\frac{1}{Pr}\left[\nabla(\nabla^2\psi^{n+1})\times\nabla\psi^{n+1}\right]\cdot\hat{z} = R_2^n, \qquad (4.9)$$

where R_1^n and R_2^n contain all terms at the current time step n,

$$R_1^n \equiv \left[\epsilon+\frac{2}{\Delta t}-(\nabla^2+1)^2\right]\psi^n-g_m\mathbf{U}^n\cdot\nabla\psi^n+N(\psi^n), \qquad (4.10)$$

$$R_2^n \equiv -\left[\nabla^4-\left(c^2-\frac{2}{Pr\Delta t}\right)\nabla^2\right]\zeta^n-\frac{1}{Pr}\left[\nabla(\nabla^2\psi^n)\times\nabla\psi^n\right]\cdot\hat{z}. \qquad (4.11)$$

Let us define the operators,

$$L_1 \equiv \nabla^4+2\nabla^2+\left(1-\epsilon+\frac{2}{\Delta t}\right), \qquad (4.12)$$

$$L_2 \equiv \nabla^4-\left(c^2+\frac{2}{Pr\Delta t}\right)\nabla^2, \qquad (4.13)$$

and the nonlinear terms,

$$N_1(\psi,\zeta) \equiv g_m\mathbf{U}\cdot\nabla\psi-N(\psi), \qquad (4.14)$$

$$N_2(\psi,\zeta) \equiv \frac{1}{Pr}\left[\nabla(\nabla^2\psi)\times\nabla\psi\right]. \qquad (4.15)$$

Then the nonlinear equations to solve at each time step $n = 0, 1, 2, \ldots$ are

$$L_1\psi^{n+1} + N_1(\psi^{n+1}, \zeta^{n+1}) = R_1^n, \tag{4.16}$$

$$L_2\zeta^{n+1} + N_2(\psi^{n+1}, \zeta^{n+1}) = R_2^n, \tag{4.17}$$

which can also be written conveniently as the matrix system,

$$\begin{pmatrix} L_1 & 0 \\ 0 & L_2 \end{pmatrix} \begin{pmatrix} \psi^{n+1} \\ \zeta^{n+1} \end{pmatrix} + \begin{pmatrix} N_1(\psi^{n+1}, \zeta^{n+1}) - R_1^n \\ N_2(\psi^{n+1}, \zeta^{n+1}) - R_2^n \end{pmatrix} = \begin{pmatrix} 0 \\ 0 \end{pmatrix}. \tag{4.18}$$

This is a large nonlinear system of equations which can be solved by Newton's method. As before, the efficient solution of the resultant linear problem depends upon the spatial discretization we choose. Since we are again interested in solving these equations in a circular geometry, we use a finite difference discretization of the polar form of the equations. Then, as before, preconditioned GMRES offers a particularly efficient approach to solving the linear problem.

As we noted before, it is actually more efficient to precondition the system Eq. (4.18) before applying Newton's method, rather than applying preconditioned GMRES at every inner iteration. Therefore, we actually apply Newton's method to

$$F\begin{pmatrix} \psi \\ \zeta \end{pmatrix} \equiv \begin{pmatrix} \psi \\ \zeta \end{pmatrix} + \begin{pmatrix} L_1^{-1}\left(N_1(\psi, \zeta) - R_1\right) \\ L_2^{-1}\left(N_2(\psi, \zeta) - R_2\right) \end{pmatrix} = \begin{pmatrix} 0 \\ 0 \end{pmatrix}. \tag{4.19}$$

We have dropped the superscripts for convenience, and L_1^{-1} and L_2^{-1} are the inverses of the biharmonic operators L_1 and L_2 given in Eq. (4.12) and Eq. (4.13) respectively. Notice also that the terms R_1^n and R_2^n can be obtained recursively for $n \geq 1$;

$$R_1^n = \frac{4}{\Delta t}\psi^n - R_1^{n-1}, \tag{4.20}$$

$$R_2^n = -\frac{4}{Pr\Delta t}\nabla^2\zeta^n - R_2^{n-1}. \tag{4.21}$$

The values of R_1^0 and R_2^0 can be obtained from Eq. (4.10) and Eq. (4.11).

We have also implemented the same adaptive time stepping scheme considered in Section 2.7. We find, again, a general trend for the time step to be increased, but the

size of Δt in this case is considerably smaller (usually $O(1)$). Larger time steps are usually possible when the rotation nonlinear terms, Eq. (2.3), are included. We suspect the need for a smaller time step is due to the presence of fast dynamical structures observed in the spiral chaos state by Cross [16], as well as the use of larger values of ϵ.

4.3 Qualitative Results

Our primary goal is to study the effects of rotation on the spiral chaos state previously obtained by Xi *et al.* [50] and also by Cross [16]. We begin by reproducing the spiral state found by Xi and his coauthors, by choosing the same form for the nonlinearity $N(\psi)$. We use the same parameters, namely a cell of radius 32π and set $\epsilon = 0.7$, $g_m = 50$, $g_2 = 0.35$ and $Pr = 1$. These are chosen to approximately reproduce the parameters found in the experiments of Bodenschatz *et al.* [8]. As we noted before, $c^2 = 2$ to model the physical rigid-rigid boundary conditions at the top and bottom plates.

In Fig. (4.1) we show the evolution of a run started random initial conditions. We also show the corresponding vorticity potential at this time. We first note the similarity of our result with the result of Xi *et al.* who integrated the equations using a significantly different numerical scheme. At $t = 500$ in the evolution, we see approximately six well developed spirals in the cell of either clockwise or counterclockwise orientations. The location of the spirals is also clearly seen in the plot of the vorticity potential $\zeta(x, y, t)$ where they appear as a bright or dark spot, depending on their sense. An interesting question to consider is whether rotation of the entire cell will favor one spiral orientation over another. From a physical standpoint, the answer to this question is that rotation should affect the behavior since it provides a symmetry-breaking mechanism in the system. This has been observed experimentally [19] and somewhat confirmed in the numerical work of Ponty *et al.* [43]. It should be noted that this is a difficult question to answer definitively since this would require a large number of runs so that significant statistical data could be collected. Therefore, we will concentrate more on providing qualitative evidence to justify our claims about the effect of rotation.

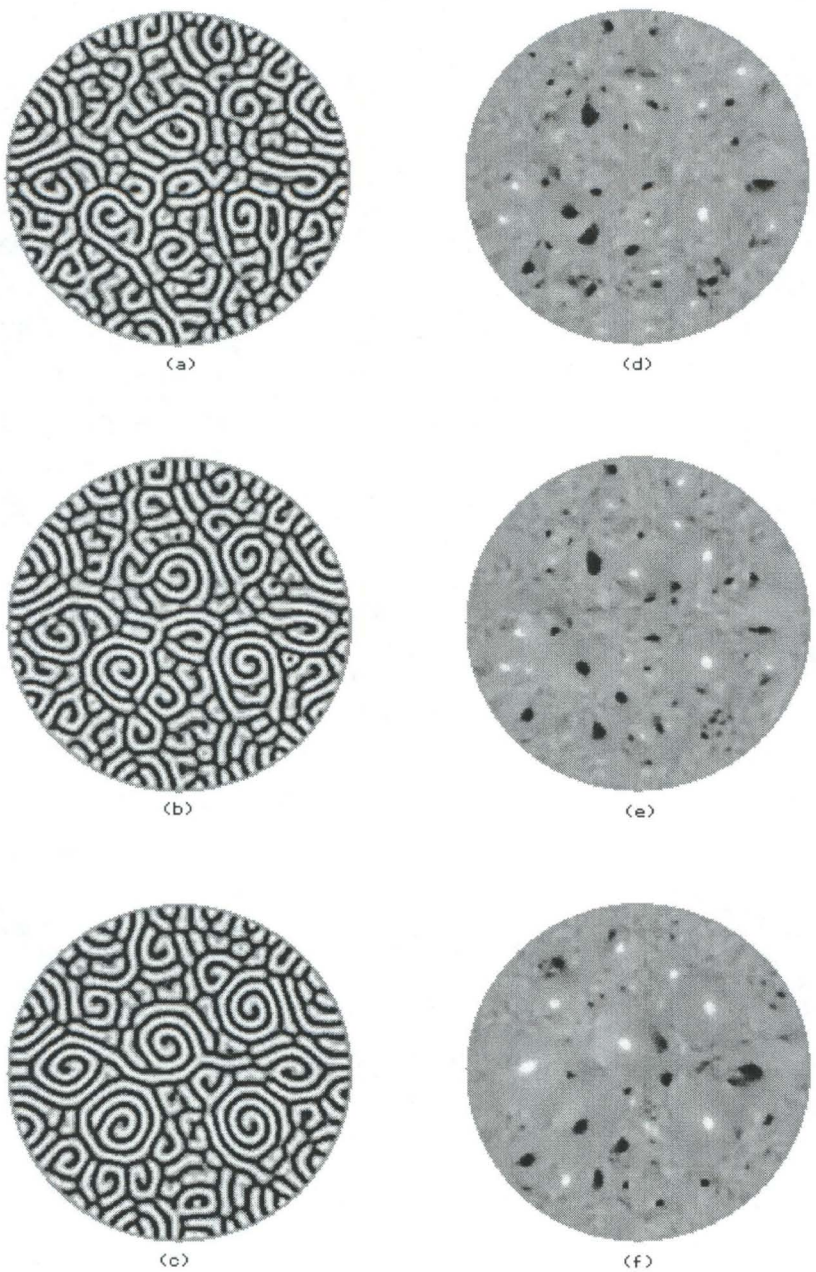

Figure 4.1: Evolution of the spiral chaos pattern from random initial conditions. The field ψ is shown at (a) $t = 120$, (b) $t = 250$ and (c) $t = 500$. Dark (white) regions correspond to positive (negative) values of ψ. The corresponding vorticity potential ζ is shown in (d), (e) and (f), where dark and white regions correspond to clockwise and counterclockwise rotations respectively. The other parameters are $\epsilon = 0.7$, $g_2 = 0.35$, $g_m = 50$, $Pr = 1$, $c^2 = 2$ and the cell radius is 32π.

4.3.1 Comparisons Without Rotation

We first note some qualitative trends in the absence of rotation. Thus, we will be considering solutions to Eq. (4.1) and Eq. (4.2) where the nonlinear term is given by Eq. (4.5) as in [50]. We have repeated some of the experiments of Xi *et al.* to ensure consistency in our results, but also to confirm various trends with the parameters for ourselves. We shall also briefly summarize some of the other trends they have found, as well as the findings of Cross [16], who considered a slightly different form of the nonlinearity.

We first look at the effect of smaller cell size. In a cell of radius 16π we do not find a truly chaotic spiral state. Instead, the domain is dominated by a single slowly rotating spiral. This can be seen in Fig. (4.2) where we present an evolution from random initial conditions. We see that at around $t = 600$, a single well defined spiral has formed near the center of the cell. The other structures in the domain at this time are generally disordered, although some may be seen as the beginnings of other spirals. However, as time progresses, we see that no further spirals actually form, and the lone spiral near the center begins to dominate the entire cell. From our runs in larger cells at the same parameter values, we have observed spirals of the same approximate size as the spiral seen in this cell at $t = 2000$. Thus, it appears that the size of the spirals are determined almost exclusively by the parameter values and not the size of the domain. We obtain only one spiral here because the cell is not large enough to accommodate another spiral.

We also notice the slow rotation of this spiral which seems to occur at about one revolution every 600 time units. But the important feature we observe here is a more globally ordered state with a single spiral, rather than a truly chaotic spiral state. Thus, we confirm the findings of Xi and his coauthors in that a cell of large aspect ratio is critical to the existence of spiral chaos.

The inclusion of mean flow is essential to the formation of the spiral chaos state. This is easily confirmed by setting the coupling constant $g_m = 0$. Then Eqs. (4.1) and (4.2) completely decouple, and if we also set $g_2 = 0$, the equation for the field variable ψ reduces to the original Swift-Hohenberg equation, where no spiral chaos state has been observed. One may then think that the non-Boussinesq coupling constant g_2 plays an important role in the formation of spiral chaos, but it has been shown by Bestehorn *et*

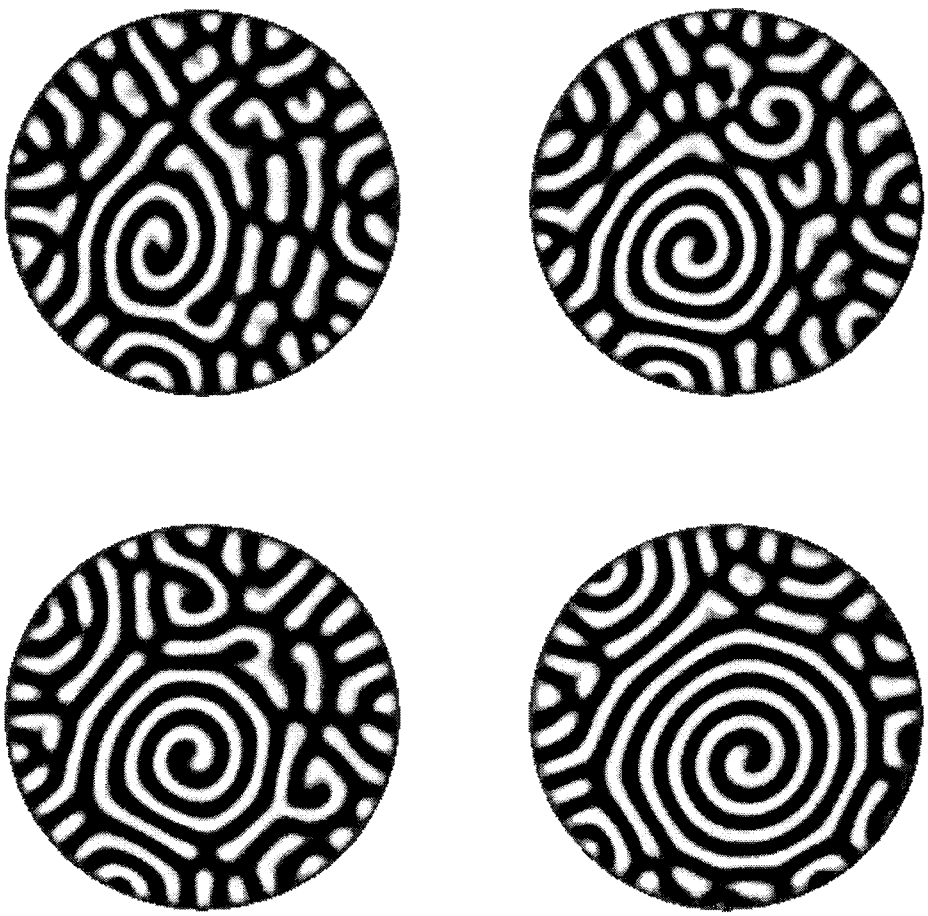

Figure 4.2: Evolution of the field ψ from random initial conditions in a cell of radius 16π. From left to right, top to bottom, the times are $t = 600, 900, 1200, 2000$. The other parameters are as in Fig. (4.1).

al. [3] and also by Cross [16] that this is not necessary. In fact, in [16], $g_2 = 0$ for all the results presented. There has also been an extensive study of the trends with varying g_m in that work, which has shown the spiral state to exist for a wide range of values, $10 < g_m < 50$. Although we have not studied these trends in this case of no rotation, we have seen the spiral state occur for a similar range of values for g_m even when rotation is included (see results in the following section).

We finally note the importance of the Prandtl number Pr. Xi *et al.* has shown that it is necessary for Pr to be reasonably small. For $Pr = 6$, they did not observe a spiral chaos state. This is not too surprising since in the experimental situation, mean flow effects are expected to be strongest at smaller Prandtl numbers, and we have already noted the importance of mean flow in the formation of spiral chaos. It is also interesting to note that ϵ must be reasonably large in order to observe spiral chaos. This is clearly seen in the experimental work of Morris *et al.* [40] who show the transition to the spiral state as ϵ is increased.

4.3.2 Effect of Rotation

We now consider the effect of rotation on the spiral chaos state. This is modeled by changing the nonlinear term in Eq. (4.1) to include the effects of rotation. In our implementation, we have replaced the nonlinear terms Eq. (4.5) with those used to model the KL instability in domain chaos, Eq. (2.3). Thus we have a mechanism with which to study the transition from a domain chaos to spiral chaos state (or vice versa).

Our initial observation is that rotation and mean flow are somewhat competing processes. While mean flow has the effect of "winding up" the roll structures (into spirals), rotation seems to want to "straighten them out." This effect can be seen in Fig. (4.3). Here we compare the solutions with and without the rotation terms included, at a sequence of times. The initial condition for both is the reasonably well defined spiral state seen in Fig. (4.1)(c). In the absence of rotation, we see most of the original spirals continue to wind up increasing in size. By $t = 1500$, the cell is dominated by many large spirals with either sense of rotation. The structures outside the spirals are noticeably smaller and more disordered. On the other hand, with the rotation "switched on," we see that many of the original spirals have been unwound, or the spiral core has broken down.

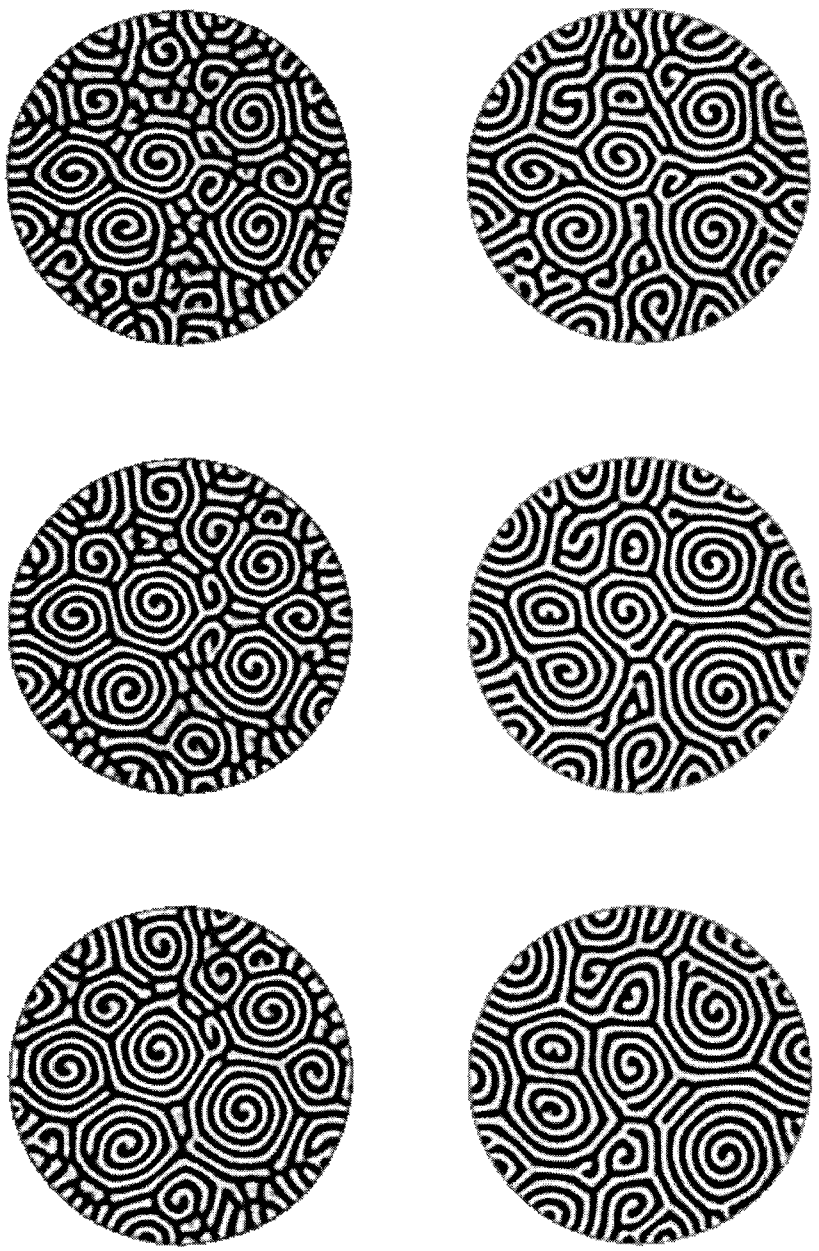

Figure 4.3: Comparison of solutions with and without the rotation terms included. The solutions **without** rotation are shown on the left. Both sets of solutions are shown at *400 time* units apart, starting at a time $t = 200$ from the pattern given in Fig. (4.1) (c). The parameters for the run without rotation are unchanged from that run. For the solutions with rotation, $g_3 = 1.5$, while all other parameters are the same as with the run without rotation.

By $t = 1500$, the cell looks to have no more than three large, well defined spirals, all with the same sense of rotation. Outside of these spirals, other large ordered structures are observed like the sidewall foci at the nine and ten o'clock positions.

4.3.3 Linear Stability Analysis

We are interested in gaining a better understanding of the competition that exists between the mean flow and rotational effects. In particular, we want to determine the effect of mean flow on the onset of the KL instability. We consider the linear stability of straight roll solutions of the form

$$\psi_0(x) = A\cos(qx), \qquad \zeta_0 = 0, \tag{4.22}$$

where $A \sim \epsilon^{1/2}$, to small perturbations $\delta\psi(\mathbf{x},t)$ and $\delta\zeta(\mathbf{x},t)$ in the model equations Eq. (4.1) - Eq. (4.2). Thus, substituting

$$\psi(\mathbf{x},t) = \psi_0(x) + \delta\psi(\mathbf{x},t) \tag{4.23}$$

$$\zeta(\mathbf{x},t) = \zeta_0 + \delta\zeta(\mathbf{x},t) \tag{4.24}$$

into Eqs. (4.1) - (4.2) and linearizing, we have

$$\begin{aligned}\frac{\partial(\delta\psi)}{\partial t} + g_m(\psi_0)_x(\delta\zeta)_y &= \epsilon\delta\psi - (\nabla^2+1)^2\delta\psi - 3g_1\psi_0^2\delta\psi \\ &+ g_2\hat{z}\cdot\left(\nabla\times\left[|\nabla\psi_0|^2\nabla\delta\psi\right] + \nabla\times\left[2(\nabla\psi_0\cdot\nabla\delta\psi)\nabla\psi_0\right]\right) \\ &+ g_3\left(\nabla\cdot\left[|\nabla\psi_0|^2\nabla\delta\psi\right] + \nabla\cdot\left[2(\nabla\psi_0\cdot\nabla\delta\psi)\nabla\psi_0\right]\right),\end{aligned} \tag{4.25}$$

and

$$\left[\frac{\partial}{\partial t} - Pr(\nabla^2 - c^2)\right]\nabla^2\delta\zeta = \left[\nabla(\nabla^2\psi_0)\times\nabla\delta\psi + \nabla(\nabla^2\delta\psi)\times\delta\psi_0\right]\cdot\hat{z}. \tag{4.26}$$

We assume that

$$\delta\psi(\mathbf{x},t) = e^{\sigma t}e^{i\mathbf{k}\cdot\mathbf{x}}\sum_n B_n\cos(2nqx), \tag{4.27}$$

$$\delta\zeta(\mathbf{x},t) = e^{\sigma t}e^{i\mathbf{k}\cdot\mathbf{x}}\sum_n C_n\sin[(2n+1)qx]. \tag{4.28}$$

ϵ	g_3	$\langle k \rangle$
0.4	1.5	0.9
0.55	4.5	0.77
	6.0	0.76
	9.0	0.78
0.7	4.5	0.73
	9.0	0.71
	15.0	0.72

Table 4.1: Mean wave numbers $\langle k \rangle$ at $g_m = 50$. The values show a clear trend to smaller values as ϵ increases. The critical wave number for our model equation is scaled to be 1.

Truncating after the first term in each of these sums we find that the growth rate σ satisfies

$$\sigma - \frac{1}{2}g_m D - \epsilon + (1 - |\mathbf{k}|^2)^2 + \frac{3}{2}g_1 A^2 - g_2 A^2 q^2 k_x k_y + \frac{1}{2}g_3 A^2 q^2 (3k_x^2 + k_y^2) = 0 \quad (4.29)$$

where

$$D = \frac{A^2 q^2 k_y^2 (q^2 - |\mathbf{k}|^2)}{\sigma(q^2 + |\mathbf{k}|^2) + Pr\left[(q^2 + |\mathbf{k}|^2)^2 + 4k_x^2 q^2 + c^2(q^2 + |\mathbf{k}|^2)\right]}. \quad (4.30)$$

Thus we see that the mean flow is important when $q^2 - |\mathbf{k}|^2 \neq 0$, i.e., when there is difference in the wavenumbers of the base state ψ_0 and the perturbation $\delta\psi$.

4.3.4 Parameter Space

From the linear stability analysis, it is clear that mean flow can affect the onset of the KL instability if there is a change in the wave number of the pattern. It is therefore useful to calculate the wave number of patterns obtained with mean flow. Note that in the absence of mean flow, our equations have been scaled to give a critical wave number $k_C = 1$. We present in Table 4.1 representative mean wave numbers computed (using Eq. (3.4)) for patterns obtained at various values of ϵ and rotation rates g_3 for a fixed mean flow, $g_m = 50$. We clearly see that mean flow has the effect of reducing the wave number of the pattern. For fixed ϵ, there is a slight variation in these values as the rotation rate g_3 is increased, but these variations are small compared to the overall shift in the wave number. We also find that once g_m becomes reasonably large, $g_m > 10$,

there is also little variation in the wave numbers as g_m increases. A more significant variation in these wave number shifts is seen as ϵ increases, with a clear trend towards smaller values of $\langle k \rangle$ for larger ϵ. This is expected since we anticipate stronger nonlinear effects as the system is driven further from onset.

Although mean flow is an important component in the formation of spirals, we have found little variation in our solutions for $10 < g_m < 50$. An example of this is seen in Fig. (4.4). The patterns at $g_m = 10$ do show some intrinsic differences from those at the higher values of g_m, particularly at later times. However, the solutions at $g_m = 25$ and $g_m = 50$ appear to be very similar to each A similar result has been found by Cross [16]. We therefore consider the behavior of the solutions as we vary ϵ and the rotation rate g_3 for a fixed value of g_m. Since we wish to include significant mean flow effects in our solutions, we choose a large value, $g_m = 50$.

We now consider the effect of rotation at fixed values of ϵ and mean flow. In the absence of rotation ($g_3 = 0$), we find that a spiral state state develops for $\epsilon > 0.4$. As we increase g_3, we see that the rotation begins to unwind the spirals. For ϵ close to 0.4, the spiral state is completely eliminated for g_3 as small as 0.5. For larger ϵ, the spiral state appears to more stable and persists for much larger rotation rates. For example, for $\epsilon = 0.7$, $g_3 \approx 7$ before all the spirals are eliminated from the solutions. Once the rotation rate is high enough to remove all the spirals from the solution, we observe instead a static roll-like pattern. For smaller $\epsilon < 0.55$, the rolls are straight and most of the cell is filled with just a single set of these parallel rolls. For larger ϵ, though, the rolls appear more curved and it is rare that a single set of rolls will fill the cell. If we further increase g_3, the roll structures become dynamic and domain chaos is observed. For very large values of the rotation rate, the domains become smaller and smaller and the patterns generally more disordered. However, it is still possible to observe a switching of orientation of the roll-like structures in the pattern, and we therefore still classify this state as domain chaos.

It is clear that the higher rotations rates needed to bring on the onset of the KL instability and the formation of domains is consistent with our understanding of the mean flow effects. As we noted earlier, mean flow acts to decrease the wave number of the pattern and the decrease is greater for larger values of ϵ. Thus we would expect to

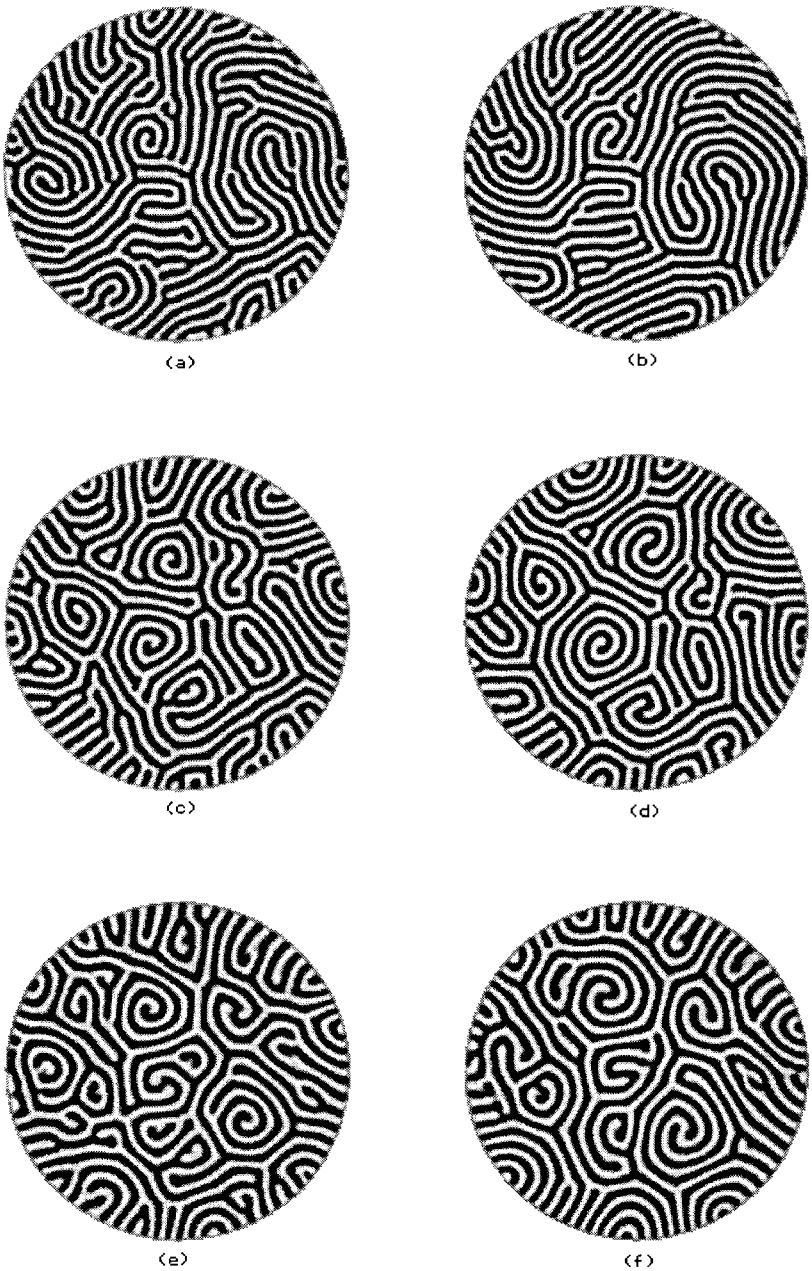

Figure 4.4: Comparison of solutions with varying mean flow g_m. For (a) and (b) $g_m = 10$, for (c) and (d) $g_m = 25$ and for (e) and (f) $g_m = 50$. The patterns in (a), (c) and (e) are shown at $t = 550$ and in (b), (d) and (f), the time is $t = 1550$. All solutions are been evolved from the same random initial conditions. The other parameters are $\epsilon = 0.7$ and $g_3 = 1.5$ for all patterns shown.

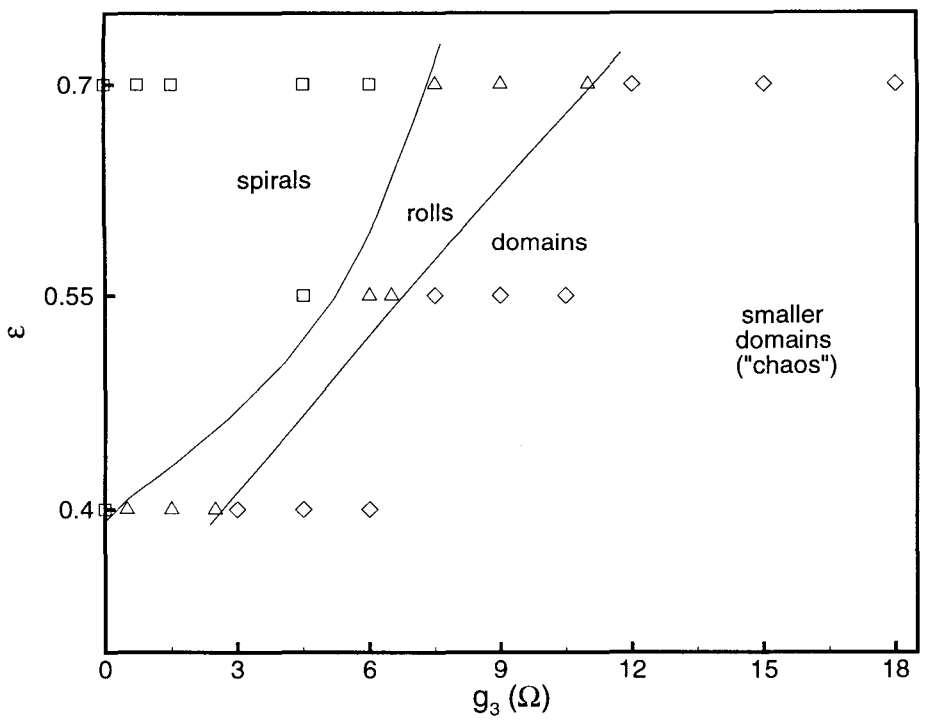

Figure 4.5: Summary of patterns found in parameter space at fixed $g_m = 50$. A square represents that a spiral state is found, a triangle represents that a roll state is found, and a diamond represents that a domain chaos state is found. The lines show the approximate location of the boundaries between these transitions.

see the domain state come in at higher values of g_3 as we increase ϵ. This is precisely what we have observed in our results.

We summarize our results in Fig. (4.5) which shows a slice of parameter space at a fixed mean flow, $g_m = 50$. Since spiral states are generally not found for $\epsilon < 0.35$, we have focused our attention on the range $0.4 < \epsilon < 0.7$. For $\epsilon > 0.7$ spirals are still observed in the absence of rotation, but roll states seem to be more difficult to observe this far above threshold. With rotation, we find that the roll-like structures occupy only small regions of the domain, and the rolls are less well defined, particularly for $\epsilon > 0.55$. This is to be expected since the solutions become more disordered at larger ϵ and higher rotation rates. From their visual appearance and dynamic behavior, we are able to determine approximate boundaries in parameter space between the various states found

in this system. These are also shown in Fig. (4.5).

We observe that the roll patterns seen at moderate rotation rates become less well defined as ϵ increases. For smaller values of ϵ, the rolls are mostly straight and a single set can occupy a large portion of the cell. At higher ϵ, straight rolls are generally less likely to occur, and typically, many sets of rolls are observed in the cell. This appears to be due to the stronger effects of mean flow for the larger values of ϵ which have a somewhat destabilizing effect on these structures. In many cases, the structures we have classified as roll-like have a visual appearance more similar to domain behavior, but it is clear that the roll patterns do not exhibit any kind of switching phenomenon. Thus, the distinction between roll and domain structures is based on their dynamic behavior rather than their visual appearance.

In Figs.(4.6) – (4.8) we show representative patterns obtained in each of the regions of parameter space. For each value of ϵ, we see the same trend for the patterns to go from a spiral state to a roll state to a domain state, as g_3 is increased. In the roll state, the patterns are quasi-static, and changes are seem to occur only over long times scales of the order $O(100)$ time units. In the domain states, clear switching of the orientation of rolls is seen over reasonably short time scales of the order $O(10)$. It should be noted also that the roll states and domain states are more clearly defined for the smaller values of ϵ. For $\epsilon = 0.7$, these states clearly show more disorder than the corresponding states at $\epsilon = 0.4$. This is to be expected since the system is more strongly influenced by nonlinear effects as ϵ increases.

We have not been able to determine definitively if the transitions between the various states are sharp or occur in a more continuous way. Certainly, if we start in a spiral state (at some value of ϵ and g_3) and approach the boundary between the spiral and roll states by increasing g_3 (keeping ϵ fixed), all spiral structures are eventually eliminated from the cell. Before this transition point, the spirals are replaced by straight or moderately curved roll structures but well defined spirals still persist in these patterns. Thus, it is difficult to say at this point whether the state is truly a spiral one, or a mix of spiral and roll state. By further increasing g_3, we will eventually lose all spiral structures from the pattern and it is at this point that we place the boundary between the spiral and roll states. Thus the point at which we lose all spirals seems reasonably well defined, but it is

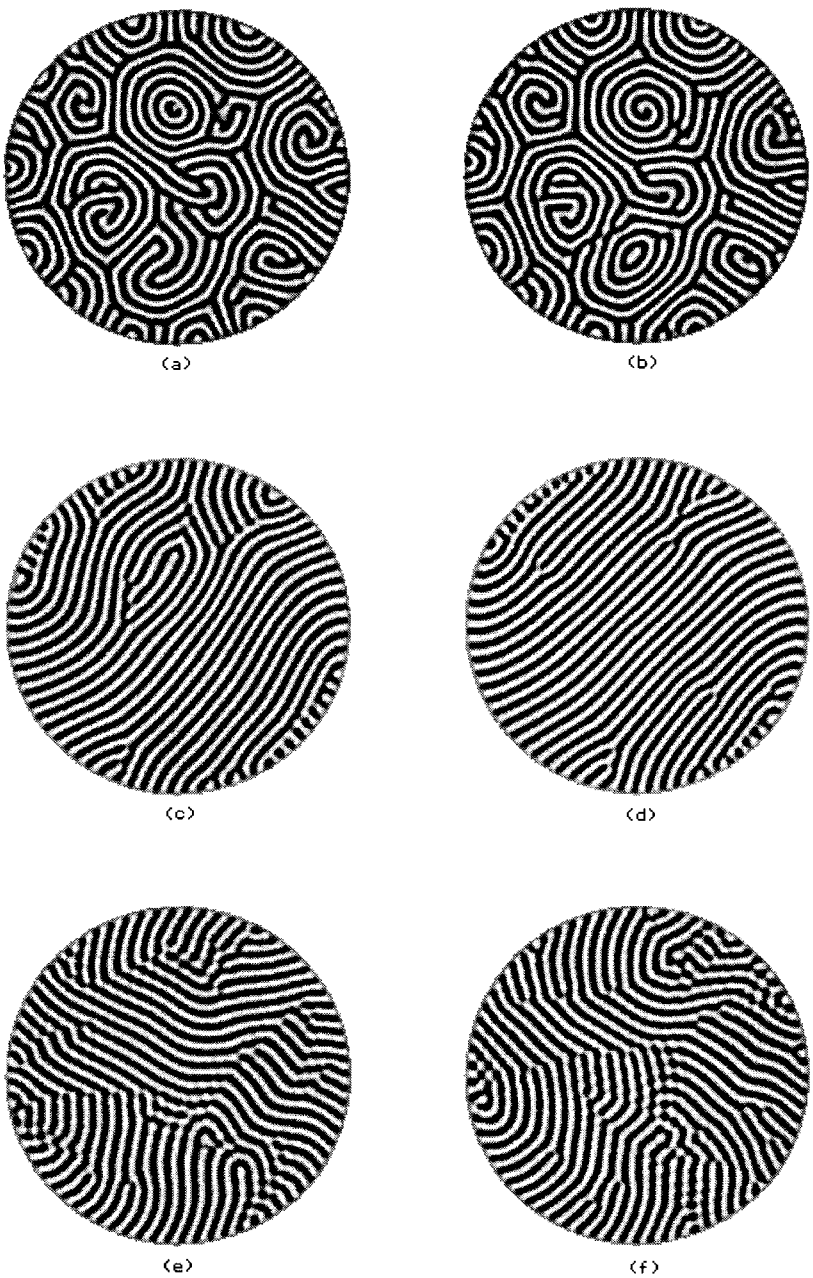

Figure 4.6: Representative patterns for $\epsilon = 0.4$, $g_m = 50$. The different states are obtained by increasing the rotation rate g_3. Spiral states are shown at (a) $t = 1100$, (b) $t = 1500$ for $g_3 = 0$. Roll states are shown at (c) $t = 1000$, (d) $t = 1400$ for $g_3 = 1.5$. Domain chaos states are shown at (e) $t = 400$, (f) $t = 500$ for $g_3 = 4.5$.

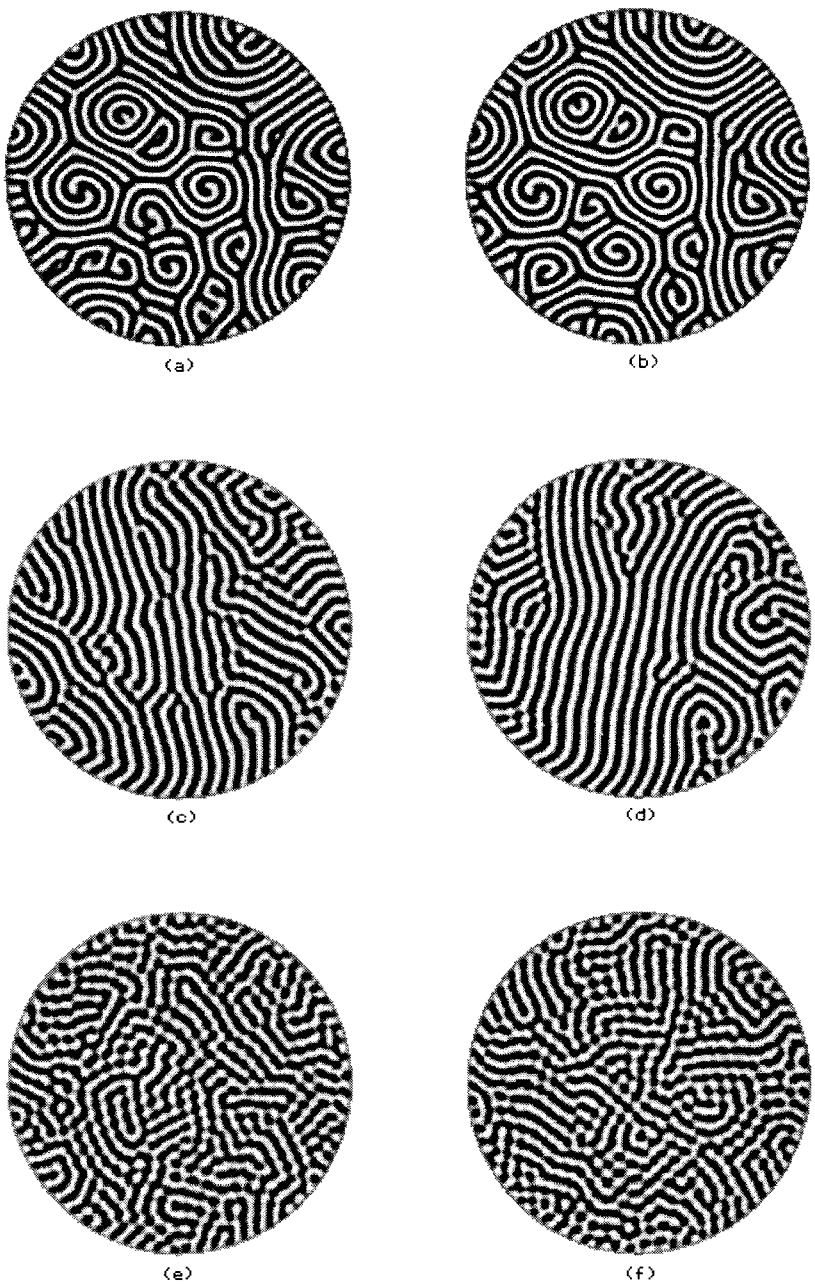

Figure 4.7: Representative patterns for $\epsilon = 0.55$, $g_m = 50$. The different states are obtained by increasing the rotation rate g_3. Spiral states are shown at (a) $t = 700$, (b) $t = 1100$ for $g_3 = 0$. Roll states are shown at (c) $t = 400$, (d) $t = 600$ for $g_3 = 6$. Domain chaos states are shown at (e) $t = 300$, (f) $t = 400$ for $g_3 = 9$.

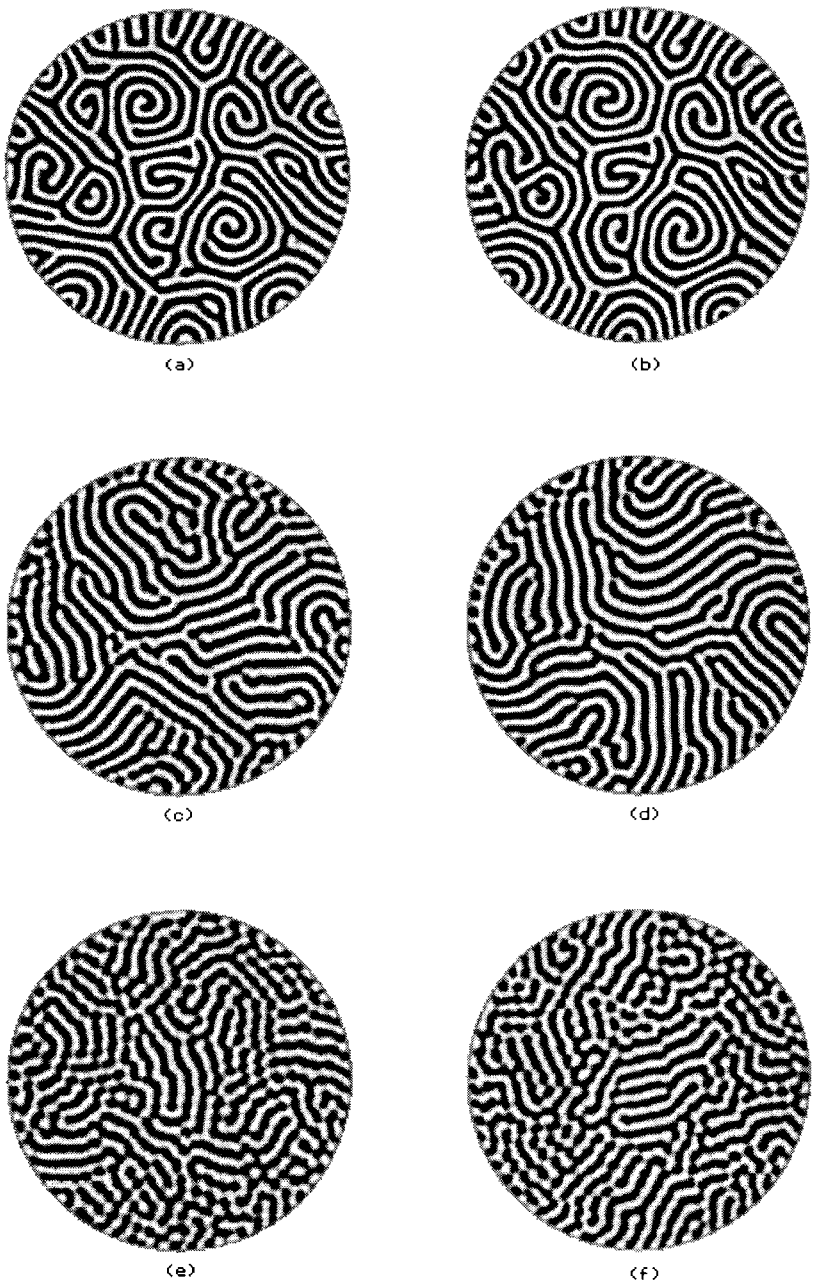

Figure 4.8: Representative patterns for $\epsilon = 0.7$, $g_m = 50$. The different states are obtained by increasing the rotation rate g_3. Spiral states are shown at (a) $t = 1150$, (b) $t = 1550$ for $g_3 = 1.5$. Roll states are shown at (c) $t = 400$, (d) $t = 600$ for $g_3 = 9$. Domain chaos states are shown at (e) $t = 200$, (f) $t = 300$ for $g_3 = 15$.

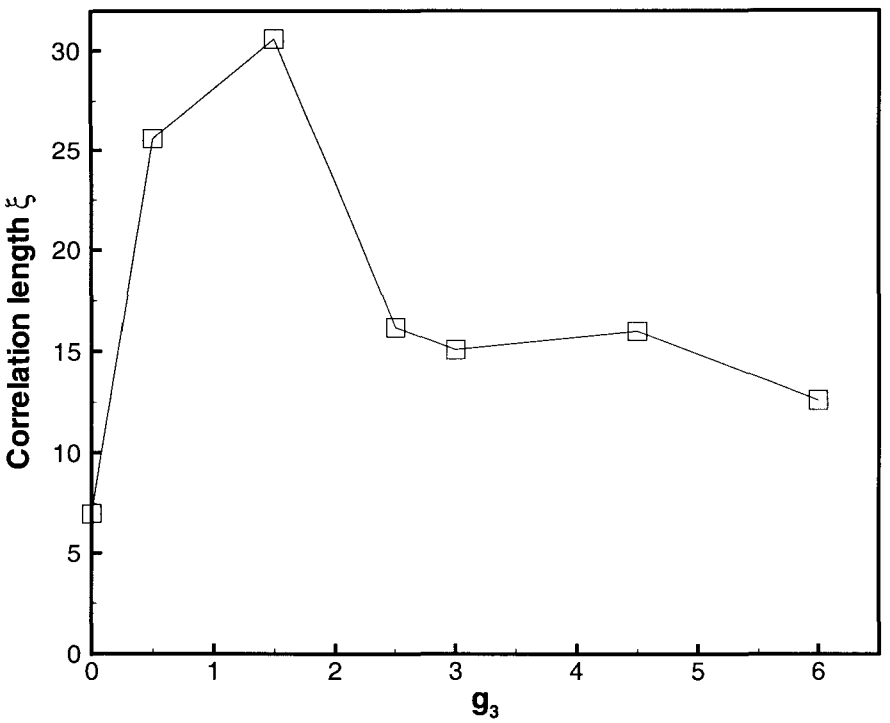

Figure 4.9: Correlation length as function of g_3 for $\epsilon = 0.4$, $g_m = 50$.

a matter of definition as to whether the states to the left of this boundary are classified as spiral states, since they certainly also contain roll structures. The boundary between roll and domain states is somewhat easier to define since, as we noted before, these are classified based on whether there is dynamic switching of the domain orientations.

In order to better quantify the transitions through the various states, we consider the correlation lengths of the patterns. We show in Fig. (4.9) and Fig. (4.10) the correlation lengths as functions of the rotation rate g_3 for $\epsilon = 0.4$ and 0.55 respectively. In these plots, a clear peak is seen for a particular range of g_3. These clearly correspond to the regions where we obtain the roll states since these are the patterns that are most highly correlated. The peaks have a reasonably well defined support, suggesting that the transition from the roll state to other states is reasonably sharp. This is certainly

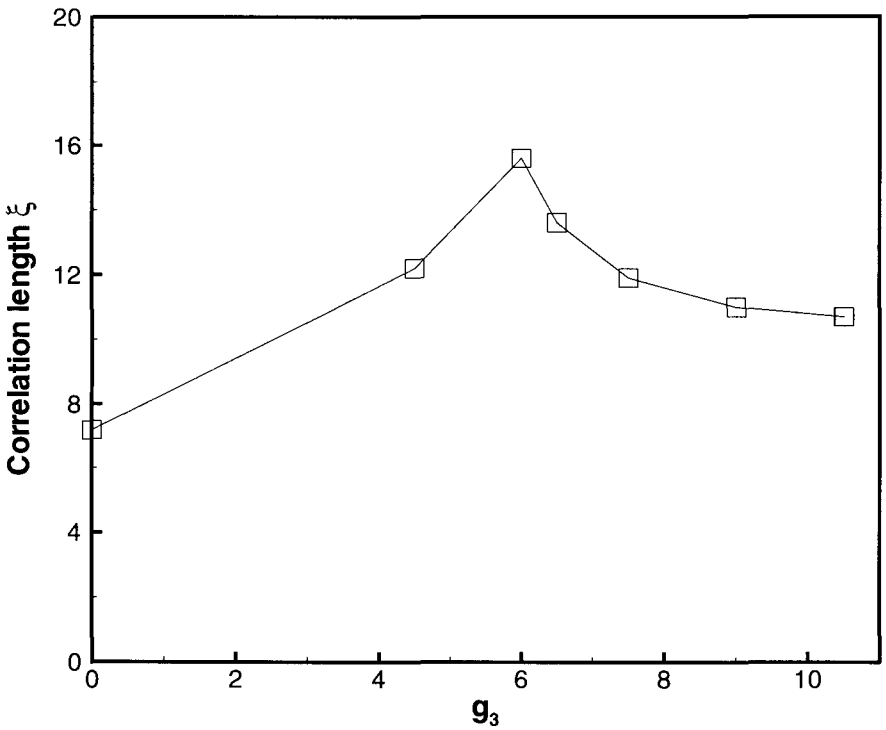

Figure 4.10: Correlation length as function of g_3 for $\epsilon = 0.55$, $g_m = 50$.

more significant for the smaller value of $\epsilon = 0.4$. Unfortunately our data is insufficient to completely justify this claim. The peak is more clearly pronounced for smaller $\epsilon = 0.4$. As we have noted before, and as can be seen in snapshots of the patterns (see Figs. (4.6) – (4.8)), more disorder in the patterns is expected as ϵ increases. Thus, we expect smaller correlation lengths for the larger values of ϵ, and thus a lower peak for the roll states.

Finally, we would like to note that the transition boundary we have found between the spiral and roll states is somewhat different from that found in experiment [32]. In the experiments, rotation is seen to enhance the spiral state in the sense that spirals are observed at lower values of ϵ when a small amount of rotation is added to the system. This can be seen in Fig. (4.11) which is reprinted from the work of Hu *et al.* [32]. In this diagram, the spiral-roll boundary is the line between the regions II and III. We note that this line has negative slope, in contrast to the positive slope seen in our results in Fig. (4.5). This indicates that there is a clear difference between our model and the physical fluid system. We note however that our results are consistent with the numerical work of Ponty *et al.* [43, 44], who have also considered Swift-Hohenberg type equations, rather than the fluid equations. They have also observed a competition between rotation, which is seen to order the system, and mean flow, which is seen to destructure the system. It is clear that further work is necessary to address this fundamental difference in the spiral states observed in the Swift-Hohenberg models and the full fluid system. On the other hand, our boundary between the roll and domain states are consistent with experiments (see Fig. (4.5) and Fig. (4.11). This further confirms the success of our Swift-Hohenberg model to capture the dynamics in the KL regime.

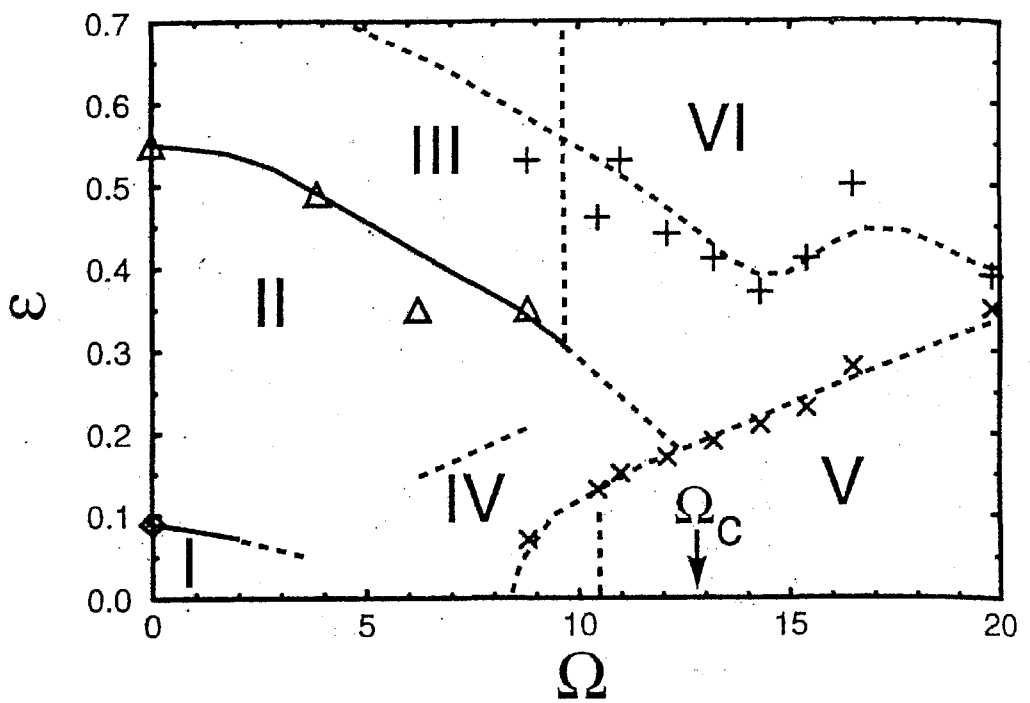

Figure 4.11: Phase diagram in the ϵ-Ω parameter space for a cell of aspect ratio 40 from the experimental work of Hu *et al.* [32]. The division into regions was done by visual observations of the patterns, and in some cases supplemented by quantitative measurements. Solid lines denote known boundaries whereas dashed lines are interpolations or suggestions of boundaries. In regions I and II, roll states are the predominant structures observed. In region III spirals are predominantly observed while in regions IV and V, the usual domain states associated with the KL instability are found. More disordered structures or a mixture of the above states are generally found in region VI. We see that the transition boundary between the roll (II) and spiral (III) states has a negative slope, contrary to our results (see Fig. (4.5)). The boundary between roll (II) and domain (IV and V) states is consistent with our numerical results.

Chapter 5

Conclusions

In this thesis we have developed and implemented a fully implicit scheme to numerically integrate equations of Swift-Hohenberg type in truly circular domains of large radius. This allows us to remove the stiffness associated with the linear biharmonic terms and to then evolve the solutions over very long time scales. The difficulty of solving in circular domains is overcome by integrating the equations in polar coordinates, but this creates other difficulties due to the nonuniform spatial grid. We show that our solutions can be stabilized by simply increasing the relative radial resolution. However, this cannot be done over the entire domain as the complexity quickly becomes prohibitive in large radius cells. Thus we have shown the effectiveness of using a variable radial mesh to overcome this problem.

Next we applied pattern analysis techniques similar to those used in experiments on rotating Rayleigh-Bénard convection [31, 33] to determine appropriate time and length scales in the Küppers-Lortz regime. Our study shows that our model equations follow the theoretically predicted scalings for the correlation length and domain switching frequency. However, for the correlation length, it is necessary to scale appropriately to take account of finite size effects. We find that the correlation length scales like the size of the cell, when the cell is small and/or when ϵ is small. Our results are consistent with those from experiment [33] in the sense that deviations from the theoretical scaling can be attributed to finite size effects. Our results provide strong evidence for this conjecture. In terms of the time scales, we have found that the domain switching frequency scales linearly with ϵ in agreement with the theoretical scaling. In this case, we have not found it is necessary to scale appropriately for finite size effects. The finite geometry and our simple treatment of the boundary conditions appears to enhance the domain switching behavior of our solutions, since sidewall nucleated rolls play an important role in smaller cells. This differs from the experimental results, which show significant devi-

ation from the theoretical scalings even for ϵ close to zero. It is likely therefore that the lateral boundaries play a very important role in the experiment and more complicated phenomena may be occurring there. To test this conjecture, it would be worthwhile incorporating more complicated boundary conditions into our model equations to help determine if this is the source of the discrepancy.

We have also studied the effect of rotation on the spiral chaos state which is obtained by the addition of mean flow effects to the Swift-Hohenberg equation. We find that rotation and mean flow effects compete in this system. Rotation tends to have an ordering effect while mean flow has a destructuring effect. The addition of mean flow appears to shift the wave number of the pattern which results in a shift in the onset of the KL instability. In the presence of mean flow, it is therefore necessary to rotate the system at higher rates in order to observe the KL instability. Mean flow effects increase with increasing ϵ so particularly large rotation rates are necessary before the KL instability is observed at large $\epsilon \approx 0.7$. A consistent sequence of patterns is obtained for $0.4 < \epsilon < 0.7$, as we increase the rotation rate. For small amounts of rotation, spirals are observed. At moderate rotation rates, the spirals are replaced by roll-like structures. By further increasing the rotation rate, the roll structures become dynamic and the familiar KL domain switching patterns are observed. The transitions across the boundaries (in parameter space) appear to be sharp although some ambiguity in the classification of the spiral/roll transition exists. Generally, we classify a pattern to be a spiral state if there are any spiral structures observed, but often spirals and roll structures will coexist in the cell.

In terms of future work, there is still a need to determine if there are other effects not accounted for in our model of the Küppers-Lortz instability that may be responsible for the different time and length scalings seen in experiment. As we have already mentioned, the reflection-symmetry-breaking boundary conditions of Kuo may prove to be a useful addition to the model. The conditions cause significant changes in the structure of the matrices to be solved, which may possibly destabilize our scheme. It would, however, be a worthwhile avenue to pursue since the conditions give rise to a unique state not seen before in Swift-Hohenberg models in finite geometries that may well account for realistic sidewall effects found in the physical system.

Finally, there is a need to carry out direct numerical simulation on the full fluid system. As we have mentioned, this is currently being undertaken, but a code in the cylindrical geometry is still some time away. There are also algorithmic improvements that need to be made since the current implementation in the rectangular geometry is only a semi-implicit code and suffers somewhat from a severe time step restriction.

Bibliography

[1] W.E. Arnoldi. *Quart. Appl. Math.*, 9:17, 1951.

[2] M. Assenheimer and V. Steinberg. Transition between Spiral and Target States in Rayleigh-Bénard Convection *Nature*, 367:345–347, 1994.

[3] M. Bestehorn, M. Neufeld, R. Friedrich and H. Haken. Spiral-Pattern Formation in Rayleigh-Bénard Convection – Comment. *Physical Review E*, 50(1):625–626, 1994.

[4] M. Bestehorn and C. Pérez-Garcia. Study of a Model of Thermal Convection in Cylindrical Containers. *Physica D*, 61(1–4):67–76, 1992.

[5] P.E. Bjørstad. Fast numerical-solution of the biharmonic Dirichlet problem on rectangles. *SIAM J. Numer. Anal.*, 20(1):59–71, 1983.

[6] P.E. Bjørstad. *Direct solution of a generalized biharmonic equation on a disk.* Efficient solutions of elliptic systems:proceedings of a GAMM-seminar. Braunschweig, 1984.

[7] E. Bodenschatz, D.S. Cannell, J.R. de Bruyn, R. Ecke, Y. Hu, K. Lerman and G. Ahlers. Experiments on 3 Systems with Nonvariational Aspects. *Physica D* 61(1–4): 77–93, 1992.

[8] E. Bodenschatz, J.R. de Bruyn, D.S. Cannell and G. Ahlers. Transitions between Patterns in Thermal Convection. *Physical Review Letters*, 67(22):3078–3081, 1991.

[9] P.N. Brown and Y. Saad. Convergence theory of nonlinear Newton-Krylov algorithms. *SIAM J. Opt.*, 4:297–330, 1994.

[10] F.H. Busse and R.M. Clever. *J. Fluid Mechanics*, 91:319, 1979.

[11] F.H. Busse and K.E. Heikes. *Science*, 208:173, 1980.

[12] S. Chandrasekhar. Hydrodynamic and Hydromagnetic Stability. *Oxford University Press*, 1961.

[13] R.M. Clever and F.H. Busse. *J. Fluid Mechanics*, 65:625, 1974.

[14] M.C. Cross. Derivation of the amplitude equation at the Rayleigh-Bénard instability. *Physics of Fluids*, 23:1727, 1980.

[15] M.C. Cross. Ingredients of a Theory of Convective Textures Close to Onset. *Physical Review A*, 25(2):1065–1076, 1982.

[16] M. Cross. Theoretical modelling of spiral chaos in Rayleigh-Bénard convection. *Physica D*, 97(1-3):65–80, 1996.

[17] M.C. Cross and P.C. Hohenberg. Pattern Formation Outside of Equilibrium. *Reviews of Modern Physics*, 65(3) Part 2:851–1112, 1993.

[18] M.C. Cross, D. Meiron, and Y. Tu. Chaotic Domains: A numerical investigation. *Chaos*, 4(4):607–619, 1994.

[19] R.E. Ecke, Y. Hu, R. Mainieri and G. Ahlers. Excitation of spirals and chiral-symmetry breaking in Rayleigh-Bénard convection. *Science* 269:1704–1707, 1995.

[20] W.S. Edwards, L.S. Tuckerman, R.A. Friesner, and D.C. Sorensen. Krylov Methods for the Incompressible Navier-Stokes Equations. *J. Comp. Phys.*, 110:82–102, 1994.

[21] M. Fantz, R. Friedrich, M. Bestehorn and H. Haken. Pattern formation in rotating Bénard convection. convection. *Physica D*, 61(1–4):147–154, 1992.

[22] H.S. Greenside and W.M. Coughran, Jr. Nonlinear pattern formation near the onset of Rayleigh-Bénard convection. *Physical Review A*, 30(1):398–428, 1984.

[23] H.S. Greenside and M.C. Cross. Stability analysis of two-dimensional models of three-dimensional convection. *Physical Review A*, 31:2492–2501, 1985.

[24] H.S. Greenside, M.C. Cross and W.M. Coughran, Jr. Mean flows and the onset of chaos in large-cell convection. *Physical Review Letters*, 60(22):2269–2272, 1988.

[25] K.E. Heikes. *Ph.D Thesis, UCLA* 1979.

[26] K.E. Heikes and F.H. Busse. *Ann. N.Y. Acad. Sci.*, 357:28, 1980.

[27] M. Hochbruck and C. Lubich. On Krylov subspace approximations to the matrix exponential operators. SIAM Journal of Numerical Analysis 34:(5) 1911–1925, 1997.

[28] M. Hochbruck, C. Lubich and H. Selhofer. Exponential integrators for large systems of differential equations. SIAM Journal on Scientific Computing 19:(5) 1552–1574, 1998.

[29] Y. Hu, R.E. Ecke and G. Ahlers. Transition to Spiral Defect Chaos in Low Prandtl Number Convection. *Physical Review Letters*, 74(3):391–394, 1995.

[30] Y. Hu, R.E. Ecke and G. Ahlers. Convection for Prandtl Numbers Near 1 – Dynamics of Textured Patterns. *Physical Review E*, 51(4):3263–3279, 1995.

[31] Y. Hu, R.E. Ecke and G. Ahlers. Time and Length Scales in Rotating Rayleigh-Bénard convection. *Physical Review Letters*, 74(25):5040–5043, 1995.

[32] Y. Hu, R.E. Ecke and G. Ahlers. Convection Under Rotation for Prandtl Numbers Near One: Linear stability, wave-number selection, and pattern dynamics. *Physical Review E*, 55(6):6928–6949, 1997.

[33] Y. Hu, W. Pesch, G. Ahlers and R.E. Ecke. Convection Under Rotation for Prandtl Numbers Near One: Küppers-Lortz instability. *Physical Review E*, 58(5):5821–5833, 1998.

[34] E.Y. Kuo. Ph.D. Thesis, Caltech 1994.

[35] G. Küppers and D. Lortz. J. Fluid Mechanics, 35:609, 1969.

[36] G. Küppers. Physics Letters, 32A:7, 1970.

[37] M.C. Lai and H.S. Greenside. Private communication.

[38] R.B. Lehoucq and D.C. Sorensen. Deflation techniques for an implicitly restarted Arnoldi iteration. *SIAM Journal on Matrix Analysis and Applications*, 17(4):789-821, 1996.

[39] P. Manneville. J. Physics (Paris), 44:759, 1983.

[40] S.W. Morris, E. Bodenschatz, D.S. Cannell and G. Ahlers. Spiral Defect Chaos in Large Aspect Ratio Rayleigh-Bénard Convection. *Physical Review Letters*, 71(13):2026–2029, 1993.

[41] M. Neufeld, R. Friedrich and H. Haken. Order-Parameter Equation and Model Equation for high Prandtl number Rayleigh-Bénard Convection in a large aspect ratio system. *Zeitschrift Fur Physik B*, 92(2):243–256, 1993.

[42] L. Ning and R. Ecke. Küppers-Lortz transition at high dimensionless rotation rates in Rotating Rayleigh-Bénard Convection. *Physical Review E*, 47(5):2991–2994, 1993.

[43] Y. Ponty, T. Passot and P.L. Sulem. Chaos and Structures in Rotating Convection at Finite Prandtl Number. *Physical Review Letters*, 79(1):71–74, 1997.

[44] Y. Ponty, T. Passot and P.L. Sulem. Pattern dynamics in rotating convection at finite Prandtl number. *Physical Review E*, 56(4):4162–4178, 1997.

[45] E.D. Siggia and A. Zippelius. Pattern Selection in Rayleigh-Bénard convection near threshold. *Physical Review Letters*, 47:835, 1981.

[46] J.B. Swift and P.C. Hohenberg. Hydrodynamic fluctuations at the convective instability. *Physical Review A*, 15:319, 1977.

[47] M. Tokman. Private communication.

[48] Y. Tu and M.C. Cross. Chaotic Domain Structure in Rotating Convection. *Physical Review Letters*, 69(17):2515–2518, 1992.

[49] H. Xi and J.D. Gunton. Spatiotemporal Chaos in a Model of Rayleigh-Bénard Convection. *Physical Review E*, 52(5):4963–4975, 1995.

[50] H. Xi, J.D. Gunton and J. Viñals. Spiral Defect Chaos in a Model of Rayleigh-Bénard Convection. *Physical Review Letters*, 71(13):2030–2033, 1993.

[51] F. Zhong and R. Ecke. Pattern Dynamics and Heat Transport in Rotating Rayleigh-Bénard Convection. *Chaos*, 2(2):163–171, 1992.

[52] F. Zhong, R. Ecke and V. Steinberg. Rotating Rayleigh-Bénard convection: The Küppers-Lortz transition. *Physica D*, 51:596, 1991.

[53] A. Zippelius and E.D. Siggia. Disappearance of stable convection between free-slip boundaries. *Physical Review A*, 26(3):1788–1790, 1982.